PROBING NEUTRINO OSCILLATION PARAMETERS WITH ATMOSPHERIC NEUTRINOS AT ICAL

By

Chandan Gupta

PHYS01201404002

Bhabha Atomic Research Centre, Mumbai

A Thesis submitted to the
Board of Studies in Physical Sciences
in partial fulfillment of the requirements
for the Degree of

DOCTOR OF PHILOSOPHY

of

Homi Bhabha National Institute

March, 2019

STATEMENT BY AUTHOR

This dissertation has been submitted in partial fulfillment of requirements for an advanced degree at Homi Bhabha National Institute (HBNI) and is deposited in the Library to be made available to borrowers under rules of the HBNI.

Brief quotations from this dissertation are allowable without special permission, provided that accurate acknowledgement of source is made. Requests for permission for extended quotation from or reproduction of this manuscript in whole or in part may be granted by the Competent Authority of HBNI when in his or her judgement the proposed use of the material is in the interests of scholarship. In all other instances, however, permission must be obtained from the author.

Date: March, 2019

Place: Mumbai

Chandan Gupta

(Enrolment Number PHYS01201404002)

DECLARATION

I, hereby declare that the investigation presented in the thesis has been carried out by me. The work is original and has not been submitted earlier as a whole or in part for a degree/diploma at this or any other Institution/University.

Date: March, 2019

Place: Mumbai

Chandan Gupta

(Enrolment Number PHYS01201404002)

List of Publications arising from the thesis

Published

(1) "Sensitivity to neutrino decay with atmospheric neutrinos at the INO-ICAL detector" - Sandhya Choubey, Srubabati Goswami, **Chandan Gupta**, S. M. Lakshmi, and Tarak Thakore.

Phys. Rev. D 97, 033005 [arXiv: 1709.10376]

(2) "Enhancing the hierarchy and octant sensitivity of ESSνSB in conjunction with T2K , NOνA and ICAL@INO" - Kaustav Chakraborty, Srubabati Goswami, **Chandan Gupta**, Tarak Thakore.

JHEP 1905 (2019) 137 [arXiv: 1902.02963]

Manuscript in preparation

(1) "Sensitivities to mass hierarchy and octant of θ_{23} of a 50 kt magnetized iron detector in the presence of invisible neutrino decay and oscillations" - Sandhya Choubey, Srubabati Goswami, **Chandan Gupta**, S. M. Lakshmi.

Conference Proceedings

(1) "Bounds on Neutrino Decay Lifetime with ICAL detector" - **Chandan Gupta**, Sandhya Choubey, Srubabati Goswami, S. M. Lakshmi and Tarak Thakore.

XXII DAE High Energy Physics Symposium: Delhi, India, December 12-16, 2016 **Springer Proc. Phys.** Vol- 203, Pages-447-450, Year- 2018, doi-10.1007/978-3-319-73171-1_104

(2) "Study of invisible neutrino decay and oscillation in the presence of matter

with a 50 kton magnetised iron detector" - Choubey, S. and Goswami, S. and **Gupta, C.** and Mohan Lakshmi S. and Thakore, Tarak.

2017 International Workshop on Neutrinos from Accelerators (NuFact17), Vol- NuFact2017, Pages-147, Year- 2018, doi- 10.22323/1.295.0147

Other Publication

(1) "Physics Potential of the ICAL detector at the India-based Neutrino Observatory (INO)" - ICAL Collaboration, **Pramana 88(2017) no.5, 79**

Chandan Gupta

(Enrolment Number PHYS01201404002)

Dedicated to,

All my teachers

ACKNOWLEDGEMENTS

It gives me an immense pleasure to express my sincere gratitude towards my PhD thesis supervisor Prof. Gobinda Majumder for his support and encouragement throughout this journey. I especially like to thank Prof. Srubabati Goswami for her role as a co-supervisor, mentor, collaborator and constant guidance during the writing of the thesis.

I like to thanks Prof. Amol Dighe who first introduced me to the subject of neutrino physics and motivated me to pursue my thesis in this field. I am highly indebted to my other doctoral committee members Prof. Prafulla Behera, Prof B. K. Nayak, Prof. Amol Dighe and Prof. Sudeshna Banerjee for their constant vigilance and invaluable suggestions throughout the course of this work.

I express my gratitude to Prof. N. K. Mondal and Prof. V. M. Datar, former and current project director of INO, for their support and motivation. Also, I am highly thankful to all the members of INO collaboration and the INO Graduate training program, which gave me an excellent learning opportunity.

I especially want to thank Prof. Raj Gandhi who motivated me to pursue the research career at the first place. I would like to thank all my teachers Prof. Gagan Mohanty, Prof. Amol Dighe, Prof. Vandana Nanal, Prof. K. V. Srinivasan, Prof. B. Satyanarayana, Prof. A. Shrivastava, Prof. K. Mahata, Prof. N. K. Mondal, Prof. S. Banerjee and Prof. Gobinda Majumder, who taught me during my coursework at TIFR. I thank all the past and present colleagues at TIFR, Suresh Kalmani, Piyush Verma, Sharad R Joshi, L. V. Reddy, P Nagraj, Pavan Kumar, Ganesh Ghodke, V V Asgolkar, Ravindra R Shindhe, Mandar N Saraf, Yuvaraj E, Dipankar Sil, H Pathaleswar, Jayaprakash, N Sivaramakrishnan, Puneet Kaur, Darshana Gonji, Upendra Gokhale, who comforted me during my stay at TIFR. I am highly indebted to my collaborators, Tarak Thakore, S. M. Lakshmi, Kaustav Chakraborty and Sandhya Choubey. Working with them was a learning experience for me altogether.

I thank my seniors Sumanta Pal, Vivek Singh, Varchaswi Kashyap, Sudeshna Dasgupta, Salim Mohammed, Meghna K. K., Moon Moon Devi, Neha Dokania, Nitali Das, Rajesh Ganai, Raveendrababu Karnam, Deepak Tiwari, Abhik Jash, Ali Ajmi, Animesh Chatterjee, Anushree Ghosh, Kolahal Bhattacharya, Mathimalar, Monojit Ghosh, Gulab Bambhaniya, Subrata Khan, Sushant K Raut, Deepthi K. N., Biswajit Karmakar, Arindam Mazumdar, Soumya Jana, Soumya Sadhukhan, Manu George, Tamnoy Mondal, Arun Pandey, Kuldeep Sutar, Abhaya Swain and juniors Kaustav Chakraborty, Rukmani Bai, Soumik Bandyopadhyay, Bhavesh Chauhan, Vishnu K. N., Bharti Kundra, Ashish Narang, Richa Arya, Akansha Bhardwaj, Priyank Parashari, Balbeer Singh, Arvind Mishra, Aman Abhishek, Aman Phoghat, Mohammad Nijam, Neha Panchal, S. Pethuraj, Divya Divakaran, Suryanarayan Mondal, Aparajita Mazumder, Jaydeep Datta, Tanmay Poddar for various useful academic and non-academic discussions. I would like to thank Arko Roy, Avdhesh Kumar, Chandan Hati, Girish Kumar, Hrushikesh Sable and Anshika Bansal, with whom I have shared my office space during my enjoyable stay at PRL. I feel extremely fortunate to have friends like Lalit Shukla, Apoorva Bhatt, Shivangi Gupta, Amina Khatun, Newton Nath. Their presence always gave me homely feeling and their encouraging words have always kept me going throughout this journey.

I acknowledge the Department of Atomic Energy (DAE), Department of Science and Technology (DST) and HBNI for their help and financial assistance. I would like to thank the administration staff at TIFR and PRL for their support. I would like to extend my sincere thanks to Mr. Nagaraj from TIFR and Mr. Jigar Raval from PRL, for helping me in computational assistance from time to time. At last, I must express my gratitude to all the non-academic staff members who were always there to help me out anytime of the day.

Finally, I would like to thank my family for their unconditional love, support and encouragement, without which I would never have come this far.

Contents

Synopsis

Motivation

The fundamental particle neutrino has remained one of the most elusive particle since it's postulation in 1930. The theoretical existence of neutrino was first put forward by Pauli to solve the four momentum and angular momentum conservation in nuclear β-decay [1]. The first experimental detection came in 1956 by Reines and Cowan [2]. Since then neutrinos have always remained as an exciting field till today. According to the Standard Model (SM) of particle physics, neutrino is mass less. But the discovery of neutrino oscillation, a phenomenon where one mass eigen state changes it's flavour to another while traveling, established the non zero mass of the neutrinos and opened the door to explore the Beyond Standard Model (BSM) physics. The superposition of different mass eigenstates to form the flavour state is incorporated through a unitary transformation. In three flavour, the matrix elements can be parameterized by three mixing angle namely θ_{12}, θ_{23} and θ_{13} with an additional CP phase δ_{CP}. The mass matrix can be expressed with two independent mass squared differences Δm^2_{21} and Δm^2_{31} where $\Delta m^2_{ji} = m^2_j - m^2_i$. The amplitude of the oscillation is dictated by the three mixing angles while the frequency is governed by the two mass squared differences. Various world wide efforts are going on to probe the oscillation parameters [3]. The magnitude and the sign of Δm^2_{21} is decided by the Solar and reactor based neutrino experiments while the magnitude of Δm^2_{31} is known through atmospheric and long baseline (LBL)

experiments. The sign of the Δm^2_{31} remains an open question till date leaving two possible scenarios: $\Delta m^2_{31} > 0$ which is referred to as normal hierarchy (NH) and $\Delta m^2_{31} < 0$ which is called inverted hierarchy (IH). The phase δ_{CP} determines the CP violation in neutrino sector. The value of $\delta_{CP} = 0°, \pm 180°$ implies CP conservation whereas $\delta_{CP} = \pm 90°$ corresponds to maximum CP violation. The magnitude of the CP violating phase δ_{CP} is still unknown although global analysis [4] hints it to be near 270°. Among the mixing angles, θ_{12} is measured with high precision and in recent times θ_{13} has been measured with non-zero value [5]. Maximum mixing is assumed for θ_{23}, although any deviation from the maximum mixing (i.e. 45°) leaves two possible octant scenarios: i) $\theta_{23} < 45°$ implies lower octant (LO) and ii) $\theta_{23} > 45°$ implies higher octant (HO). Other than measuring oscillation parameters, various experiments are designed using various neutrino sources and innovative detector technologies with novel methods to probe the absolute mass scale of the neutrinos, the nature of neutrinos i.e. Dirac or Majorana. As a part of the global effort, the India-based Neutrino Observatory (INO) has been initiated in India to build an underground multidisciplinary laboratory. The proposed 50 kt magnetized Iron Calorimeter (ICAL) detector will measure the oscillation parameters using atmospheric neutrinos as sources and by using three identical modules of dimension 16 m × 16 m × 14.5 m each. ICAL will use the Resistive Plate Chambers (RPC) as an active material to detect the signals of neutrino interactions. The total height of the ICAL detector will be due to total 151 layers where each layer comprises of 5.6 cm iron block and the RPC with 4 cm gap in between. The whole detector will be magnetized to about 1.5 Tesla and will be placed inside the overall rock coverage of 1 km inside a mountain in the southern part of India to reduce the cosmic muon background. The main goal of INO is to determine the mass hierarchy by utilizing the matter effect and distinguishing ν_μ and $\bar{\nu}_\mu$ by separating μ^- and μ^+ respectively using the strong magnetic field. Along with standalone results, INO can also help by combing it's result with other global experiments to improve the sensitivities of

oscillation parameters using various synergies and search for new physics which is beyond the Standard Model.

In this thesis we have studied how mass hierarchy and octant sensitivity can be improved by combining different long baseline experiments with the atmospheric experiment INO. Parameter degeneracies pose challenges when calculating the sensitivity of oscillation parameters. By using different synergies we have shown how the bottle neck of degeneracies can be overcome and better sensitivities when combing long baseline experiments with the atmospheric experiment INO. In other study we have shown that if neutrino decay exist in nature how well the proposed neutrino experiment in India i.e. INO- ICAL will be able to put bounds on the decay parameters.

Events in ICAL

INO ICAL experiment will use atmospheric neutrinos as the source. These neutrinos are produced when the cosmic ray particles interact with the air molecules present in the atmosphere and from their subsequent decay products. The flux of such atmospheric neutrinos covers a wide range of energies, from MeV to as high as few TeV. These neutrinos interact with the ICAL detector material via two type of interactions: Charge Current (CC) and Neutral Current (NC). In the CC interaction, neutrino interacts with detector material and produce charge lepton of same flavour alongside hadrons whereas in NC interaction, neutrino does not loose it's identity and produce hadrons along side neutrino in the final state. For CC and NC interactions, different processes can take place depending on the type of the target molecule and the energy of the neutrino. These are classified into three broad categories: quasi elastic (QE), resonant production (RES) and deep inelastic scattering (DIS). In the low energy ($E_\nu < 1$ GeV) QE interaction become the dominant one where neutrino scatters entire nucleon elastically producing single

or multiple nucleons. In RES interaction neutrino can excite the target nucleon to a resonate baryonic state which further decays to different types of mesons and nucleons in the final state. This type of resonance process become dominant in the 1-2 GeV energy range. As the energy of the neutrino increases, the chances of neutrino interactions with the quarks, constituent of target nucleon, also increase and hadronic shower comprises of nucleons, mesons and other hadrons are generated. After 2 GeV, DIS become the most dominating interaction mechanism. Details of the interaction mechanism and the interaction modes can be found in [6]. INO experiment is planned to explore the matter effect of neutrinos in the GeV range and thus the main challenge is to differentiate the charge leptons produced in the CC interaction from the associated hadrons. As atmospheric flux contain both ν_e and ν_μ along with their associated anti neutrinos, the events of ICAL gets contribution from both of them. ICAL detector is optimized for the detection of ν_μ and $\bar{\nu}_\mu$ and the number of events detected by ICAL will be:

$$\frac{d^2N}{dE_\mu d\cos\theta_\mu} = t \times n_d \times \int dE_\nu d\cos\theta_\nu d\phi_\nu \times \left[P^m_{\mu\mu}\frac{d^3\Phi_\mu}{dE_\nu d\cos\theta_\nu d\phi_\nu} + P^m_{e\mu}\frac{d^3\Phi_e}{dE_\nu d\cos\theta_\nu d\phi_\nu}\right] \times \frac{d^2\sigma_\mu(E_\nu)}{dE_\mu d\cos\theta_\mu} \quad (1)$$

where n_d is the number of target nucleons in the detector, σ_μ is the differential neutrino interaction cross section in terms of the energy and direction of the muon produced, Φ_μ and Φ_e are the ν_μ and ν_e fluxes and $P^m_{\alpha\beta}$ is the oscillation probability of $\nu_\alpha \rightarrow \nu_\beta$ in matter. A sample of 1000 years of unoscillated neutrino events is generated using NUANCE-3.5 neutrino generator [7] which include the Honda 3D atmospheric neutrino fluxes [8] and neutrino-nucleus cross sections and simplified ICAL geometry. Oscillation is introduced by multiplying with the relevant oscillation probability in Earth matter assuming PREM density profile [9]. The events are smeared according to the resolution and efficiencies obtained from [10]. These process is repeated on an event by event basis which is reduced further to 500 kt

year to reduce statistical fluctuations. Both data and theory events in ICAL are generated using the same principle where the data is generated with central values of the oscillation parameters and the theory events are calculated for the allowed 3σ ranges of the oscillation parameters Δm^2_{31} and θ_{23}. Having good muon energy and angular resolution and the capability of ICAL detector to separate hadrons from the muon track, the events are binned in total three dimensional (3D) space namely (E_μ, $\cos\theta_\mu$, E'_{had}). Poissonian χ^2 analysis has been performed to extract the sensitivity of the experiment which is defined as:

$$\chi^2_{\pm} = \min_{\xi_l} \sum_{i=1}^{N_{E'_{had}}} \sum_{j=1}^{N_{E_\mu}} \sum_{k=1}^{N_{\cos\theta_\mu}} \left[2(N^{theory}_{ijk} - N^{data}_{ijk}) - 2N^{data}_{ijk} \ln(\frac{N^{theory}_{ijk}}{N^{data}_{ijk}}) \right] + \sum_{l=1}^{N_{pull}} \xi^2_l \quad (2)$$

where, $\chi^2_{\pm}$ refer to the χ^2 contribution from μ^- and μ^+ events respectively. The following systematic uncertainties are included in the analysis using pull method : i) Flux normalization error (20%), ii) cross section error (10%), iii) tilt error (5%), iv) zenith angle error (5%) and v) overall systematic error (5%).

Improving mass hierarchy and octant sensitivity with long baseline and atmospheric neutrino experiments

The main difficulty while finding out the unknown oscillation parameters, namely hierarchy, octant of θ_{23} and δ_{CP}, comes from the parameter degeneracies where different sets of unknown parameters produce same probabilities i.e. $P_{\alpha\beta}(\theta) \sim P_{\alpha\beta}(\theta')$ where $\theta \neq \theta'$. Several future experiments are proposed and planned to address the degeneracy problems and unambiguous determination of the unknown parameters. This includes the accelerator based experiments T2HK [11] /T2HKK [12], DUNE [13] and ESSνSB [14, 15]. Among these the main goal of the ESSνSB experiment

is the determination of δ_{CP}. In this thesis we have explored the possibility of proposed ESSνSB experiment in determining hierarchy and octant in conjunction with currently running accelerator experiments T2K and NOνA and proposed atmospheric neutrino experiment INO. T2K (Tokai to Kamioka) [16] is a 295 km baseline experiment with peak energy 0.6 GeV and uses JPARC neutrino beam facility with expected protons on target (POT) of 8×10^{21}/year. T2K uses two Ĉherencov detectors, a near and a far, with an off-axis of 2.5° from the neutrino beam. Super Kamiokande detector with fiducial volume 22.5 kt is used as an detector for T2K with an ability to distinguish electron and muon events from the shape of the Ĉherencov rings. In our study we have assumed 4 years of neutrino and four years of anti-neutrino runs for T2K. NOνA experiment [17] is also a beam based experiment which uses two scintillator detectors (near detector with fiducial volume 222 tons and the far detector with larger volume of 15 kt) with an off axis of 0.8°. NOνA uses high intensity neutrino beam from Fermilab with POT 7.3×10^{20}/year. NOνA is planned to operate with 3 years of neutrino and 3 years of anti-neutrinos with peak energy of 2 GeV. In our study we have used the re-optimized NOνA set up from [18, 19] and have used the full projected run time. ESSνSB [14, 15] is a proposed accelerator based experiment with a total baseline of 540 km and plans to use a water Ĉherencov detector like T2K. Focusing on the physics potential of the second oscillation maximum, ESSνSB will use high intensity neutrino beam from 2 GeV linac proton with an average beam power of 5 MW and 27×10^{23} POT from European Spallation Source (ESS) in Lund, Sweden. In our study we have used 2 years of neutrino and 8 years of anti neutrino runs. The simulation of the LBL experiments are done using General Long Baseline Experiment Simulator (GLOBES) package [20, 21]and the χ^2 analysis is done incorporating the pull variables. The signal (background) tilt error is taken 1%(5%) for T2K, 0.1%(0.1%) for NOνA and 0.1%(0.1%) for ESSνSB while other systematic uncertainties of different experiments considered in our analysis are summarized in Table 1. The

oscillation parameters used while generating events and their marginalization range are summarized in Table 2.

Channel	T2K	NOνA	ESSνSB
ν_e appearance	2% (5%)	5% (10%)	5% (10%)
$\bar{\nu}_e$ appearance	2% (5%)	5% (10%)	5% (10%)
ν_μ disappearance	0.1% (0.1%)	2.5% (10%)	5% (10%)
$\bar{\nu}_\mu$ disappearance	0.1% (0.1%)	2.5% (10%)	5% (10%)

Table 1: The signal (background) normalization errors used in the analysis for T2K, NOνA and ESSνSB .

Oscillation parameters	True value	Test range
$\sin^2 2\theta_{13}$	0.085	fixed
$\sin^2 \theta_{12}$	0.304	fixed
θ_{23}	42° (LO), 48° (HO)	$39° - 51°$
Δm^2_{21} (eV^2)	7.4×10^{-5}	fixed
Δm^2_{31} (eV^2)	2.5×10^{-3}	$(2.35 - 2.65) \times 10^{-3}$
$\delta_{\rm CP}$ (LBL)	$-180° : 180°$	$-180° : 180°$
$\delta_{\rm CP}$ (INO)	$-180° : 180°$	0°(fixed)

Table 2: The true and test values of the oscillation parameters used in our analysis.

Since INO experiment is not sensitive to $\delta_{\rm CP}$, the value of $\delta_{\rm CP}$ is kept fixed at 0° when analyzing INO data to save computation time. For the LBL experiments $\delta_{\rm CP}$ is varied between $-180°$ to 180°. While adding the INO results with the LBL experiments, first the marginalization over test-$\delta_{\rm CP}$ is performed for LBL experiments and added with INO χ^2. The final sensitivity of the combined experiments

are obtained after marginalizing over other parameters $|\Delta m^2_{31}|$, $\sin^2\theta_{23}$ as follows:

$$\chi^2_{tot} = \underset{\theta_{23},|\Delta m^2_{31}|}{\text{Min}} \left[\chi^2_{INO} + \underset{\delta_{CP}}{\text{Min}}\ \chi^2_{LBL}\right] \tag{3}$$

The mass hierarchy sensitivity with $\delta_{cp}(true)$ is shown in Figure 1 for different combinations: NH-LO, NH-HO, IH-LO and IH-HO for individual and combined experiments [22].

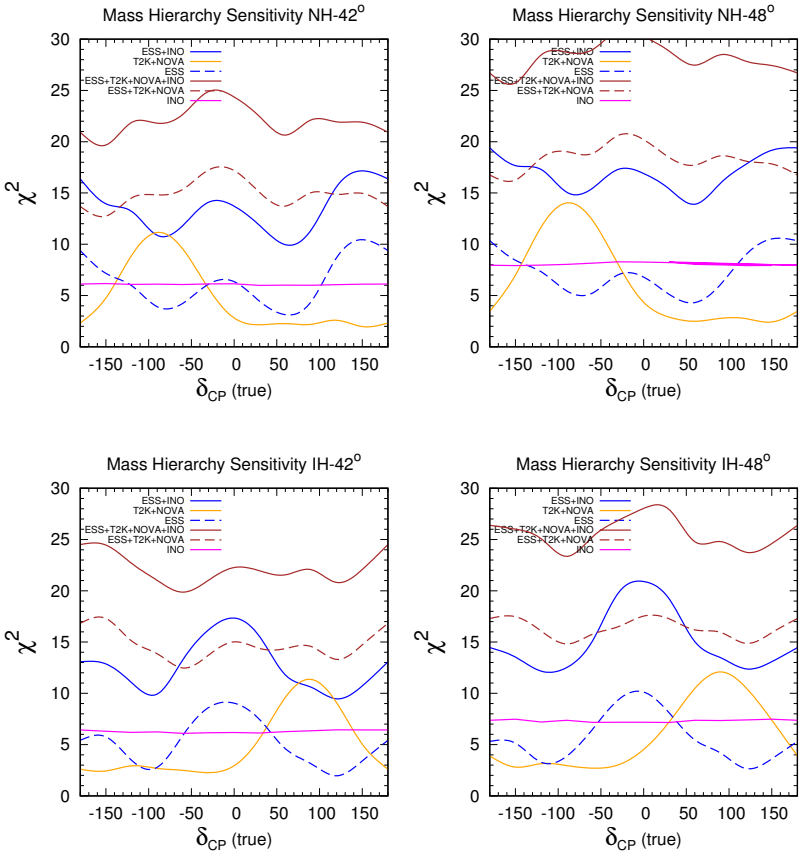

Figure 1: Mass difference determination for different hierarchies vs $\delta_{\rm CP}$ (true) for INO-3D ESSνSB T2K NOνA for four hierarchy-octant combinations starting from top right, clockwise in the order NH-LO, NH-HO, IH-HO and IH-LO. Each figure consists of six different experimental combinations which are represented as INO (magenta solid curve), ESSνSB (blue dashed curve), T2K + NOνA (orange solid curve), ESSνSB + INO (blue solid curve), ESSνSB + T2K + NOνA (brown dashed curve) and ESSνSB + T2K + NOνA +INO (brown solid curve).

The mass hierarchy sensitivity of INO is independent of δ_{CP} because of the sub-dominant effect of δ_{CP} in the survival probabilities and due to the smearing over directions [23, 24] which is shown by the magenta curve in Figure 1. The mass hierarchy sensitivity of ESSνSB experiment is shown by the dashed blue line in Figure 1. For all the combinations, mass hierarchy sensitivity is better for the CP conserving values ($0°$, $\pm180°$) than CP violating values ($\pm90°$). This happens because of the presence of wrong hierarchy solutions coming with right CP degeneracy for δ_{CP} (true) = $\pm90°$ which is not the case for δ_{CP} (true) = $0, \pm180°$. The hierarchy sensitivity of ESSνSB in the higher octant is better than lower octant but follows the same trend. The combined results of INO and ESSνSB follow the same trend as ESSνSB but a constant χ^2 addition makes the overall sensitivity to reach as high as 4σ for the CP conserving values in some of the hierarchy-octant combinations. The hierarchy sensitivity of T2K + NOνA experiment is shown by the yellow curve. The highest sensitivity comes at δ_{CP} = -90° for NH-LO and NH-HO combinations. This happens because of the combined run of neutrino and anti-neutrino runs in the analysis. For example, in the case of NH-LO, the wrong hierarchy-wrong octant degeneracy present in the neutrinos is compensated by the anti-neutrinos run which is free from such degeneracies making the lower half plane (LHP : $\delta_{CP} = -180° : 0°$) conducive for hierarchy determination. On the other hand for NH-HO, although anti-neutrinos suffer from wrong hierarchy-wrong octant and right CP degeneracy but adding neutrino, which is free from such degeneracies, removes the overall degeneracies making the LHP to be favorable for hierarchy determination. The opposite is true for IH. For IH-LO(HO), there is no degeneracy for neutrinos (anti-neutrinos) for δ_{CP} in the upper half plane (UHP : $\delta_{CP} = 0° : 180°$) giving better sensitivities. When T2K and NOνA results are added with ESSνSB , the CP dependence of the hierarchy sensitivity is governed by all the three experiments which is shown by the dashed brown line in the plots. The results from the combination of all the experiments i.e. adding INO with all the

LBL experiments, are shown by the solid brown line in the plots. The sensitivity of 5σ can be achieved for all the values of $\delta_{\rm CP}$ in NH-HO combination whereas the same sensitivity is achieved for $\delta_{\rm CP} = 0°$ in NH-LO combination and $\delta_{\rm CP} = 0°,\ \pm 180°$ in IH-HO combination. For all values of $\delta_{\rm CP}$, the hierarchy sensitivity remains higher than 4.4σ for IH-LO.

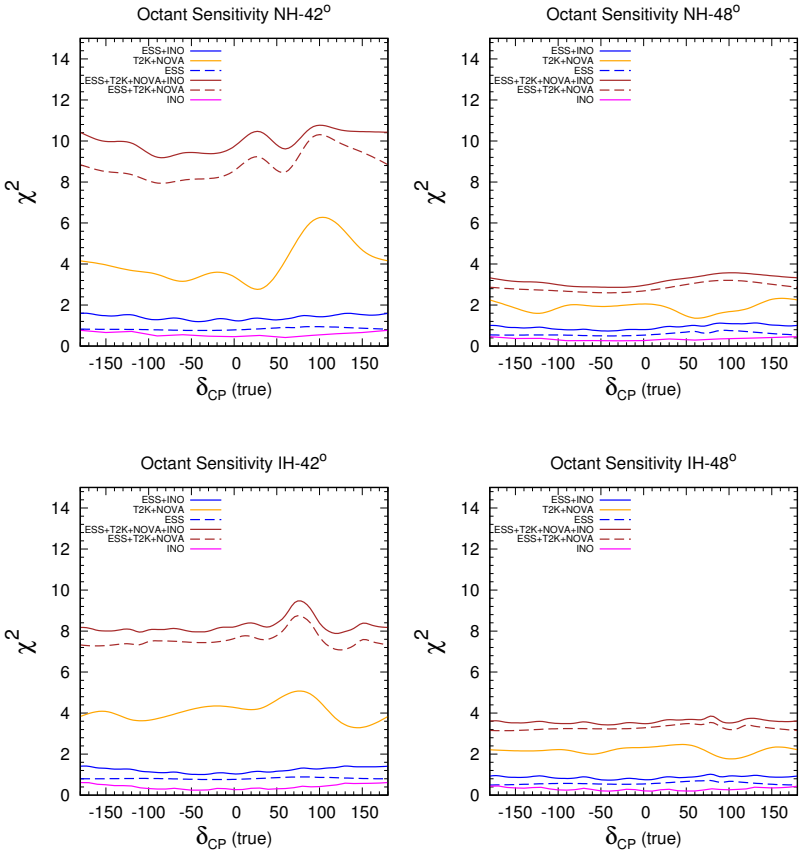

Figure 2: Octant sensitivity vs $\delta_{\rm CP}$ (true) for INO, ESSνSB , T2K and NOνA for four hierarchy-octant combinations starting from top right, clockwise in the order NH-LO, NH-HO, IH-HO and IH-LO. Each figure consists of six different experimental combinations which are represented as INO (magenta solid curve), ESSνSB (blue dashed curve), T2K + NOνA (orange solid curve), ESSνSB + INO (blue solid curve), ESSνSB + T2K + NOνA (brown dashed curve) and ESSνSB + T2K + NOνA + INO (brown solid curve).

We have also studied the octant sensitivity of individual and the combined analysis of these experiments. To calculate the octant sensitivity, data for a representative value of true θ_{23} belonging to LO (HO) is compared with the opposite octant HO(LO) along with the marginalization over $|\Delta m^2_{31}|$, hierarchy and $\delta_{\rm CP}$ (

only for LBL experiments). The plots in Figure 2 show the variation of octant sensitivity for the various experiments [22]. The octant sensitivity of INO is shown by the purple line and is seen to have poor octant sensitivity for all the combinations of hierarchy-octant. This happens because INO detects only muon signals which include both muon appearance and disappearance channel and the octant sensitivities are opposite for these two channels. On the other hand LBL experiments can measure signals from appearance and disappearance channel separately. The octant sensitivity of ESSνSB is shown by the dotted blue line and the poor sensitivities are due to the degeneracies present over all ranges of $\delta_{\rm CP}$ for the energies 0.25 GeV and 0.45 GeV. The contribution towards octant sensitivity mainly comes the 0.35 GeV energy bin. For T2K + NOνA , the octant sensitivity is shown by the yellow lines and has $\sim 2\sigma$ sensitivity for most of the $\delta_{\rm CP}$ range for the combination of NH-LO and IH-LO with peak sensitivities reaching up to $\sim 2.4\sigma$ and $\sim 2.2\sigma$ respectively for $\delta_{\rm CP} = 90^\circ$. The combination of neutrino and anti-neutrino runs help in removing the degenerate wrong octant solutions [25–27]. The synergy between T2K and NOνA also helps in increasing the sensitivity near $\delta_{\rm CP}$ =90° for such combinations. For the IH-LO scenario although neutrinos do not suffer from degeneracies in UHP but anti-neutrinos suffer from degeneracies with NH-HO at same $\delta_{\rm CP}$ and IH-HO with $\delta_{\rm CP}$ in the LHP. Due to the neutrino events having larger statistics, higher sensitivity is achieved for $\delta_{\rm CP}$ in UHP. When combining T2K + NOνA with ESSνSB , the sensitivity improves because of the synergies between T2K + NOνA and the ESSνSB . The rapid variation of the octant sensitivity χ^2 with $\delta_{\rm CP}$ for ESSνSB controls the overall shape of the combined experiments result and the position of the overall minimum. When combining INO with the LBL experiments, the octant sensitivity improves slightly which is shown by the solid brown curve. With this combination, 3σ sensitivity can be achieved by NH-LO combination for all $\delta_{\rm CP}$ whereas the same can be obtained for $\delta_{\rm CP} = 90^\circ$ with IH-LO. For NH/IH-HO the total sensitivity obtained is close to 2σ.

Neutrino decay sensitivity at ICAL

Neutrino oscillation has proven to be the solution for flavour transformation in the journey of neutrinos and the reason behind solar and atmospheric anomalies. Though INO is proposed mainly to measure neutrino mass hierarchy but INO has also the capability to study other physics scenarios such as neutrino decay as a sub dominant effect along with neutrino oscillation with the help of magnetized ICAL detector. Because of the non zero mass of the neutrino mass eigenstates, decay of the mass eigenstates is an open problem in physics and applied in the solar and atmospheric sectors to put bounds on the lifetime of the mass eigenstates [28–32]. Before the discovery of the non zero value of mixing angle θ_{13}, all the studies assume two flavour neutrino oscillation with decay. In this study we have assumed the invisible neutrino decay where one of the mass eigenstates decays to a sterile neutrino and a scalar particle where the sterile neutrino mass is unconstrained and does not have any standard model interactions and thus does not take part in oscillation. Our analysis assumes full three flavour oscillation with neutrino decay and the Earth matter effect. The propagation equation in presence of decay is shown in Equation 4, is solved numerically with PREM [9] density profile of the Earth to account for the matter effect.

$$
\begin{aligned}
i\frac{d\tilde{\nu}}{dt} &= \frac{1}{2E}\left[U\mathbb{M}^2U^\dagger + \mathbb{A}_{CC}\right]\tilde{\nu} \qquad \text{where,} \\
\mathbb{M}^2 &= \begin{pmatrix} 0 & 0 & 0 \\ 0 & \Delta m^2_{21} & 0 \\ 0 & 0 & \Delta m^2_{31} - i\alpha_3 \end{pmatrix} \text{ and} \\
\mathbb{A}_{CC} &= \begin{pmatrix} A_{cc} & 0 & 0 \\ 0 & 0 & 0 \\ 0 & 0 & 0 \end{pmatrix}
\end{aligned} \tag{4}
$$

The matter potential $A_{cc} = 2\sqrt{2}G_F n_e = 7.63 \times 10^{-5}\text{eV}^2(\frac{\rho}{\text{gm/cc}})(\frac{\text{E}}{\text{GeV}})$ where, G_F is Fermi constant and n_e is the electron number density in matter while ρ is the matter density. Three neutrino flavors are denoted by $\tilde{\nu} = (\nu_e\ \nu_\mu\ \nu_\tau)^T$. Here, we have assumed normal hierarchy (i.e. $m_3 > m_2 > m_1$) and the highest mass eigenstate to be decaying with decay constant $\alpha_3 = \frac{m_3}{\tau_3}$ where the mass eigenstate ν_3 with mass m_3 decays invisibly with decay lifetime τ_3 at rest. U denotes the 3×3 usual PMNS matrix. The effect of decay comes with the term $e^{-\frac{\alpha L}{E}}$ and have damped oscillations which modifies the amplitude of the oscillation while keeping the frequency unchanged. The event distributions with or without decay as a function of zenith angle for two different energies are shown in Figure 3 to show that decay effect is pronounced in low energies and higher baselines i.e. higher $\cos\theta$ values.

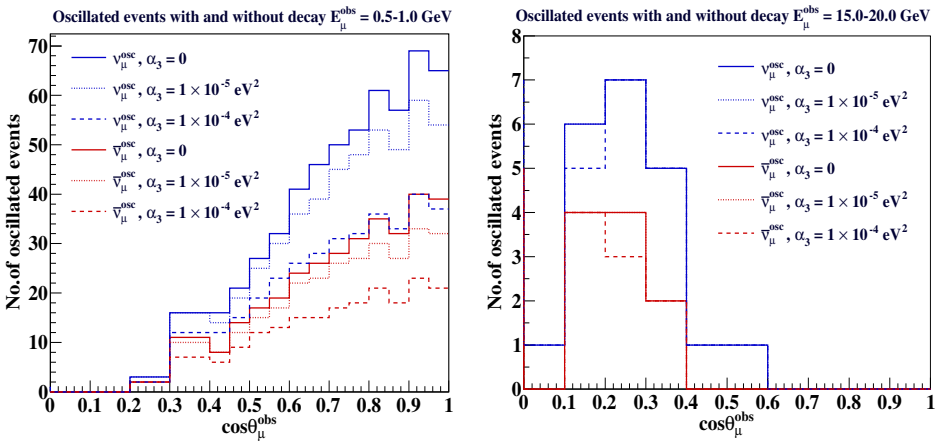

Figure 3: Oscillated ν_μ and $\bar{\nu}_\mu$ events for each E_μ^{obs} bin as a function of $\cos\theta_\mu^{obs}$ for $\alpha_3 = 0, 1 \times 10^{-5}$ and 1×10^{-4} eV^2 as representative values. $\cos\theta_\mu^{obs}$ = 0-1 represents the up coming neutrinos.

In the sensitivity measurements of the decay parameter (α_3), we have assumed neutrino decay with oscillation in the theory and fitted with data where only oscillation is assumed. In our analysis we have taken charge current interaction data while ignoring the neutral current events. The sensitivity of the decay parameter $\alpha_3 = \frac{m_3}{\tau_3}$ is shown in Figure 4 for both fixed parameter analysis and for marginalization of the oscillation parameters. The true value of the oscillation parameters and

their marginalization ranges have been summarized in Table 3. From Figure 4, we can see that marginalization of the oscillation parameters reduces the sensitivity of the decay parameter from fixed parameter analysis for any choice of hierarchy. This is because of the interplay of the mixing angle θ_{23} and the α_3 since both of them affect the amplitude of the neutrino oscillation.

Parameter	Central value	Marginalization range
θ_{13}	$8.5°$	$[7.80°, 9.11°]$
$\sin^2\theta_{23}$	0.5	[0.39, 0.64]
Δm^2_{32}	2.366×10^{-3} eV^2	$[2.3, 2.6]\times 10^{-3}$ eV^2 (NH)
$\sin^2\theta_{12}$	0.304	Not marginalized
Δm^2_{21}	7.6×10^{-5} eV^2	Not marginalized
δ_{CP}	$0°$	Not marginalized

Table 3: Oscillation parameters used in this analysis. For fixed parameter studies all parameters are kept at their central values. While applying marginalization, only the parameter for which the sensitivity study is being performed is kept fixed and the others are varied in their respective 3σ ranges.

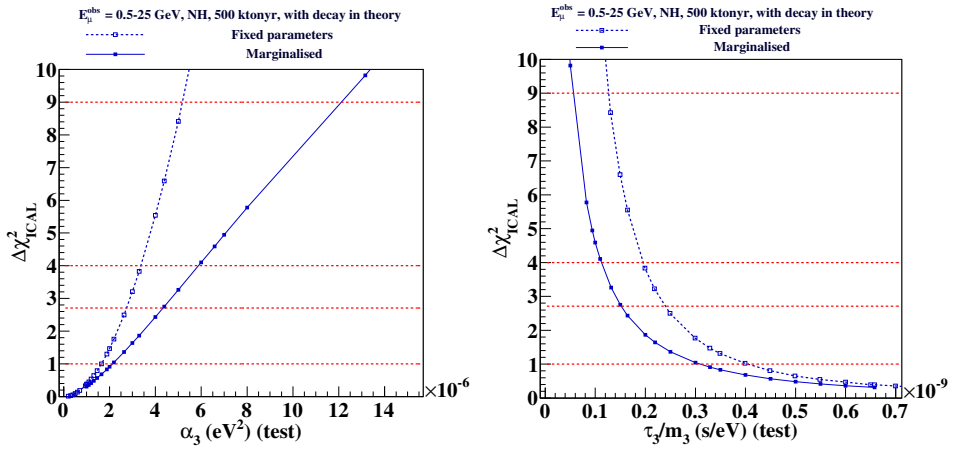

Figure 4: Bounds on the allowed values of (left) α_3 eV^2 (right) τ_3/m_3 (s/eV) with 500 kt year exposure of ICAL with NH as true hierarchy. Both fixed parameter and marginalized results are shown for comparison.

The 90% CL results provide the lower bound on $\frac{\tau_3}{m_3} > 1.51 \times 10^{-10}$ s/eV which translate to the upper bound of $\alpha_3 < 4.36 \times 10^{-6}$ eV^2. These bounds from ICAL are at least two orders of magnitude tighter than the MINOS bound [33] where at 90% CL, $\frac{\tau_3}{m_3} > 2.8 \times 10^{-12}$ s/eV which translates to $\alpha_3 < 2.34 \times 10^{-4}$ eV^2 and comparable to the limit provided by the global analysis of full atmospheric data

from Super-Kamiokande with long baseline experiments K2K and MINOS [32]. The bound on $\frac{\tau_3}{m_3}$ depends on the true hierarchy and the above mentioned bound is for NH and will change if one considers IH to be the true hierarchy.

The effect of decay on the precision measurements of the oscillation parameters is shown in Figure 5 where both data and theory assumes decay with $\alpha_3 = 1\times10^{-5}$ eV^2. In the marginalization, α_3 is varied in 3σ ranges i.e. [0,2.35 $\times 10^{-4}$] eV^2. The 1σ precision of a parameter β is defined as

$$p(\beta) = \frac{\beta_{max(2\sigma)} - \beta_{min(2\sigma)}}{4\beta_{\text{true}}} \tag{5}$$

where, $\beta_{max(2\sigma)}$ and $\beta_{min(2\sigma)}$ are the maximum and minimum allowed values of β at 2σ with β_{true} being the true choice.

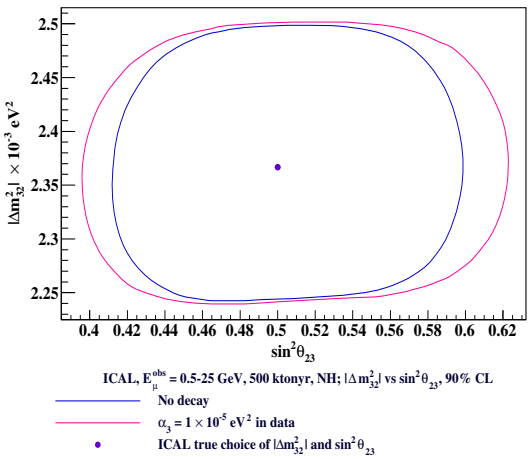

Figure 5: Expected 90% C.L. contour in the $\sin^2\theta_{23} - |\Delta m^2{}_{32}|$ plane, with and without decay, for NH. The value of α_3 in "data" is taken as 1×10^{-5} eV^2.

From Figure 5, we can see that precision measurements of the standard oscillation parameters worsen in presence of decay. While the precision on $|\Delta m^2_{32}|$ changes marginally from the no decay value of 5.35% to 5.46%, the effect is more in case of $\sin^2\theta_{23}$ where precision worsen to 22.3% as compared to 18.5% while considering decay.

We have also studied the mass hierarchy determination sensitivity of ICAL in

α_3 eV^2	$\Delta\chi^2$ (NH$^{\text{true}}$)	$\Delta\chi^2$ (IH$^{\text{true}}$)
0	7.92	9.17
6×10^{-6}	7.37	7.36
1×10^{-5}	7.11	7.07
2.35×10^{-4}	5.19	5.10

Table 4: Mass hierarchy sensitivity values $\Delta\chi^2$ obtained with 500 kt year exposure of ICAL with true NH/IH. $\sin^2\theta_{23}^{\text{true}} = 0.5$ has been taken for the analysis.

presence of invisible neutrino decay. Data events are generated assuming NH(IH) as true hierarchy in presence of decay and fitted with opposite hierarchy IH(NH). While calculating marginalized χ^2, the test parameters are varied in the range shown in Table 3. The reduction of oscillation amplitude in the presence of decay reduce the number of events as compared to no decay. This reduces the hierarchy sensitivity as shown in Figure 6. The marginalized hierarchy sensitivities that can be achieved with 500 kt-yr of ICAL is summarized in Table 4 [34].

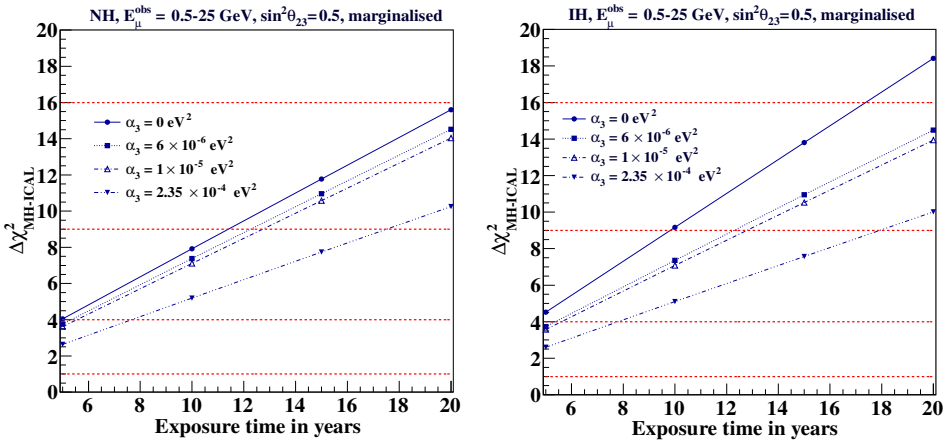

Figure 6: Mass hierarchy sensitivity of ICAL as a function of exposure time of 50 kt ICAL. The left(right) plot assume NH(IH) as true hierarchy. Hierarchy sensitivity is shown with three decay constant $\alpha_3 = 6 \times 10^{-6}$, 1×10^{-5} and 2.35×10^{-4} eV^2. The no decay hierarchy sensitivity is shown with $\alpha_3 = 0$.

Summary and future scope

The INO ICAL detector is mainly designed to measure mass hierarchy and precision measurement of the parameter Δm^2_{31} and θ_{23} by using a magnetized iron calorimeter

and resistive plate chambers as active detector materials. The physics of matter effect with wide range of $(\frac{L}{E})$ and the ability to distinguish μ^- and μ^+ and therefore the ability of separating ν_μ from $\bar{\nu}_\mu$, puts INO in the global arena of neutrino study. INO is insensitive to $\delta_{\rm CP}$ whereas long baseline experiments are sensitive to $\delta_{\rm CP}$. So adding INO with long baseline experiment can help to remove some of the degeneracies faced by individual experiments and thus improve the sensitivity of the oscillation parameters. In our study, we have explored how the hierarchy and octant sensitivity of ESSνSB , which is primarily aimed for CP discovery, can improve by adding INO. We also add the information from the current LBL experiments T2K and NOνA assuming their full projected runs. Various synergies between these experiments and the interplay between neutrino and anti-neutrino boost the overall sensitivity. We have shown the results with various hierarchy-octant scenarios as a function of $\delta_{\rm CP}$ (true). The combined mass hierarchy sensitivities can reach to $\sim 5\sigma$ for most of the true hierarchy-octant combinations. Although INO has very little octant sensitivity, but $2-3\sigma$ octant sensitivity can be achieved when combing with T2K and NOνA experiments. Due to rapid variation of sensitivities of ESSνSB with $\delta_{\rm CP}^{\rm true}$, the overall shape and the position of the minimum is decided by ESSνSB when combing with other experiments and the combined sensitivities can reach up to $\sim 3\sigma$ for LO and $\sim 2\sigma$ for HO.

We have also explored the capabilities of INO ICAL detector in constraining the invisible decay of the neutrinos. Using the full three flavour analysis with matter effect, we are able to put bounds on the lifetime of the decaying mass eigen state with the parameter $\alpha_3 = \frac{m_3}{\tau_3}$ where the mass eigenstate decays with rest frame lifetime τ_3. With only CC events and by using atmospheric neutrinos with higher $(\frac{L}{E})$, INO can put severe constraints on the decay parameters. In our analysis we have shown it is possible for INO with 500 kt year exposure to put upper bounds on $\alpha_3 < 4.36 \times 10^{-6}$ eV^2 for 90% CL which is two orders of magnitude better than MINOS charge and neutral current combined analysis. We have also discussed

the effect of decay on the precision measurements of the standard oscillation parameters. We have shown that decay affects the amplitude of oscillation and thus interferes with θ_{23} and in effect worsen the $\sin^2\theta_{23}$ precision from 18.5% to 22.3% with 90% CL from no decay case. The $|\Delta m^2_{32}|$ precision does not change much and changes from 5.35% to 5.46% when considering neutrino decay. The improvements of the detector resolution and the identification of hadrons could be beneficial in future for adding neutral currents along with charge current events to put even better bounds for the decay parameters. Mass hierarchy sensitivity is seen to get reduced as compared to no decay scenario because of the reduction of number of events while considering invisible decay of neutrino.

Future studies can include combination of INO and other LBL experiments to probe new physics beyond Standard Model.

List of Figures

List of Tables

List of Abbreviations

SM	Standard Model
BSM	Beyond Standard Model
MSW	Mikheyev-Smirnov-Wolfenstein
LO	Lower Octant
HO	Higher Octant
LMA	Large Mixing Angle
PREM	Preliminary Reference Earth Model
NSI	Non Standard Interaction
OMSD	One Mass Scale Dominance
CC	Charged-Current (interaction)
NC	Neutral-Current (interaction)
SSM	Standard Solar Model
CP	Charge conjugation and Parity (symmetry)
CPT	Charge conjugation, Parity and Time reversal (symmetry)
NH	Normal Hierarchy
IH	Inverted Hierarchy
QE	Quasi-Elastic
RES	Resonance
DIS	Deep Inelastic Scattering
U	Neutrino mixing matrix
PMNS	Pontecorvo Maki Nakagawa Sakata Matrix
ν_α, ν_β, ...	Neutrino flavour eigenstates (Greek indices)
ν_i, ν_j, ...	Neutrino mass eigenstates (Roman indices)
$P_{\alpha\beta}$	$\nu_\alpha \to \nu_\beta$ oscillation probability
Δm^2_{ji}	mass-squared differences $m^2_j - m^2_i$
θ_{12}, θ_{23}, θ_{13}	neutrino mixing angles
δ_{CP}	neutrino CP violating phase
G_F	Fermi's constant

INO	India-based Neutrino Observatory
SK	Super Kamiokande
SNO	Sudbury Neutrino Observatory
T2K	Tokai to Kamioka
MINOS	Main Injector Neutrino Oscillation Search
NuMI	Neutrinos at the Main Injector
NOνA	NuMI Off-Axis ν_e Appearance
ESS	European Spallation Source
KamLAND	Kamioka Liquid Scintillator Anti-neutrino Detector
OPERA	Oscillation Project with Emulsion-tRacking Apparatus
CERN	European Organization for Nuclear Research
LHC	Large Hadron Collider
LEP	Large Electron-Positron Collider
LNGS	Laboratori Nazionali del Gran Sasso
POT	Protons on Target
ICAL	Iron CALorimeter
RPC	Resistive Plate Chamber
TASD	Totally Active Scintillator Detector
DOM	Digital Optical Module
GEANT	GEometry ANd Tracking
GLoBES	General Long Baseline Experiment Simulator

Chapter 1

Introduction

1.1 Neutrino : The invisible particle

The introduction of neutrino as a particle goes far back to 1930 when Wolfgang Pauli proposed its existence for the first time as a "desperate remedy" [1] to solve the long standing problem of conservation of energy, momentum and angular momentum in the beta decay spectrum. The term *neutrino* was first coined by Enrico Fermi in 1934. The particle neutrino was hypothesized to be neutral in charge, to belong to the family of leptons with spin $\frac{1}{2}$ and massless. These properties make it very difficult to detect these particles. However, in 1954 neutrino was detected for the first time in the experiment conducted by Reines and Cowan [2, 35, 36]. From that time more and more experiments were designed to study it's behavior more closely and for the last 60 years it remained as one of the most puzzling particles in terms of it's nature and the difficulties in unravelling it's properties. Several experiments have been performed and many are still proposed to understand this elusive particle and neutrino physics remains an exciting field of research till date. The proposed India-based Neutrino Observatory (INO) is an effort to understand some of the properties of neutrinos by using atmospheric neutrinos as a source. In this chapter we will discuss about neutrinos, their sources, properties and the

understanding gathered about these from world wide efforts.

1.2 Neutrino sources

Neutrinos come with three different flavors and can be of different energies. Though the basic properties remain the same but they are broadly classified in few categories depending on their energy and their production points. Their various energy ranges and distances traveled from the point of production to the detector, have helped to explore different properties and cross verify the results between different experiments. Neutrinos not only come from the natural processes but can also be man made. The main sources are:

1.2.1 Relic neutrinos

Like the cosmic micro wave background radiation, there is a neutrino background having very low energies. These neutrinos got decoupled and their current temperature is estimated to be of 1.95 K. Very low interaction cross section in the sub-eV range along with the constraint of having a lower threshold for the experiment, makes it difficult to detect such neutrinos and this remains an open problem on its own.

1.2.2 Geo neutrinos

Neutrinos get produced from the beta decay of long lived natural radio isotopes found in Earth's interior like ^{238}U, ^{232}Th, ^{40}K. All these isotopes emit anti-neutrinos in the energy range of MeV. These neutrinos provide an insight into the Earth's structure and it's inner heating mechanism. The first measurements of such neutrinos came from the KamLAND experiment [37] and later verified by the Borexino experiment [38].

1.2.3 Solar neutrinos

Sun is an important source of neutrinos in the MeV energies. According to Standard Solar Model [39], neutrinos get produced through the fusion process of protons inside the sun. Each second, Earth receives about 65 billion solar neutrinos per square centimeter orthogonal to the direction of Sun [40]. The anomaly in the solar flux measurement was the first indication of neutrino oscillation [41].

1.2.4 Supernova neutrinos

When a massive star collapses, the matter densities at the core become so high ($\sim 10^{17}$ kg/m^3) that it breaks the degeneracies of electron producing neutron and electron neutrino. These kind of events are categorized as type Type II supernova [42, 43]. Neutrinos in the range of few MeV are produced in huge numbers (10^{57}) but their flux reduces by d^{-2} while reaching Earth (where d is the distance of the Earth from the supernova). So the detection of such neutrinos is only possible for Supernova events in the Milky Way and nearby galaxies [44]. The first neutrinos from SN1987a Type II supernova were observed by Kamiokande II, IMB and Baskan detector within a time span of 13 seconds.

1.2.5 Reactor neutrinos

Nuclear reactors are also one of the major sources of neutrinos in the MeV region. In reactors, different fissile materials are used such as ^{238}U, ^{235}U, ^{241}Pu, ^{239}Pu. All these radio active elements go through fission process and produce electron type anti-neutrinos with mean energy 3.5-4 MeV. In fact the first experimental verification of the existence of neutrinos [35] came from such neutrinos.

1.2.6 Atmospheric neutrinos

Neutrinos are also produced in the Earth's atmosphere. Isotropic cosmic particle flux come with all energies from MeV to TeV. They interact with the air molecules in the atmosphere and produce unstable particles (mostly pions and kaons) which further decay and produce electrons and muon type neutrinos. As a result, the energies of the atmospheric neutrinos span from as low as 0.1 MeV to few TeV, making the flux peaked at 0.25 GeV and falls with $E^{-2.7}$ in the higher energies. INO experiment is designed to detect such neutrinos in the GeV energy range.

1.2.7 Accelerator neutrinos

Accelerator neutrinos are another example of neutrinos from man made sources. In the accelerator experiments, high energetic protons are smashed on a fixed target made of graphite sheet to produce heavier unstable particles. These particles are focused using magnetic horns and allowed to decay in long decay pipe and thus produce neutrinos with desired flavour and type (neutrinos and anti-neutrinos). Although the production mechanism is similar to that of atmospheric neutrinos but a higher flux of neutrinos can be obtained of relatively known energies and known direction.

1.2.8 Galactic and extra galactic neutrinos

These neutrinos are produced from the decay of charged cosmic particles those are accelerated in the active galactic medium or in gamma ray burst. The reason for such high energetic acceleration is little understood. But neutrinos being neutral does not bend while crossing the high magnetic galactic medium thus providing a direct way to locate and study the sources of such high energetic processes. The energies of such neutrinos varies from TeV to PeV. Baikal, AMANDA, IceCube, ANTARES are few such experiments designed to study such high energetic neutri-

nos.

1.3 Neutrinos and the Standard Model

The Standard Model (SM) of particle physics is a well accepted and celebrated model explaining the particle content and fundamental forces in nature. The SM explains all the three forces in nature i.e. weak, electromagnetic and strong forces (Gravitational forces are not included in SM). The SM as we know today was developed in various stages and the final form of the Glashow-Weinberg-Salam SM came in 1967. The SM, based on $SU(3)_C \times SU(2)_L \times U(1)_Y$ gauge groups, successfully predicted the neutral current and the existence of Z boson [45]. The Higgs mechanism is responsible to give mass to the gauge boson and fermions [46–51]. SM contains total 12 spin $\frac{1}{2}$ fermions (6 leptons and 6 quarks with three colors) with their associated anti-particles and four spin-1 fundamental force carriers. The first success of SM came in 1971 with the Gargamelle experiment at CERN in which neutral current neutrino interaction was first discovered [52–54] and later confirmed by Fermilab [55]. According to the SM, all the fermions and the force carriers W and Z boson acquire mass through the interaction with the Higgs field. The further success of SM came after the experimental verification of the Higgs boson at the LHC in 2012 [56, 57]. The precision tests of the SM reveal the total number of the active neutrino species to be three by measuring the invisible decay width of the Z boson by LEP experiment at CERN [58–61]. Goldhaber experiment [62] has shown neutrinos are left handed while the anti-neutrinos are right handed particles. Neutrinos can only interact through the weak force either by charged current (CC), mediated by $W^{\pm}$ boson or through neutral current (NC), mediated by Z boson. In the SM, neutrinos are assumed to be massless and flavor is conserved. However, observation of neutrino oscillation, a phenomenon through which neutrino changes it's flavour established that neutrinos are massive although with very tiny

mass. But due to the absence of right handed neutrinos, generating mass terms for neutrinos are beyond the scope of the SM. Thus the study of neutrinos play an important role to probe physics beyond the SM and for the exploration of new physics.

1.4 Neutrino oscillation

The idea of neutrino oscillation was first proposed by B. Pontecorvo in 1950 [63, 64]. Neutrino oscillation happens because of the rotation of the flavor states and the mass eigenstates. The flavour states ($|\nu_\alpha>$, $\alpha = e, \mu, \tau$), take part in the weak interactions and can be expressed as a linear superposition of the mass eigenstates ($|\nu_i>$, i = 1,2,3). This is possible through the unitary matrix U which is sometimes referred to as the PMNS matrix named after Pontecorvo, Maki, Nakagawa and Sakata [65, 66]. The flavour and the mass eigenstates of the neutrinos are related through

$$|\nu_\alpha>=\sum_i U^*_{\alpha i}|\nu_i> \tag{1.1}$$

The parameterization of the U matrix depends on the number of neutrino flavors considered. For example, when considering three flavour neutrino oscillation, PMNS matrix U can be described by three mixing angles (namely θ_{12}, θ_{23} and θ_{13}) and one complex phase $\delta_{\rm CP}$ which is responsible for CP violation in the neutrino sector [67]. For three flavour neutrino oscillation PMNS matrix can be expressed as

$$U = \begin{pmatrix} c_{12}c_{13} & s_{12}c_{13} & s_{13}e^{-i\delta_{\rm CP}} \\ -s_{12}c_{23} - c_{12}s_{23}s_{13}e^{i\delta_{\rm CP}} & c_{12}c_{23} - s_{12}s_{23}s_{13}e^{i\delta_{\rm CP}} & s_{23}c_{13} \\ s_{12}s_{23} - c_{12}c_{23}s_{13}e^{i\delta_{\rm CP}} & -c_{12}s_{23} - s_{12}c_{23}s_{13}e^{i\delta_{\rm CP}} & c_{23}c_{13} \end{pmatrix} \tag{1.2}$$

where, s_{ij} and c_{ij} are used to denote $\sin\theta_{ij}$ and $\cos\theta_{ij}$ respectively and θ_{ij} represents the mixing angle between the mass eigenstates. $\delta_{\rm CP}$ represents the CP violating

Dirac phase.

At the time of neutrino propagation, different mass eigenstates propagate with different velocities and they go out of phase with each other. This is the reason for getting a non zero probability of finding a neutrino with flavour ν_β starting with (t=0) a flavour ν_α. This probabilistic transformation depends on factors like the energy of the neutrinos, the path length traveled by the neutrinos and the medium in which they traveled.

The time evolution of the mass eigenstates can be expressed as

$$|\nu_i(t)>= e^{-iE_it}|\nu_i(0)> \tag{1.3}$$

where, $|\nu_i(0)>$ and $|\nu_i(t)>$ represents the mass eigenstate at time t = 0 and t= t respectively. The time evolution of the flavour state ν_α can be expressed as

$$|\nu_\alpha(t)>= \sum_{\beta=e,\mu,\tau}\left(\sum_i U^*_{\alpha i}e^{-iE_it}U_{\beta i}\right)|\nu_\beta> \tag{1.4}$$

From Equation 1.4, we can obtain the amplitude of getting the flavour ν_β after time t. The probability $P_{\alpha\beta}$ can be expressed as shown in Equation 1.5 where, neutrino of flavour ν_α of energy E will oscillate to another flavour ν_β after traversing the distance L.

$$P_{\alpha\beta} = \delta_{\alpha\beta} - 4\sum_{i>j}\Re[\square U_{\alpha\beta ji}]\sin^2\left(\frac{\Delta m^2_{ij}L}{4E}\right) + 2\sum_{i>j}\Im[\square U_{\alpha\beta ji}]\sin\left(\frac{\Delta m^2_{ij}L}{2E}\right) \tag{1.5}$$

where, $\square U_{\alpha\beta ji} = U^*_{\alpha i}U_{\beta i}U_{\alpha j}U^*_{\beta j}$, $\Delta m^2_{ij} = m^2_i - m^2_j$, m_i and m_j being the mass of the eigenstates ν_i and ν_j respectively.

Thus neutrino oscillation is possible only if neutrinos are massive and have distinct mass eigenvalues ($m_j \neq m_i$) as shown in Equation 1.5.

Using Equation 1.5, the neutrino conversion probability $P_{\alpha\beta}$ ($\alpha \neq \beta$) for neutrinos with energy E after traveling a distance L can be simplified for 2 flavour

vacuum oscillation as :

$$P_{\alpha\beta} = \sin^2 2\theta \sin^2 \left(\frac{\Delta m^2 L}{4E} \right) \tag{1.6}$$

where the 2×2 PMNS matrix is parameterized by a mixing angle θ as:

$$U = \begin{pmatrix} \cos\theta & \sin\theta \\ -\sin\theta & \cos\theta \end{pmatrix} \tag{1.7}$$

and the oscillation length is expressed as:

$$L_{\text{OSC}} = \frac{4\pi E}{\Delta m^2} \tag{1.8}$$

However, the oscillation probabilities change significantly from its vacuum behavior when considering the propagation through matter. While propagating through matter, the evolution equation gets modified significantly by the effective potential caused by the interaction with the medium through coherent elastic scattering. As a result, CC interaction for only $\nu_e's$ and NC interaction for all flavours get modified. This leads to change in the effective mixing angle and mass squared differences in the neutrino parameterization. As a result the 2 flavour vacuum oscillation probability as shown in Equation 1.6 gets modified in the presence of matter as :

$$P_{\alpha\beta} = \sin^2 2\theta_m \sin^2 \left(\frac{\Delta m^2_m L}{4E} \right) \tag{1.9}$$

where, θ_m and Δm^2_m are matter modified mixing angle and the mass squared differences respectively. These modification are due to the effective matter potential $A = 2\sqrt{2} G_F n_e E = 7.63 \times 10^{-5}\ \text{eV}^2 \left(\frac{\rho}{\text{gm/cc}} \right) \left(\frac{\text{E}}{\text{GeV}} \right)$ where, G_F is the Fermi constant, n_e is the number density of electrons present in matter, E being the neutrino energy expressed in GeV and ρ is the matter density expressed in gm/cc. The modified θ_m and Δm^2_m can be expressed as a function of A, mass squared differences

and the mixing angle in vacuum as shown in Equation 1.10.

$$\begin{aligned} \Delta m^2_m &= \sqrt{(-A + \Delta m^2 \cos 2\theta)^2 + (\Delta m^2 \sin 2\theta)^2} \\ \tan 2\theta_m &= \frac{\Delta m^2 \sin 2\theta}{-A + \Delta m^2 \cos 2\theta} \end{aligned} \tag{1.10}$$

Few salient features of Equation 1.10 are worth mentioning.

- To have neutrino oscillation, both the mixing angle and the mass square difference need to be non zero.
- When $A = \Delta m^2 \cos 2\theta$, matter modified mixing angle θ_m becomes $\frac{\pi}{4}$ making the oscillation probability maximum irrespective of the value of the vacuum mixing angle θ. This mechanism is known as Mikheyev - Smirnov - Wolfenstein (MSW) resonance [68, 69].
- Effective matter potential A is positive for neutrinos but changes sign for anti-neutrinos. So for neutrinos, matter resonance happens when $\Delta m^2 > 0$ but the opposite is true for anti-neutrinos where $\Delta m^2 < 0$.

In the case of three flavours, mixing angles get modified in similar fashion although the expressions become complicated and the probabilities are solved numerically. In three flavour, complex phase δ_{CP} also plays a crucial role while calculating the probabilities. From Equation 1.5 it is clear that the amplitude of neutrino oscillation is dictated by the mixing angle θ_{ij} whereas the frequency of oscillation is determined by the mass squared differences Δm^2_{ji}. Oscillation also depends on the neutrino energy E and the path length L from the source to the detector and the density (ρ) of the medium it passes through. $\mathrm{L_{OSC}}$ also plays an important role while planning any experiment.

Oscillation experiments are designed to extract the information of the mixing angle and the mass squared differences. For example, θ_{12} and Δm^2_{21} are extracted

from the solar and long baseline reactor experiments and in general referred as θ_{sol} and Δm^2_{sol} respectively. Similarly, θ_{23} and Δm^2_{32} are obtained from the atmospheric and accelerator based experiments and are termed as θ_{atm} and Δm^2_{atm} respectively. Mixing angle θ_{13} is referred as θ_{REACTOR} as this value is obtained from reactor neutrino experiments.

1.5 Present status of the neutrino oscillation parameters

The current best fit values from global analysis of world neutrino data is summarized in Table 1.1 [70, 71]. Note that these values get updated with new results and new data. Some of the parameter values that are used in our analysis may be different and will be mentioned in their respective analysis chapters.

Parameters	**Normal Hierarchy**		**Inverted Hierarchy**	
	bfp $\pm$ 1σ	3σ **range**	**bfp** $\pm$ 1σ	3σ **range**
$\sin^2\theta_{12}$	$0.307^{+0.013}_{-0.012}$	$0.272 \to 0.346$	$0.307^{+0.013}_{-0.012}$	$0.272 \to 0.346$
θ°_{12}	$33.62^{+0.78}_{-0.76}$	$31.42 \to 36.05$	$33.62^{+0.78}_{-0.76}$	$31.43 \to 36.06$
$\sin^2\theta_{23}$	$0.538^{+0.033}_{-0.069}$	$0.418 \to 0.613$	$0.554^{+0.023}_{-0.033}$	$0.435 \to 0.616$
θ°_{23}	$47.2^{+1.9}_{-3.9}$	$40.3 \to 51.5$	$48.1^{+1.4}_{-1.9}$	$41.3 \to 51.7$
$\sin^2\theta_{13}$	$0.02206^{+0.00075}_{-0.00075}$	$0.01981 \to 0.02436$	$0.02227^{+0.00074}_{-0.00074}$	$0.02006 \to 0.02452$
θ°_{13}	$8.54^{+0.15}_{-0.15}$	$8.09 \to 8.98$	$8.58^{+0.14}_{-0.14}$	$8.14 \to 9.01$
δ°_{CP}	234^{+43}_{-31}	$144 \to 374$	278^{+26}_{-29}	$192 \to 354$
$\frac{\Delta m^2_{21}}{10^{-5}}$ (eV^2)	$7.40^{+0.21}_{-0.20}$	$6.80 \to 8.02$	$7.40^{+0.21}_{-0.20}$	$6.80 \to 8.02$
$\frac{\Delta m^2_{3l}}{10^{-3}}$ (eV^2)	$+2.494^{+0.033}_{-0.031}$	$+2.399 \to +2.593$	$-2.465^{+0.032}_{-0.031}$	$-2.562 \to -2.369$

Table 1.1: The three flavour global fit of the neutrino oscillation parameters. The values of the oscillation parameters in the first column are obtained assuming NH to be the true hierarchy whereas the second column reports the same but assuming IH to be the true hierarchy.

Table 1.1 depicts our understanding of oscillation parameters from the global

neutrino analysis. The knowledge of the oscillation parameters in the Solar sector i.e. the mixing angle θ_{12} and the solar mass squared differences Δm^2_{21} have been measured with high precision. The sign of $\Delta m^2_{21} > 0$ have been established from solar matter effect, proving the fact $m_2 > m_1$ [72]. Reactor angle θ_{13} have also been proven to be non zero with 5σ C.L. [73]. Atmospheric mixing angle θ_{23} have also been determined by atmospheric and accelerator experiments. However ambiguity regarding octant of θ_{23} still exists with possibilities of θ_{23} to be in lower octant (**LO** where $\theta_{23} < 45°$) and higher octant (**HO** when $\theta_{23} > 45°$). The sign of Δm^2_{3l} ($l = 1$ for NH and $l = 2$ for IH [74]) is also an open question leading to the possibility of normal hierarchy (**NH** where $\Delta m^2_{31} > 0$) or inverted hierarchy (**IH** when $\Delta m^2_{32} < 0$) as shown in Figure 1.1 [75] This is referred to as mass hierarchy problem in the neutrino physics and has remained as one of the most intriguing problem till now. Several world wide experiments are currently running and some are proposed to solve the neutrino hierarchy problem. India-based Neutrino Observatory (INO) is one such proposed experiment geared to solve mass hierarchy problem in neutrino physics. The leptonic phase $\delta_{\rm CP}$ is still unknown although global analysis of neutrino data from all the neutrino oscillation experiments indicates the leptonic CP phase $\delta_{\rm CP} \sim -90°$ [3, 76, 77].

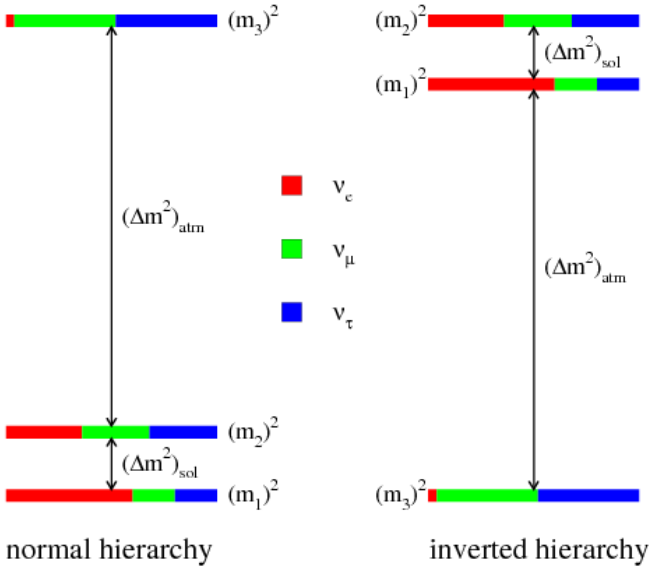

Figure 1.1: Schematic representation of the two possible mass hierarchy, NH (left) and IH (right). The figure shows the proportion of each flavour (ν_α) in the mass eigenstate (ν_i) where $\alpha = e, \mu, \tau$ and $i = 1, 2, 3$ [78].

1.6 Neutrino oscillation experiments

Neutrino physics has remained as one of the most exciting fields till date and various experiments have contributed in enhancing our knowledge about its properties. Several complementary experiments are designed by using different sources of neutrinos with different energies to unravel their properties. In this section I discuss the experiments that contributed in establishing neutrino oscillation and in precise determination of their parameters. I also discuss some of the current experiments and their salient features.

1.6.1 Homestake

Homestake experiment [41, 79–81] was designed to study solar neutrinos and measurement of it's flux. The experiment operated continuously from 1970 to 1994. By radiochemical measurement technique of neutrino capture ($\nu_e + {}^{37}\mathrm{Cl} \rightarrow {}^{37}\mathrm{Ar} + \mathrm{e}^-$), Homestake experiment was able to measure only one third of the predicted neutrino flux [82]. This led to the famous "*solar neutrino problem*" indicating flavour

transformation of neutrinos.

1.6.2 GALLEX & SAGE

GALLEX or Gallium experiment [83] was also a radiochemical neutrino experiment ($\nu_e + {}^{71}\text{Ga} \rightarrow {}^{71}\text{Ge} + e^-$) that ran between 1991 and 1997 at the Laboratori Nazionali del Gran Sasso (LNGS) situated inside the 2912 meters high Gran Sasso mountain. The rock equivalent of 3200 meters of water (mwe) acted as cosmic ray shield. Using gallium based solution in the detector as target material, GALLEX experiment was able to achieve the low threshold of 233 KeV for neutrino detection and thus able to detect the neutrinos emitted in the initial proton fusion reaction of the proton-proton chain reaction with an upper energy level of 420 KeV.

SAGE experiment is a deep underground laboratory of the Baskan Neutrino Observatory in the Northern Caucasus mountain range which provides good background shielding equivalent of 4700 mwe. Using 50 ton mass of metallic gallium in the gallium-germanium neutrino telescope, SAGE experiment was able to put bounds on the solar flux using the capture rate by Ga [84, 85] which is half of the Standard Solar Model prediction and therefore supported the solar neutrino shortfall.

1.6.3 Kamioka Observatory

The Kamioka observatory is a neutrino laboratory located underground in the Mozumi mine of the city of Hida in Japan. Kamiokande was proposed to study proton decay lifetime [86]. However, while measuring the background for this, they found an anomaly in the atmospheric neutrino flux ratio [87], a departure from the predicted value. This initiated the atmospheric neutrino problem. Using cylindrical water Ĉherencov detector, it could also detect the solar neutrinos ($\nu_e + e^- \rightarrow \nu_e + e^-$) and confirmed that neutrinos are coming from the Sun. The detected only half of the neutrinos as compared to the Statndard Solar Model pre-

diction corroborated the solar neutrino shortfall. During its run time, Kamiokande detector also observed 11 neutrinos produced by Supernova 1987a. Kamiokande also measured the ratio of the electron and muon neutrino flux and the deviation of the measured ratio from the theoretical prediction gave rise to atmospheric neutrino deficit problem.

To resolve the solar and atmospheric neutrino anomaly and to put bounds on the proton decay, Super Kamiokande (SK) detector, upgraded version of Kamioka, was designed with 50 kt water as a detector target material with 11200 photo multiplier tube to record the signal of neutrino interactions. Using larger statistics, SK was able to measure the zenith angle dependence of atmospheric neutrinos. Both $\nu_\mu \rightarrow \nu_e$ and $\nu_\mu \rightarrow \nu_\tau$ were considered to explain the oscillation phenomenon but $\nu_\mu \rightarrow \nu_\tau$ oscillation was favoured with a higher statistical significance [88] and the leading effect to solve the atmospheric neutrino problem. It also measured the solar neutrino spectrum and confirmed the solar neutrino shortfall and contributed in pin pointing the Large Mixing Angle (LMA) solution [89, 90] to the standard solar neutrino problem.

1.6.4 Sudbury Neutrino Observatory (SNO)

Sudbury Neutrino Observatory experiment [91–93] was designed to resolve the long standing "*solar neutrino problem*" by using heavy water as target material. With various interactions of neutrinos with D_2O, it was not only able to probe the charged current (CC) interactions of the electron neutrinos, as had been done by the other experiments, but also the neutral current (NC) interactions for all neutrino flavours. SNO experiment conclusively established the presence of other flavors to which electron type neutrinos coming from Sun have oscillated into, thus confirming the Standard Solar Model (SSM) and resolved the *solar neutrino problem* by measuring the $\frac{\text{CC}}{\text{NC}}$ ratio to be less than 1 [94]. Measurement of NC reaction rate of the total flux of ^{8}B was also consistent with the SSM prediction.

1.6.5 Borexino

Borexino is the most radio-pure scintillator detector till date planned to study the individual solar neutrino flux and to validate *Standard Solar Model*. Borexino has the capability to study geo-neutrinos [38] and also supernova neutrinos. This makes Borexino, a member of Supernova Early Warning System [95]. In 2017, Borexino provided the first widespread spectroscopic measurement of the solar neutrino spectrum measuring ^{7}Be, pep and pp neutrino flux. These measurements reached a precision of up to 2.7% for beryllium solar neutrinos and established a 5σ confirmation of the presence of pep neutrinos [96].

1.6.6 The Main Injector Neutrino Oscillation (MINOS)

MINOS is an accelerator based neutrino experiment with two detectors, one near detector located 1 km away from the NuMI facility at Fermilab which acts as neutrino source and a far detector positioned 735 km away at the Soudan Underground laboratory. MINOS was designed to put limits on the atmospheric parameters related to neutrino oscillation i.e. θ_{23}, Δm^2_{32}. Using the exposure of 7.25×10^{20} protons on target (POT), MINOS put the bound with 90% C.L. on $\Delta m^2_{32} = 2.32^{+0.12}_{-0.08} \times 10^{-3}$ eV^2 and $\sin^2(2\theta_{23}) > 0.9$ [97].

1.6.7 Tokai to Kamioka (T2K)

T2K [98] is an accelerator based experiment to probe oscillation parameters in the atmospheric sector. T2K uses SK detector along with a near detector to reduce the uncertainty in the initial neutrino flux. This improves the precision measurements of the oscillation parameters. T2K can measure various interaction cross sections using its near detector and also the CP violation phase $\delta_{\rm CP}$ in the neutrino sector [99]. In 2017, based on a total data set of 2.25×10^{21} POT and with the inclusion of electron anti neutrino disappearance data from reactor experiments, T2K

excludes CP conservation at the 2σ confidence level. The 95% allowed region for CP violating phase , $\delta_{\rm CP}$, is $[-171°; -34°]$ ($[-88°; -68°]$) for the normal (inverted) hierarchy, with the best fit point being $-105°$ ($-79°$) [100].

1.6.8 NuMI Off-Axis ν_e Appearance (NOνA)

NOνA [101] is a successor of MINOS which uses the same beam from NuMI facility like MINOS does. NOνA uses both near detector ($\sim$ 1 km from neutrino source) and far detector located 810 km from the source. It uses a Totally Active Scintillator Detector (TASD) to study the ν_e appearance from the original ν_μ beam and therefore can measure θ_{13} and the CP violating phase $\delta_{\rm CP}$. The experiment is also designed to resolve some of the open questions in neutrino physics like mass hierarchy by studying ν_μ disappearance and ν_e appearance. In 2018, using exposure of 8.85×10^{20} POT and with combined ν_μ disappearance and ν_e appearance, NOνA experiment give the best fit point as normal hierarchy, $\Delta m^2_{32} = 2.44 \times 10^{-3}$ eV^2, $\sin^2\theta_{23} = 0.56$ and $\delta_{\rm CP} = 1.21\pi$. The 68.3% confidence intervals in the normal hierarchy are $\Delta m^2_{32} \in [2.37, 2.52] \times 10^{-3}$ eV^2, $\sin^2\theta_{23} \in [0.43, 0.51] \cup [0.52, 0.60]$, and $\delta_{CP} \in [0, 0.12\pi] \cup [0.91\pi, 2\pi]$. The inverted mass hierarchy is disfavored at the 95% confidence level for all choices of the other oscillation parameters [102].

1.6.9 Kamioka Liquid Scintillator Anti-neutrino Detector (KamLAND)

KamLAND is a liquid scintillator based reactor experiment to study the survival probability of $\bar{\nu}_e$ [103] at a distance of 180 km from the source. KamLAND is well suited to study and precise determination of the oscillation parameters related to solar sector i.e. θ_{12} and Δm^2_{21} [104, 105]. Using 162 ton.yr exposure, KamLand was the first experiment to conclusively establish Large Mixing Angle (LMA)-MSW solution of the solar mixing angle [103]. KamLAND also has the capability to study

geo-neutrinos and was the first to report about them [106].

1.6.10 Daya Bay

Daya bay is a reactor based experiment comprising of total eight scintillator detectors and use the anti-neutrino flux from six nuclear reactors. Designed to measure the reactor angle θ_{13}, Daya Bay confirmed the non-zero value of this parameter with 5.2σ [73] discovery potential. Double Chooz [107, 108] and RENO [109, 110] experiments are reactor based experiments which also reported a non-zero θ_{13}.

1.6.11 IceCube Neutrino Observatory

IceCube is a neutrino observatory situated in the South pole Antarctic. The detector is located inside 1.5 km beneath the ice sheet to reduce the cosmic background. The whole detector uses 1 km^3 of antarctic ice as a target material and digital optical modules (DOM) to collect the signal of neutrino interactions using Ĉherencov light. The aim of this detector is to study high energy neutrinos (TeV-PeV) coming from terrestrial and extra terrestrial sources and to help in understanding the mechanism behind the production of such high energetic particles and their production zones, thus acting as a neutrino telescope [111–114] with other complementary experiments like KM3NET [115], ANTARES [116]. Several events have already been observed with the neutrino energy extending to PeV [117]. IceCube also shows promise in determining mass hierarchy, octant of θ_{23} [118], indirect dark matter searches [119, 120] and resolution of sterile neutrinos [121].

1.6.12 Oscillation Project with Emulsion-tRacking Apparatus (OPERA)

OPERA is a long baseline experiment to study the oscillation $\nu_\mu \rightarrow \nu_\tau$ using nuclear emulsion detector at Gran Sasso, Italy using the ν_μ beam from CERN with their

total journey of 730 km. OPERA is the first experiment to detect ν_τ [122] from ν_μ beam providing insight on the $P_{\mu\tau}$ oscillation channel.

Apart from the experiments mentioned above, several experiments are proposed for further investigation and precision studies on neutrino oscillation parameters. The notable among such experiments intending to measure unknown oscillation parameters are Hyper-Kamiokande [123], PINGU [124], INO [125], JUNO [126], DUNE [127], T2HK [11], T2HKK [12], ESSνSB [22]. Other than the oscillation physics and the oscillation parameter study, several world wide experiments are going on and proposed to measure the absolute mass scale of the neutrinos [128], their type - Dirac or Majorana [129, 130]– this is beyond the scope of the present study.

1.7 The scope of INO in the race

One of the main aim of India-based Neutrino Observatory (INO) is to determine the sign of Δm^2_{32} by exploiting the matter effect of the atmospheric neutrinos where neutrinos and anti neutrinos behave differently while propagating in Earth. For this the collaboration proposes to use a large (with total mass of 50 kt) magnetized iron calorimeter (ICAL) with simple repetitive geometry and using novel idea of distinguishing ν_μ from $\bar{\nu}_\mu$ by identifying μ^- and μ^+ respectively because of the charge identification capability owing to the magnetic field. INO will also do precision study of θ_{23} and Δm^2_{32}. Being an atmospheric neutrino experiment, INO will use the large combinations of energy (E_ν) and the path length (L_ν) to further explore beyond standard model (BSM) physics including the search of dark matter, magnetic monopole and the sterile neutrinos [125].

Chapter 2

The ICAL detector & atmospheric neutrinos in the ICAL detector

The India Based Neutrino Observatory (INO) is a proposed experiment to study atmospheric neutrinos. The detector is proposed to be a magnetized iron calorimeter (ICAL) which will be located in an underground location to reduce the cosmic ray background. Keeping in mind the requirement of low rainfall and low seismic zone, Bodi West Hills in Theni district of Tamilnadu is chosen as the site for the ICAL detector. The overall mountain rock coverage of 1 km gives an excellent shield from the cosmic muon background. In this chapter we will discuss the main components of the detector and it's working principle. We will also discuss the generation of atmospheric neutrino flux and its interaction in the detector.

2.1 ICAL detector

In this section we give a brief description of the ICAL detector including its geometry, the resistive plate chamber or RPCs which are the active detector components and the electro magnet.

2.1.1 ICAL geometry

ICAL is a modular detector with iron as the target material. Main active detector components are RPCs which will be sandwiched between the iron layers. Iron being an higher Z material is an ideal choice as the target material for neutrino interaction. Use of iron as the detector material also allows the possibility of magnetization. This inturn enables the detector to differentiate between the neutrinos and the anti-neutrinos. The whole detector is divided into three identical structures each with dimension 16 $m \times 16\ m \times 14.5\ m$ making the whole detector dimension 48 $m \times 16\ m \times 14.5\ m$. The detector height is composed of total 151 layers of iron where width of each iron layer is 5.6 cm. Identical 2 $m \times 2\ m$ RPC module accompanies the iron layer keeping a gap of 40 mm making total 150 layers of RPC to fill the whole ICAL height. This modular structure helps in replacing the detector parts and maintenance. The specifications of various parts of the detector are summarized in Table 2.1. All the signals generated from the neutrino interactions with the detector or the cosmic and random noise signal is registered in the RPC in different parts of the detector. The signals collected by each RPC through its pick up signal strips are channeled through the electronic cable to the front end and finally to the back end server for data processing and further analysis. Any signal registered in the pick up strips have position (x,y,z) co-ordinates attached to it and the timing information. (x,y,z) co-ordinate system gives an idea from which part of the detector the signal came from and the combination of (z-t) co-ordinate provides the timing and directionality of the signal. This information is very crucial to distinguish the direction of the incoming neutrinos i.e. up coming or down going. RPCs having good timing resolution $\sim$ 1 ns is sufficient for such jobs. All this information is further used in the calibration of the detector and to analyze the detector data.

No. of Modules	3
Modular dimension	16 m × 16 m × 14.5 m
Total dimension	48 m × 16 m × 14.5 m
No. of iron layers	151
Iron plate thickness	5.6 cm
Gap for RPC assembly	4 cm
Magnetic field	1.4 T
RPC unit dimension	174 cm × 183.5 cm × 1.8 cm
Readout strip width	2.8 cm
No. of RPCs/Road/Layer	8
No. of Roads/Layer/Module	8
No. of RPC units/Layer	192
Total RPC units	28,800
No. of electronic channels	$\sim 3.7 \times 10^6$

Table 2.1: Specifications of ICAL detector and its active detector components.

2.1.2 Resistive Plate Chamber (RPC)

RPC is the heart of the ICAL detector and the main active detector element. RPC works as a successor of spark chamber [131–134]. RPCs are made up of two high resistive plate with a small gas gap in between. A high electric field is maintained across the two glass plates to create a potential difference. In order to reduce the cost of experiments, INO plans to use glass plates to make RPC [135]. Graphite coating is done on the outer side of the glass plate so that high voltage electric field can be applied across the two glass plates. The size of each glass plate will be of $2\ m \times 2\ m$. Glass plates are joined together keeping the gap of 2 mm between them to allow the gas mixture to flow. This small gap is created by using polycarbonate cylindrical spacers with high bulk resistivity $10^{13}\ \Omega - cm$. At the time of operation if charged particle passes through the detector it will ionize the gas molecule. Because of the high electric field electrons and ions start to move in the opposite direction depending on the polarity of the electric field. Depending on the gas medium and the operating voltages RPC can work either in avalanche mode or in streamer mode. The two modes mainly differ in terms of signal output. So proper choices of the gas mixture and operating voltages are very important aspects. In the case of

INO, RPC is planned to operate in the avalanche mode. The gas mixture used in ICAL detector consists of Freon R134 as a target for ionizing particle, Isobutane to reduce the secondary avalanches by capturing secondary photons and SF_6 to limit the free charge in the medium [135, 136]. The signal is collected capacitively using the pick up strips arranged in X-Y position on the graphite painted outer walls separated by a myler sheet to avoid short circuit in the system. The time resolution achieved by this set up is of the order of ns which is adequate for current physics studies. Position resolution of mm order can be achieved by choosing the RPC readout strips width and the X-Y readout pattern in the RPC detector.

2.1.3 Magnet

The charged current (CC) interactions of neutrinos and anti-neutrinos produce charged particles with opposite polarities in the detector. In the presence of transverse magnetic field, moving charged particles bend depending on their polarity. So from the curvature of the final state particle it is possible to identify the polarity of the initial particle. For example in CC interaction if neutrino interacts with the detector medium it produces μ^- whereas anti-neutrino produces μ^+. In presence of transverse magnetic field the direction of curvature of the final state particle μ^- will be different from that of μ^+. In INO experiment, same principle is used to differentiate neutrino from its anti-neutrino counterpart. In ICAL detector high magnetic field ($\sim$ 1.5 T) is used with the help of toroidal shaped copper coil. As the ICAL detector itself is made of iron so the whole detector is magnetized using the electric current supplied through the copper coil. The momentum of a charged particle can be measured from the curvature in the magnetic field. From Figure 2.1, we can see the magnetic field structure in ICAL detector [10, 137]. Magnetic field changes its direction beyond $x \pm 4$m on two sides of the coil. In between the two coil slots (all total 8 $m \times 8$ m area in x-y plane), magnetic field is uniform and uni-directional. This region is called *central region* as shown in Figure 2.1. Beyond

the $x \pm 4$m i.e. outside the magnetic coil, the field changes its direction from the central region and called *side region*. The magnetic field in the side region is more or less uniform. But in the Y direction beyond $y \pm 4$m, i.e. the *peripheral region*, the magnetic field vary considerably both in magnitude and direction. Magnetic field is taken as zero in the gap between two iron plates and the magnetic field is assumed to be uniform over the whole iron plate. All the simulations and the detector properties (resolution, charge identification, efficiency etc.) are calculated using the simulation of the *central region* [10].

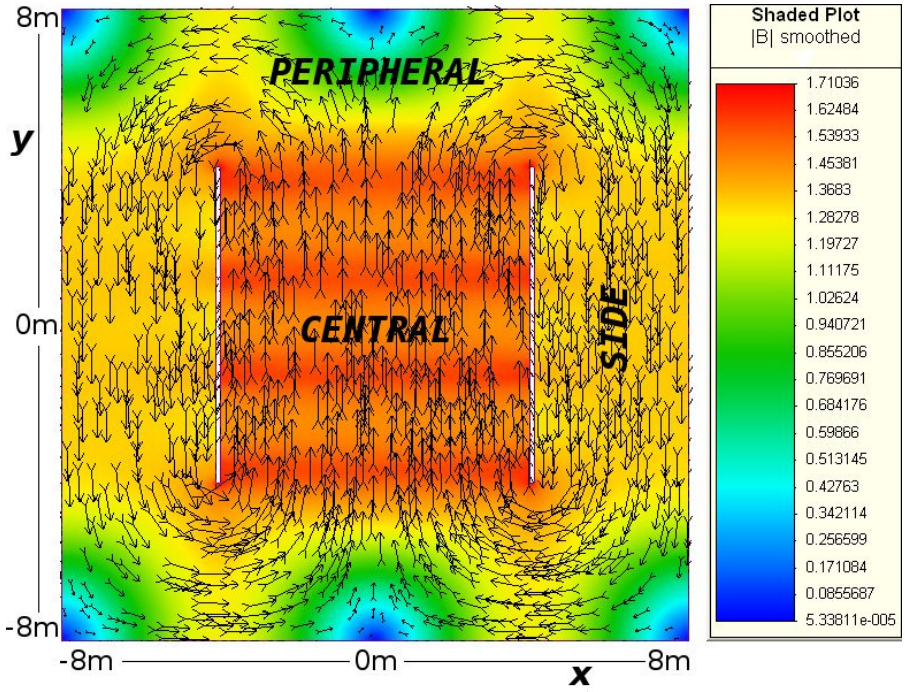

Figure 2.1: Magnetic field map used in ICAL experiment. The field map with arrows shows the magnetic field direction in the central plate of the central module generated by the MAGNET6 software. Magnetic fields are expressed in unit of Tesla and the intensity is shown using the color code. [10]

2.2 Atmospheric neutrinos

In this section we will discuss about the source of the atmospheric neutrinos and their interactions with the detector. But before going into the details let us first understand the events spectrum in any experiment. If particles with initial flux Φ

(i.e. $\frac{\text{no of particles}}{[L]^2[T]}$) interact with an ideal detector with cross section σ (i.e. $[L]^2$) then the number of events that will be registered in the detector per unit time = $\Phi \times \sigma \times N_d$, where N_d is the number of targets in the detector. So before planning an experiment it is very essential to know the flux of the initial particle. In INO experiment, atmospheric neutrinos are used as the initial flux. In this chapter we will explore the atmospheric flux production mechanism, their interaction cross section in the detector and the correlated physics.

2.2.1 Production of atmospheric flux

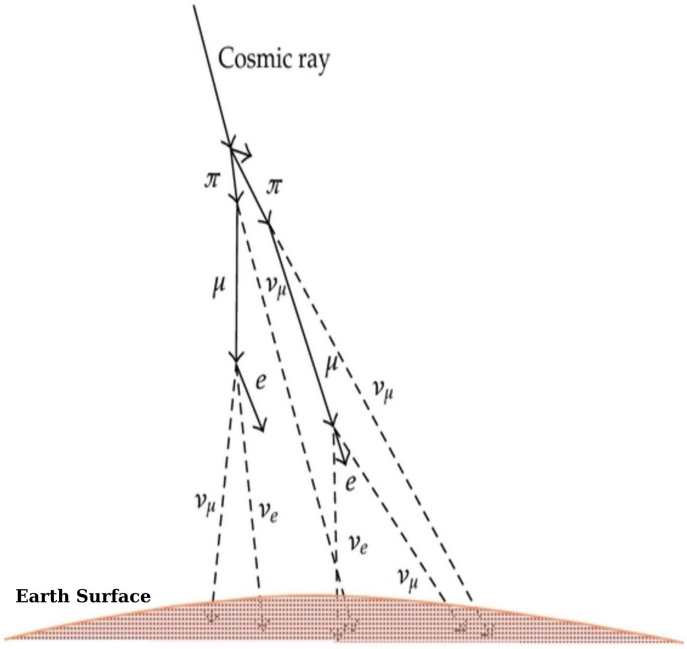

Figure 2.2: Schematic representation of atmospheric neutrino production process [138].

Earth's atmosphere is continuously bombarded with the energetic cosmic rays which are mostly protons. They come with all possible energies and direction from galactic and extra galactic sources. They can be extremely energetic $\sim 10^{10}$ GeV but the flux reduces exponentially with energy. When such cosmic particles enter the Earth atmosphere, they interact with the air molecules present in the

atmosphere. As a result lots of other unstable particles are produced which mainly consist of pions and also a fraction of kaons. These unstable particles decay to muon and electrons in chain reactions and produce neutrinos with electron and muonic flavour.

$$\begin{aligned} \pi^{\pm} &\rightarrow \mu^{\pm} + \nu_{\mu}(\bar{\nu_{\mu}}) \\ &\mu^{\pm} \rightarrow e^{\pm} + \bar{\nu_{\mu}}(\nu_{\mu}) + \nu_{e}(\bar{\nu_{e}}) \end{aligned} \tag{2.1}$$

where, $\pi^{\pm}$, $\mu^{\pm}$ and $e^{\pm}$ represent the positively and negatively charged pions, muons and electrons respectively and $\nu_{\mu}(\bar{\nu_{\mu}})$ represents the muonic neutrino (anti-neutrino). Similarly, electron neutrino and anti-neutrino are expressed with $\nu_{e}(\bar{\nu_{e}})$. Kaon channel also produces the muonic and electron neutrino and anti-neutrino in similar fashion. The cascade nature of neutrino production is shown graphically in Figure 2.2 [138].

From the production mechanism of neutrinos and anti-neutrinos in the atmosphere we have the final flux ratio (R) of ν_{μ} and ν_{e} as

$$R = \frac{\Phi_{\nu_{\mu}} + \Phi_{\bar{\nu}_{\mu}}}{\Phi_{\nu_{e}} + \Phi_{\bar{\nu}_{e}}} \approx 2 \tag{2.2}$$

The flux ratio R [139–141] is not a constant number. The value depends upon the number of muons that decayed into electron which in principle is decided by the energy of muon. The higher the energy of the muon, the lower would be the chances that it will convert into electron thus reducing the electron neutrino flux. The neutrino flux integrated over all possible directions and the dependency of R over neutrino energy is shown in Figure 2.3 [142–145].

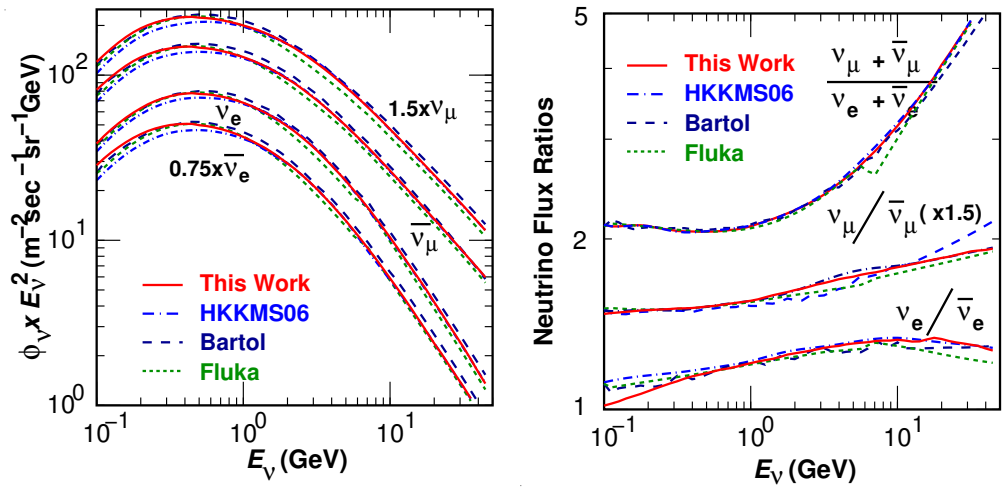

Figure 2.3: Atmospheric neutrino flux at Kamioka site [142], Japan averaged over all the directions [Left] and the muon-electron neutrino flux ratio [Right].

At higher energies ($E_\nu > 3$ GeV), the East-West effect of cosmic particles become negligible making the neutrino flux more symmetric given the particular direction of the Earth surface i.e. $\Phi_\nu(E_\nu, \cos\theta) = \Phi_\nu(E_\nu, -\cos\theta)$ where θ is the zenith angle. At lower energies ($E_\nu < 3$ GeV), Earth's geomagnetic property introduces some asymmetries in the zenith angle distributions of the neutrino flux. These properties are extensively studied by Super Kamiokande (SK) collaboration [146]. From Figure 2.4 [147], we can see that multi-GeV flux is symmetrical and peaked around $\cos\theta = 0$. Some deviation is expected and observed in the flux distribution for sub-GeV region. When assuming no-oscillation hypothesis, up going ($\cos\theta < 0$) and down going ($\cos\theta > 0$) flux should be symmetrical and same. So any deviation from this expected number will be a tell tell signature of neutrino oscillation. This asymmetry was measured by the SK collaboration which established the neutrino oscillation in atmospheric sector [147].

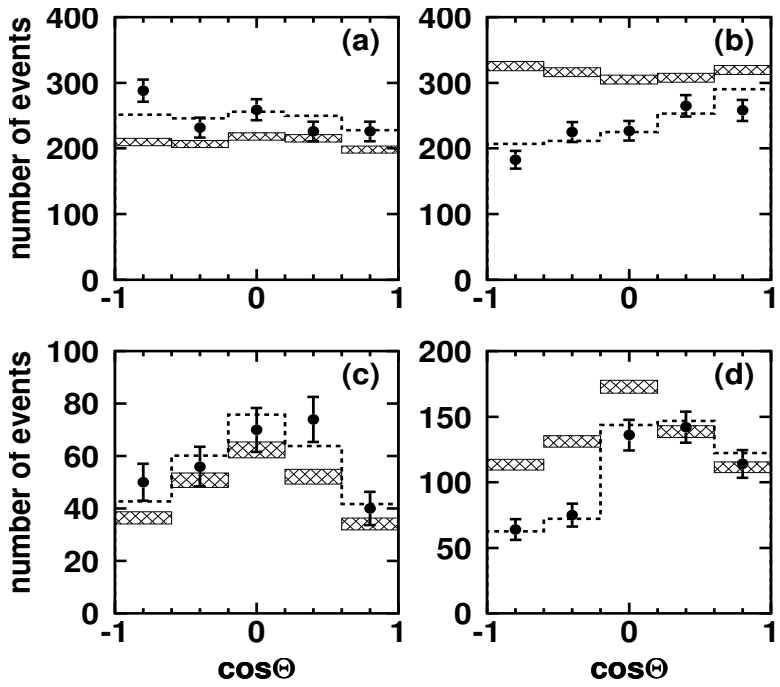

Figure 2.4: Zenith angle distribution observed in Super Kamiokande (summed over azimuthal angle) for a) sub-GeV e-like, b) sub-GeV μ-like, c) multi-GeV e-like, d) multi-GeV μ-like events. Events shown here contains both fully contained and partially contained events in the detector [147].

From Figure 2.4, we can see that at as we move from sub-GeV to multi-GeV, the flux become more symmetrical with the highest events centered around $\cos\theta = 0$. The shaded black lines represents the Monte Carlo (MC) simulation assuming neutrinos do not oscillate. Experimental data points are marked with error bars and the dotted line fits the data well assuming neutrino oscillation. The deviation from the MC results for multi-GeV upward going (i.e. for $\cos\theta < 0$) neutrinos implies conversion of ν_μ.

2.2.2 Atmospheric flux and uncertainty

Primary cosmic ray particles coming from terrestrial and extra terrestrial sources vary in energy from few MeV to TeV. As described earlier the atmospheric neutrinos are generated by the interaction of the air molecules with the cosmic ray particles. So atmospheric neutrino flux also comes with all energies in the range MeV-TeV. Having such wide range of energies and different path lengths traveled by neutrinos

before interacting with the detector, provide a unique opportunity to study varieties of physics at INO. But it is very crucial to have a deeper understanding of the neutrino flux structure and its uncertainties to find new physics and precision studies. The few key elements that introduce uncertainties in atmospheric neutrino flux measurements are:

- Atmospheric neutrinos come from the interaction of cosmic particles with the air molecules. So it is very crucial to first understand the flux of the primary cosmic particles. The primary cosmic ray flux in the 10 GeV to TeV energy range decreases with the power law $e^{-2.7}$. This in turn reduces the flux of the atmospheric neutrino flux in the higher energies. From the measurements of the cosmic flux up to tens of GeV, it is well known that cosmic flux is isotropic in nature before entering the Earth's atmosphere. The primary flux of the cosmic ray protons follow the relation:

$$\Phi(E) = K[E + b\mathrm{e}^{-\mathrm{c}\sqrt{\mathrm{E}}}]^{-\alpha} \tag{2.3}$$

  where, $\alpha = 2.74,\ K = 14900\ m^{-2}s^{-1}\mathrm{sr}^{-1},\ \mathrm{b} = 2.15\ \mathrm{GeV},\ \mathrm{c} = 0.21/\sqrt{\mathrm{GeV}}$ [146].

- The second source of uncertainty comes from the interaction models in the calculation of atmospheric flux. After entering the atmosphere, the primary cosmic particles go through hadronic interactions and produce pions, kaons along with the heavier molecules. In this stage hadronic interaction cross section is an essential input. These cross sections are measured world wide in accelerator experiments from low energy up to hundreds of GeV. For even higher energies these cross sections are mostly model dependent. As the atmospheric neutrino flux is a by product of these hadronic cross sections and the decay probabilities of such particles, errors on the calculation of primary source also propagate in the calculations of neutrino flux.

- Although the primary cosmic ray flux is isotropic before entering the Earth's atmosphere but the atmospheric neutrino flux is dependent on the latitude and longitude because of the Earth's geomagnetic effect and the time frame related to hadronic interactions and the decay of hadronic particles. So the modeling of the altitude dependence of interactions with air molecules in Earth's atmosphere and the Geomagnetic effect on the primary and secondary cosmic ray flux is very crucial and also introduces errors in the calculations of the atmospheric neutrino flux for a particular location in sub-GeV energy range.

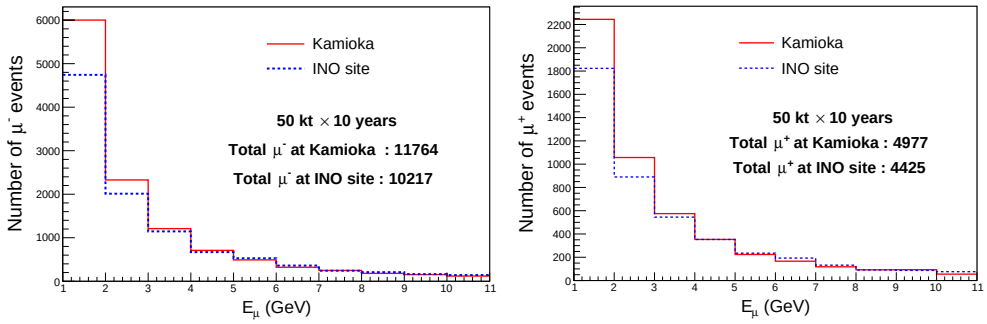

Figure 2.5: Comparison of μ^- (left) and μ^+ (right) events from un-oscillated neutrino flux in 500 kt-yr ICAL in two different locations, one in Theni, India and other is Kamioka site, Japan. The detector is assumed to be 100% perfect in detection, charge identification and energy resolution [125].

All the uncertainties discussed above affect the precision measurements of the atmospheric neutrino flux at the location of the detector. Typically all these factors introduce flux uncertainty of 15-20% in the overall normalization of neutrino flux.

All the calculations and results shown in this thesis assume the atmospheric flux at Kamioka site. From Figure 2.5, we can see there are no significant differences in events at high energies between the two sites. Since the total number of events at the INO site is $\sim 14\%$ smaller than the Kamioka site, so the precision results in determining θ_{23} will suffer which can be compensated by taking $\sim 14\%$ additional exposure [125]. But the mass hierarchy measurement will be unaffected as the main contribution comes from muons of high energy where INO flux is almost same as

Kamioka site.

2.2.3 Neutrino interaction cross section

In the previous section we have seen the properties of neutrino flux and associated uncertainties. Now we want to look at how the neutrino interacts with the detector material and its related physics. Atmospheric neutrino flux comprises of mainly two component ν_e and ν_μ. Neutrinos interact through matter with two types of interaction namely charged current (CC) interaction and neutral current (NC) interaction. In the CC interaction, neutrino interacts with detector material and produce same flavour charged particle along with hadrons whereas in NC interaction neutrino does not change its flavour but produce hadrons in the final state along with the neutrino. So depending on the type of interactions there will be hadrons produced in the detector along with associated leptons (CC interaction only) and the job of the detector is to identify the hadrons and leptons and to separate them. The summary of the CC and NC interaction is given in Table 2.2.

Charged Current Interaction (CC)	Neutral Current Interaction (NC)
$\nu_l + N \rightarrow l^- + X$	$\nu_l + N \rightarrow \nu_l + X$
$\bar{\nu_l} + N \rightarrow l^+ + X$	$\bar{\nu_l} + N \rightarrow \bar{\nu_l} + X$

Table 2.2: The CC and NC interactions of neutrinos with the nucleon N. Different neutrino flavours are denoted by ν_l where l = e, μ, τ. Here X represents the final state hadrons.

In the above mentioned CC and NC interactions, different processes can take place depending on the energy of the neutrino and the type of target nucleon. These interaction processes are classified into three broad categories: quasi elastic (QE), resonant production (RES) and deep inelastic scattering (DIS). In the low energy regime ($E_\nu < 1$ GeV), QE interaction is the dominant process where neutrino scatters entire nucleon elastically producing single or multiple nucleons.

Category	CC	NC
QE	$\nu_l\ n \rightarrow l^-\ p$	$\nu_l\ p \rightarrow \nu_l\ p$; $\nu_l\ n \rightarrow \nu_l\ n$
	$\bar{\nu}_l\ p \rightarrow l^+\ n$	$\bar{\nu}_l\ p \rightarrow \bar{\nu}_l\ p$; $\bar{\nu}_l\ n \rightarrow \bar{\nu}_l\ n$
RES	$\nu_l\ p \rightarrow l^-\ p\ \pi^+$; $\nu_l\ n \rightarrow l^-\ n\ \pi^+$	$\nu_l\ p \rightarrow \nu_l\ n\ \pi^+$; $\nu_l\ n \rightarrow \nu_l\ p\ \pi^-$
	$\bar{\nu}_l\ p \rightarrow l^+\ p\ \pi^-$; $\bar{\nu}_l\ n \rightarrow l^+\ n\ \pi^-$	$\bar{\nu}_l\ p \rightarrow \bar{\nu}_l\ n\ \pi^+$; $\bar{\nu}_l\ n \rightarrow \bar{\nu}_l\ p\ \pi^-$
	$\nu_l\ n \rightarrow l^-\ p\ \pi^0$	$\nu_l\ p \rightarrow \nu_l\ p\ \pi^0$; $\nu_l\ n \rightarrow \nu_l\ n\ \pi^0$
	$\bar{\nu}_l\ p \rightarrow l^+\ n\ \pi^0$	$\bar{\nu}_l\ p \rightarrow \bar{\nu}_l\ p\ \pi^0$; $\bar{\nu}_l\ n \rightarrow \bar{\nu}_l\ n\ \pi^0$
DIS	$\nu_l\ N \rightarrow l^-\ X$	$\nu_l\ N \rightarrow \nu_l\ X$
	$\bar{\nu}_l\ N \rightarrow l^+\ X$	$\bar{\nu}_l\ N \rightarrow \bar{\nu}_l\ X$

Table 2.3: Types of CC and NC interactions of neutrinos with a nucleon N. Different neutrino flavours are denoted by ν_l where l = e, μ, τ. Here X represents the final state hadrons.

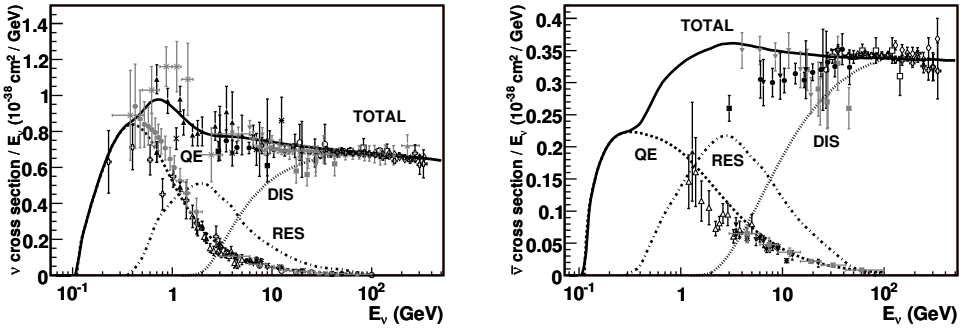

Figure 2.6: Neutrino (left) and anti-neutrino (right) CC interaction cross section with an iso-scalar singlet target [148].

For CC interaction this process is referred to as *quasi-elastic* scattering whereas the same is referred to as *elastic scattering* for NC interaction. In the resonance process neutrino can excite the target nucleon to a resonant baryonic state (Δ, N^*) which further decays to different types of mesons resulting mesons and nucleons in the final state. This type of resonant interaction becomes prominent in 1-2 GeV energy range. As the energy of the neutrino increases, it can directly interact with the quark constituent of the nucleon and produces hadronic shower comprising of

nucleons, mesons and other hadrons. After 2 GeV, DIS becomes the dominant interaction mechanism. All the interactions and their final states are summarized in Table 2.3 [148]. Total cross section along with individual contributions are shown in Figure 2.6 [148] for neutrinos and anti-neutrinos. This gives an idea to the experimentalist in which energy regime they are working on and the relevant processes that are going on to predict the number of events expected in an experiment.

INO experiment is tuned towards the GeV range so almost all the processes discussed earlier (QE, RES and DIS) will contribute towards the number of events. We know in the oscillation experiment NC events do not provide any additional information about flavour conversion and therefore we mostly focus on the CC interaction in the detector. In CC interaction both μ^- (μ^+) and e^- (e^+) will be produced from the interaction of ν_μ ($\bar{\nu}_\mu$) and ν_e ($\bar{\nu}_e$) interactions along with hadrons respectively. ICAL is designed to mainly look for the $\mu^\pm$ events in the detector as ICAL has very good energy ($\approx$ 10% for E_ν = 1 GeV) and angular resolution ($\approx 1^\circ$) [10]. ICAL can not distinguish electron events when produced by the ν_e and $\bar{\nu}_e$ interactions in the detector. This is mainly because of the shower properties of electrons at GeV energies and their subsequent absorption in the iron layers. Hadrons produced in the CC interactions also can not be separated individually. Muons being minimum ionizing particle (MIP) traverse a longer distance produces a track in the detector. Although the individual components of a hadron shower is not identifiable in the ICAL detector but their energies are estimated using the hit pattern in the active RPC detector [149, 150]. As muon produces cleaner track, the energy of the muon is measured from the bending of the muon track in the magnetic field by using Kalman filter [151]. The energy and direction measurements of the daughter particles in neutrino interaction is extremely important to estimate the parent neutrino energy.

Chapter 3

The hierarchy and octant sensitivity combining ESSνSB, T2K, NOνA and INO

3.1 Introduction

The paradigm of three flavour neutrino oscillation is well established now and most of the parameters have been measured with considerable precision. Efforts are going on to measure them more precisely and determine the unknown parameters. At the present epoch, the main challenges in the neutrino sector is to find out the correct mass hierarchy, octant of the oscillation parameter θ_{23} and the leptonic CP phase $\delta_{\rm CP}$. One of the main difficulties in determining these parameters are the presence of degeneracies [152–156] due to the unknown value of oscillation parameters which reduce the sensitivity of an experiment. Several future experiments are proposed or planned to address the above degeneracies and unambiguous determination of the parameters – hierarchy, octant and $\delta_{\rm CP}$. This includes the beam based experiments T2HK [11] / T2HKK [12], DUNE [13] and ESSνSB [14, 15]. Several studies have been performed in the literature to explore the physics potential of these facilities

[157–170]. A recent comparative study of these facilities have been accomplished in [171].

In this chapter the synergies between data from different experiments to address the degeneracies in the oscillation parameters are explored. In particular, combination of simulated data from atmospheric neutrino experiment INO along with long baseline experiments T2K , NOνA and ESSνSB have been studied. We focus on how the reach of the proposed experiment ESSνSB can be enhanced in conjunction with INO and the currently running accelerator experiments T2K and NOνA using the synergies that exist across different experiments. The ESSνSB proposal plans to use the European Spallation Source (ESS), which is under construction in Sweden [172]. The ESSνSB experiment will use this facility for generating very intense neutrino super beam. The main aim of the ESSνSB experiment is to measure the CP violation in the neutrino sector. This is expected to be achieved by using the second oscillation maximum of the $P_{\mu e}$ probability. However, the hierarchy and octant sensitivity at the second oscillation maximum gets compromised as compared to the first oscillation maximum. Optimization of the ESSνSB configuration with $\delta_{\rm CP}$ has been done in [15], which recommends the neutrino beam peak energy 0.2 GeV, 540 km baseline and 2 years ν + 8 years $\bar{\nu}$ run. In [173], the octant sensitivity of ESSνSB has been studied at both first and second oscillation maximum and they advocated 200 km baseline with 7ν+$3\bar{\nu}$ years as the optimal configuration for octant and CP sensitivity. In this study our aim is to explore whether the hierarchy and octant sensitivity of the ESSνSB setup as proposed in [15] can be improved by combining with the proposed atmospheric neutrino experiment INO. It has been shown earlier that since the hierarchy sensitivity of INO is independent of $\delta_{\rm CP}$, combination of INO with T2K and NOνA can help to raise the hierarchy sensitivity for unfavorable values of $\delta_{\rm CP}$ for the latter experiments [174]. We perform a quantitative analysis of this effect for the ESSνSB experiment. In addition we also explore how the information from the ongoing experiments T2K and NOνA

can further enhance the hierarchy and octant sensitivity of the ESSνSB + INO. We discuss in detail the various degeneracies and expound the synergistic effects of combining data from the various experiments.

This chapter (based on [22]) is structured as follows. In Section 3.2, we have described the appearance probabilities of the long-baseline accelerator experiments (LBL) and the associated degeneracies. We also discuss briefly the behavior of the probability for baselines and energies for which resonance matter effect occurs for atmospheric neutrinos passing through the Earth. Section 3.3, summarizes the various experiments that are used in this analysis and in Section 3.4 the details of the simulation procedure is described. The Section 3.5 contains the results for the mass hierarchy and octant sensitivity that can be achieved from ESSνSB , INO , T2K + NOνA and their various combinations. Conclusions are presented in Section 3.6.

3.2 Probability analysis

For the accelerator based experiments T2K, NOνA, ESSνSB the relevant channel for mass hierarchy and octant sensitivity is the appearance channel governed by the probability $P_{\mu e}$. In presence of matter of constant density, this can be expanded in terms of the small parameters α $(= \frac{\Delta m^2_{21}}{\Delta m^2_{31}})$ and $\sin\theta_{13}$ up to second order as [175]:

$$\begin{aligned} P(\nu_\mu \to \nu_e) \;=\; & \sin^2 2\theta_{13} \sin^2\theta_{23} \frac{\sin^2\Delta(1-\hat{A})}{(1-\hat{A})^2} \\ & + \alpha \cos\theta_{13} \sin 2\theta_{12} \sin 2\theta_{13} \sin 2\theta_{23} \cos(\Delta + \delta_{\rm CP}) \frac{\sin\Delta\hat{A}}{\hat{A}} \frac{\sin\Delta(1-\hat{A})}{(1-\hat{A})} \\ & + \alpha^2 \sin^2 2\theta_{12} \cos^2\theta_{13} \cos^2\theta_{23} \frac{\sin^2\Delta\hat{A}}{\hat{A}^2} \end{aligned} \tag{3.1}$$

where, E = energy of the neutrino, $A = 2\sqrt{2}G_F N_e E$, G_F is the Fermi constant, N_e is the number density of electrons in matter, L is the baseline, $\Delta = \frac{\Delta m^2_{31} L}{4E}$,

$\alpha = \frac{\Delta m^2_{21}}{\Delta m^2_{31}}$, $\hat{A} = \frac{A}{\Delta m^2_{31}}$, $\Delta m^2_{ij} = m^2_i - m^2_j$.

In Figure 3.1 we have plotted the appearance probabilities for T2K baseline of 295 km (top row) and NOνA baseline of 810 km (bottom row) as a function of $\delta_{\rm CP}$. The energies are fixed at the peak energies of 0.6 GeV and 2 GeV respectively in these plots. The left and right columns represent the neutrino and anti-neutrino oscillation probabilities respectively. Each plot in Figure 3.1 and Figure 3.2 comprises of four different hierarchy-octant bands NH-LO (cyan), NH-HO (purple), IH-LO (green), IH-HO (brown). Each LO (HO) band represents the θ_{23} variation in the range $39^\circ - 42^\circ$ ($48^\circ - 51^\circ$). These plots help to understand the various degeneracies occurring between hierarchy, octant and $\delta_{\rm CP}$.

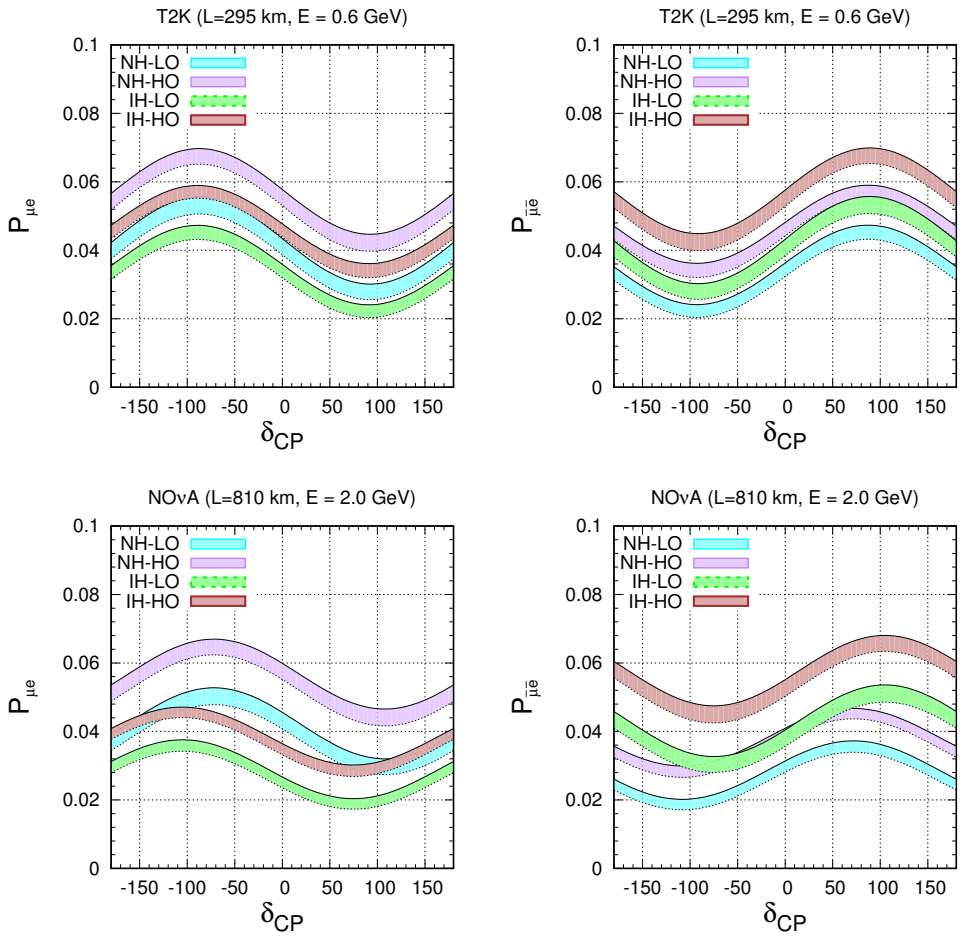

Figure 3.1: Probability vs $\delta_{\rm CP}$ for T2K & NOνA. The bands are obtained by varying θ_{23} in lower octant and upper octant. See text for details.

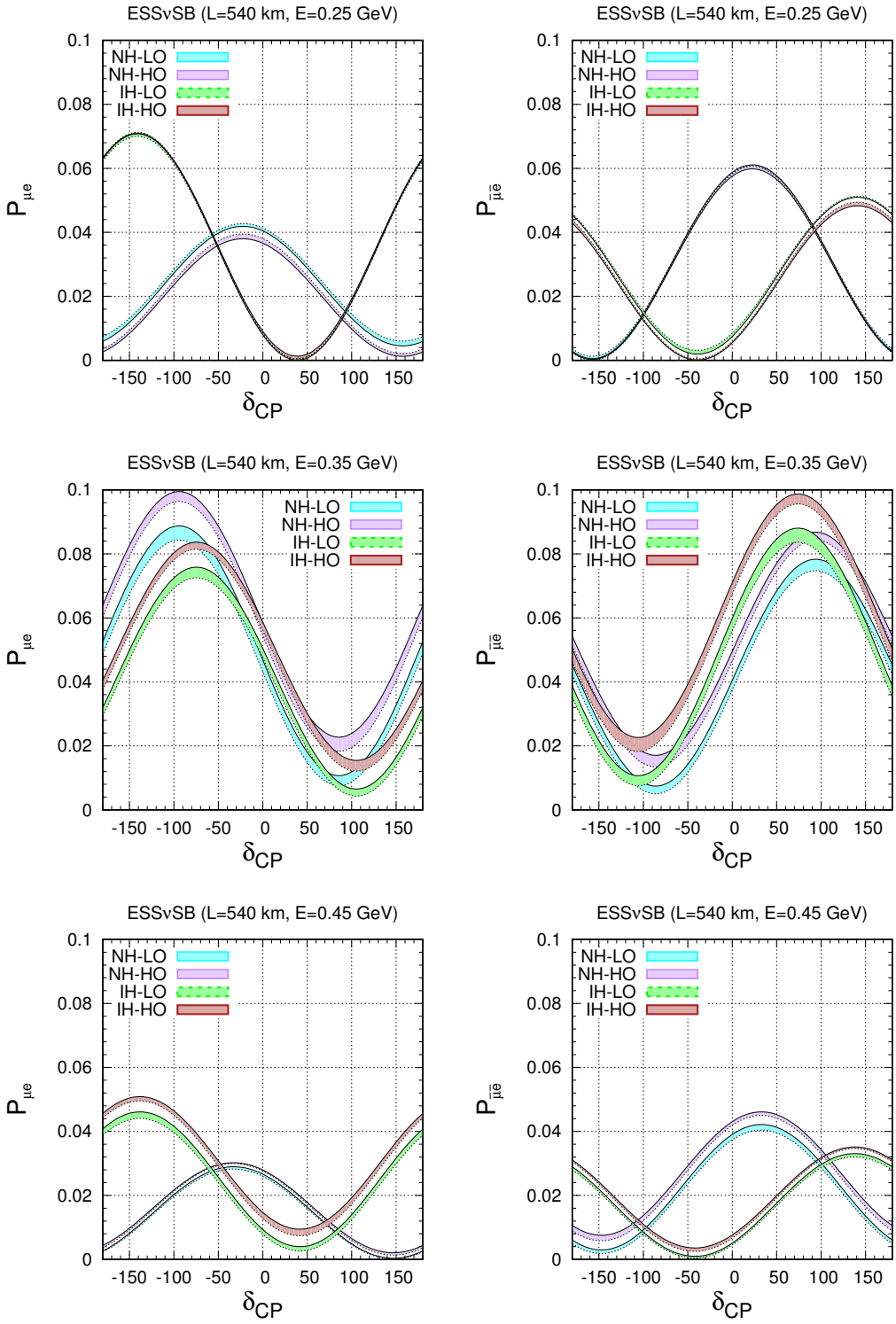

Figure 3.2: Appearance probability for ESSνSB for different energies. The bands are obtained by varying θ_{23} in lower octant and upper octant. See text for details.

With respect to $\delta_{\rm CP}$ there can be two kind of solutions : (i) those with wrong values of $\delta_{\rm CP}$ which can be seen by drawing a horizontal line through the curves and seeing the CP values at which this line intersects the two bands of opposite hierarchies and/or octant. (ii) Those with right values of $\delta_{\rm CP}$ which occur when two bands intersect each other. Thus we can have the following type of degenerate solutions in addition to the true solution which can affect the hierarchy and octant sensitivity [1] :

- Wrong Hierarchy - Right Octant - Right $\delta_{\rm CP}$ (WH-RO-R$\delta_{\rm CP}$)
- Wrong Hierarchy - Right Octant - Wrong $\delta_{\rm CP}$ (WH-RO-W$\delta_{\rm CP}$)
- Wrong Hierarchy - Wrong Octant - Right $\delta_{\rm CP}$ (WH-WO-R$\delta_{\rm CP}$)
- Wrong Hierarchy - Wrong Octant - Wrong $\delta_{\rm CP}$ (WH-WO-W$\delta_{\rm CP}$)
- Right Hierarchy - Wrong Octant - Wrong $\delta_{\rm CP}$ (RH-WO-W$\delta_{\rm CP}$)

The plots in Figure 3.1 show that there are no degeneracies at the highest and lowest points of the probability bands. These correspond to NH-HO (NH-LO) and $\delta_{\rm CP} \sim -90°$ and IH-LO (IH-HO) and $\delta_{\rm CP} \sim +90°$ for neutrinos (anti-neutrinos). The rest of the combinations are not free from hierarchy - octant - $\delta_{\rm CP}$ degeneracies [155]. NOνA baseline being higher, shows a wider separation between opposite hierarchies than that of T2K. Also one can note that combination of neutrinos and anti-neutrinos can remove octant degeneracy. For instance NH-LO with $\delta_{\rm CP} \sim -90°$ is degenerate with IH-HO with $\delta_{\rm CP}$ in the same half plane and NH-HO in the opposite half plane of $\delta_{\rm CP}$ as can be seen by comparing the cyan, brown and purple bands for the neutrinos. Thus with neutrinos one can get degenerate

[1] Note that Right Hierarchy-Right Octant-Wrong $\delta_{\rm CP}$ degeneracy is not a degeneracy for mass hierarchy and octant sensitivities and therefore it was not mentioned. Also, Right Hierarchy-Wrong Octant-Right $\delta_{\rm CP}$ is not really a degeneracy, this can be understood by drawing a vertical line at a particular $\delta_{\rm CP}$ in the $P_{\mu e}$ vs $\delta_{\rm CP}$ plot. Here we observe that the values of $P_{\mu e}$ will always be different for the opposite octants. If at all a solution encompassing LO and HO appears that will be due to the limitation in the measurement of θ_{23}.

solutions corresponding to WH-WO-R$\delta_{\rm CP}$ and RH-WO-W$\delta_{\rm CP}$. However, if one considers anti-neutrinos then these degeneracies are not present. Thus combination of neutrino and anti-neutrino data can help in alleviating degenerate solutions in opposite octant [25–27, 155, 176].

The ESSνSB set-up that we consider corresponds to that discussed in [15] with a baseline of 540 km – between Lund and Garpenberg mine. The flux peaks around 0.24 GeV with significant flux around 0.35 GeV which is close to the second oscillation maximum. The probability has a sharper variation at the second oscillation maximum, with $\delta_{\rm CP}$ leading to a higher CP sensitivity. Primarily three energy bins with mean energy 0.25 GeV (E1), 0.35 GeV (E2), 0.45 GeV (E3) contribute significantly to the hierarchy sensitivity. Thus, in order to understand the degeneracies for the ESSνSB baseline of 540 km we have plotted the appearance probability for three different energies in Figure 3.2 where the top, middle and bottom row corresponds to 0.25 GeV, 0.35 GeV and 0.45 GeV respectively. The behavior of $P_{\mu e}$ for 0.35 GeV is somewhat similar to that of T2K and NOνA in Figure 3.1. However, the variation with $\delta_{\rm CP}$ is sharper, octant bands are narrower and the different curves intersect each other more number of times indicating presence of wrong hierarchy and/or wrong octant solutions at right $\delta_{\rm CP}$. There is no degeneracy for NH-HO (NH-LO) at $\delta_{\rm CP} = -90^\circ$ and IH-LO (IH-HO) at $\delta_{\rm CP} = +90^\circ$ for neutrinos(anti-neutrinos) as in case of T2K and NOνA. The degeneracies for the energies 0.25 and 0.45 GeV are different than the above. From top left and bottom left plots in Figure 3.2, we find that for neutrinos, IH does not suffer from mass hierarchy degeneracy in ($-180^\circ \leq \delta_{\rm CP} \leq -60^\circ$ and $130^\circ \leq \delta_{\rm CP} \leq 180^\circ$) but NH suffers from hierarchy degeneracy for the whole range of $\delta_{\rm CP}$. For anti-neutrinos (top and bottom right panel in Figure 3.2) for $-30^\circ \geq \delta_{\rm CP} \geq 70^\circ$ there is no degeneracy for NH while IH is degenerate with NH throughout the full range of $\delta_{\rm CP}$. Thus the degeneracies for NH and IH occur for different $\delta_{\rm CP}$ values and combination of neutrino and anti-neutrino runs can help in resolving these.

The dependence of $P_{\mu e}$ on $\delta_{\rm CP}$ and θ_{23} can be understood analytically by expressing the probability $P_{\mu e}$ as follows [25]:

$$P_{\mu e} = (\beta_1 - \beta_3)\sin^2\theta_{23} + \beta_2 \sin 2\theta_{23}\cos(\Delta + \delta_{\rm CP}) + \beta_3 \tag{3.2}$$

where,

$$\begin{aligned}
\beta_1 &= \sin^2 2\theta_{13}\frac{\sin^2\Delta(1-\hat{A})}{(1-\hat{A})^2}, \\
\beta_2 &= \alpha\cos\theta_{13}\sin 2\theta_{12}\sin 2\theta_{13}\frac{\sin\Delta\hat{A}}{\hat{A}}\frac{\sin\Delta(1-\hat{A})}{1-\hat{A}}, \\
\beta_3 &= \alpha^2\sin^2 2\theta_{12}\cos^2\theta_{13}\frac{\sin^2\Delta\hat{A}}{\hat{A}^2}
\end{aligned} \tag{3.3}$$

The CP dependence of the probabilities can be understood from the following expression

$$P_{\mu e}(\delta_{\rm CP}) - P_{\mu e}(\delta'_{\rm CP}) = -2\beta_2\sin^2 2\theta_{23}\sin\left(\Delta + \frac{\delta_{\rm CP}+\delta'_{\rm CP}}{2}\right)\sin\left(\frac{\delta_{\rm CP}-\delta'_{\rm CP}}{2}\right) \tag{3.4}$$

for neutrino probabilities and normal hierarchy. T2K and NOνA are experiments close to first oscillations maximum corresponding to $\Delta \approx \frac{\pi}{2}$. Then, Equation 3.4 reduces to

$$P_{\mu e}(\delta_{\rm CP}) - P_{\mu e}(\delta'_{\rm CP}) = -2\beta_2\sin^2 2\theta_{23}\cos\left(\frac{\delta_{\rm CP}+\delta'_{\rm CP}}{2}\right)\sin\left(\frac{\delta_{\rm CP}-\delta'_{\rm CP}}{2}\right) \tag{3.5}$$

For ESSνSB as the bin 0.35 GeV is close to the second oscillations maximum, we can write $\Delta \approx \frac{3\pi}{2}$. Hence, the Equation 3.4 is,

$$P_{\mu e}(\delta_{\rm CP}) - P_{\mu e}(\delta'_{\rm CP}) = 2\beta_2\sin^2 2\theta_{23}\cos\left(\frac{\delta_{\rm CP}+\delta'_{\rm CP}}{2}\right)\sin\left(\frac{\delta_{\rm CP}-\delta'_{\rm CP}}{2}\right) \tag{3.6}$$

The 0.25 GeV bin in ESSνSB is closer to the third oscillations maximum, so $\Delta \approx \frac{5\pi}{2}$. Hence, the governing equation for this energy is the Equation 3.5. Although

Equation 3.5 and Equation 3.6 have a relative $(-)$ sign, the shapes are similar for Figure 3.1 and the second row for Figure 3.2 because the $\beta_2 = 0.013$ for T2K, $\beta_2 = 0.011$ for NOνA and $\beta_2 = -0.039$ for ESSνSB . Thus the negative sign in β_2 compensates for the relative negative signs between the two equations. The sharper variation in the probabilities for ESSνSB can be attributed to the higher $|\beta_2|$ value of ESSνSB as compared to T2K and NOνA ($|\beta_2|_{\text{ESS}\nu\text{SB}} \approx 3|\beta_2|_{\text{T2K(NO}\nu\text{A)}}$). To understand the shape of the $P_{\mu e}$ curve the slopes of the probability for various δ_{CP} values should be understood, which is given by

$$S = \frac{dP_{\mu e}}{d\delta_{\text{CP}}} = -\beta_2 \sin^2 2\theta_{23} \sin(\Delta + \delta_{\text{CP}}) \tag{3.7}$$

From Equation 3.7 we obtain that in Figure 3.1 the slope is positive from $-180° < \delta_{\text{CP}} < -90°$ and $90° < \delta_{\text{CP}} < 180°$, with the slope becoming zero at $\delta_{\text{CP}} = -90°$ and $90°$ and positive from $-90° < \delta_{\text{CP}} < 90°$. The same explanation is also valid for 0.35 GeV probability for ESSνSB but the slopes being higher in ESSνSB due to greater $|\beta_2|$. Comparing the NH-LO(blue) and NH-HO(purple) bands Figure 3.2 and Figure 3.1 we can see that the variation of NH probabilities for ESSνSB 0.25 GeV is more rapid compared to T2K and NOνA but less rapid compared to 0.35 GeV of ESSνSB. This is because the $|\beta_2|$ for 0.25 GeV bin in ESSνSB is greater compared to T2K and NOνA and less in comparison with 0.35 GeV bin of ESSνSB. Similarly, the shapes for IH and the anti-neutrino probabilities can be explained.

Baseline(L)	Peak Energy(E)	β_1		β_2		β_3	
		NH	IH	NH	IH	NH	IH
295 km	0.6 GeV	0.094	0.077	0.013	-0.011	0.002	0.002
810 km	2.0 GeV	0.095	0.062	0.011	-0.009	0.001	0.001
540 km	0.25 GeV	0.015	0.035	0.023	-0.035	0.034	0.034
540 km	0.35 GeV	0.090	0.071	-0.039	0.035	0.017	0.017

Table 3.1: β_1, β_2 & β_3 values in Equation 3.3 for 295 km, 810 km, and 540 km baselines corresponding to T2K, NOνA and ESSνSB experiments.The energies correspond to the values where the flux peaks. For ESSνSB we present the values for two representative energies.

The dependence of $P_{\mu e}$ on θ_{23} can also be understood from Equation 3.2, 3.3 and Table 3.1. In case of ESSνSB one can see from the plots in Figure 3.2 that the octant bands for 0.25 GeV and 0.45 GeV are very narrow indicating that the probabilities do not change significantly with θ_{23}. For the energy bin 0.35 GeV the octant bands are slightly wider as compared to the other two energies. The θ_{23} behavior is governed by the first term of Equation 3.2, which shows a linear variation with θ_{23} with a slope of $(\beta_1 - \beta_3)$. Over the allowed range of θ_{23} $(39° - 51°)$, $\sin 2\theta_{23} \sim 1$ and hence the second term of Equation 3.2 does not play a role in determining the dependence of $P_{\mu e}$ on θ_{23}.

$$P_{\mu e}(\theta_{23}) - P_{\mu e}(\theta'_{23}) \approx (\beta_1 - \beta_3)(\sin^2\theta_{23} - \sin^2\theta'_{23}) \tag{3.8}$$

This does not depend on $\delta_{\rm CP}$ which is corroborated by the probability plots. The β_is for the three different baselines and the relevant energies are tabulated in Table 3.1 for both the hierarchies. We can see that for the ESSνSB baseline and 0.25 GeV energy the β_1 and β_3 are almost equal indicative of the fact that the probability does not vary much with θ_{23}. For 0.35 GeV energy $\beta_1 - \beta_3 \sim 0.73$ for NH and 0.54 for IH, hence the octant bands are comparatively wider. This also implies that the IH bands are slightly narrower as compared to the NH bands as can be seen from the figure. For 0.25 GeV and 0.45 GeV the octant degeneracy for the same hierarchy is seen to prevail over the full range of $\delta_{\rm CP}$ corresponding to RH-WO-R$\delta_{\rm CP}$ solutions. In addition RH-WO-W$\delta_{\rm CP}$, WH-WO-W$\delta_{\rm CP}$, WH-RO-W$\delta_{\rm CP}$ and WH-WO-R$\delta_{\rm CP}$ solutions are also seen to be present. The octant sensitivity of ESSνSB comes mainly from the bin with mean energy the 0.35 GeV. For this energy, the octant degeneracies are seen to occur close to $\pm 90°$ in the same half plane giving WH-WO-R$\delta_{\rm CP}$ between NH-LO(cyan band) and IH-HO(brown band) for neutrinos and between NH-HO(purple band) and IH-LO(green band) for anti-neutrinos. For purposes of comparison we also give the β_i values for T2K and

NOνA. For these cases also the NH bands are slightly wider than the IH bands as can be seen from the Figure 3.2 and the values of $(\beta_1 - \beta_3)$.

In comparison to the LBL experiments the atmospheric neutrinos in ICAL detector can travel through larger baselines and encounter resonance effects. At resonance, the probabilities can be better described by the one mass scale dominance (OMSD) approximation rather than the $\alpha - s_{13}$ approximation in Equation 3.1. The relevant probabilities $P_{\mu\mu}$ and $P_{\mu e}$ in the OMSD approximation can be expressed as,

$$\mathrm{P}^{\mathrm{m}}_{\mu\mathrm{e}} = \sin^2\theta_{23}\ \sin^2 2\theta^{\mathrm{m}}_{13}\ \sin^2\left[1.27\ (\Delta\mathrm{m}^2_{31})^{\mathrm{m}}\ \frac{\mathrm{L}}{\mathrm{E}}\right] \tag{3.9}$$

$$\begin{aligned}
\mathrm{P}^{\mathrm{m}}_{\mu\mu} \;=\;& 1 - \cos^2\theta^{\mathrm{m}}_{13}\sin^2 2\theta_{23}\ \sin^2\left[1.27\ \left(\frac{\Delta\mathrm{m}^2_{31} + \mathrm{A} + (\Delta\mathrm{m}^2_{31})^{\mathrm{m}}}{2}\right)\ \frac{\mathrm{L}}{\mathrm{E}}\right] \\
&- \sin^2\theta^{\mathrm{m}}_{13}\sin^2 2\theta_{23}\ \sin^2\left[1.27\ \left(\frac{\Delta\mathrm{m}^2_{31} + \mathrm{A} - (\Delta\mathrm{m}^2_{31})^{\mathrm{m}}}{2}\right)\ \frac{\mathrm{L}}{\mathrm{E}}\right] \\
&- \sin^4\theta_{23}\sin^2 2\theta^{\mathrm{m}}_{13}\ \sin^2\left[1.27\ (\Delta\mathrm{m}^2_{31})^{\mathrm{m}}\ \frac{L}{E}\right]
\end{aligned} \tag{3.10}$$

Due to matter effect the modified mass squared difference $(\Delta\mathrm{m}^2_{31})^{\mathrm{m}}$ and mixing angle $\sin^2 2\theta^{\mathrm{m}}_{13}$ are given by ,

$$\begin{aligned}
(\Delta\mathrm{m}^2_{31})^{\mathrm{m}} &= \sqrt{(\Delta\mathrm{m}^2_{31}\cos 2\theta_{13} - \mathrm{A})^2 + (\Delta\mathrm{m}^2_{31}\sin 2\theta_{13})^2} \\
\sin 2\theta^{\mathrm{m}}_{13} &= \frac{\Delta\mathrm{m}^2_{31}\sin 2\theta_{13}}{\sqrt{(\Delta\mathrm{m}^2_{31}\cos 2\theta_{13} - \mathrm{A})^2 + (\Delta\mathrm{m}^2_{31}\sin 2\theta_{13})^2}}
\end{aligned} \tag{3.11}$$

The Mikheyev-Smirnov-Wolfenstein(MSW) matter resonance [177–179] occurs when,

$$\Delta\mathrm{m}^2_{31}\cos 2\theta_{13} = A$$

The MSW resonance happens when $\Delta\mathrm{m}^2_{31} > 0$ for neutrinos and $\Delta\mathrm{m}^2_{31} < 0$ for anti-neutrinos. Sine the resonance conditions are opposite for neutrinos and anti-

neutrinos therefore the ability to distinguish between neutrinos and anti-neutrinos is crucial for mass hierarchy sensitivity. Hence, the ICAL detector which has charge sensitivity can help unfold the mass hierarchy. The $\sin^2\theta_{23}$ term in $P_{\mu e}$ and $\sin^4\theta_{23}$ term in $P_{\mu\mu}$ is responsible for the octant sensitivity of ICAL [180]. Detailed discussion on the octant dependence of the probability for atmospheric neutrinos can be found for instance in [181].

3.3 Experimental details

In this section we provide a brief description of the experiments used in our study — the currently running long-baseline experiments T2K, NOνA and also the future proposed long-baseline experiment ESSνSB along with the atmospheric neutrino experiment ICAL@INO.

T2K (Tokai to Kamioka) [16] is a 295 km baseline experiment with the flux centered at the neutrino energy around 0.6 GeV generated by JPARC neutrino beam facility at power level higher than 300 kW. T2K has already collected 3.1×10^{21} protons on target(POT) and is expected to collect a total of 8×10^{21} in 10 years. So, we have used a total POT of 8×10^{21} in our simulation. In order to minimize the experimental uncertainty a near and a far detector are used at an angle 2.5° from the center of the neutrino beam. Using the shape of the Ĉherencov rings, the Super Kamiokande detector (fiducial volume 22.5 kt) for T2K has the ability to distinguish between electron and muon events. In our analysis we have considered 4 years of neutrino and 4 years of anti-neutrino runs for T2K.

NOνA experiment [17] is also a long-baseline neutrino experiment with a baseline of 810 km between the source and the detector. NOνA uses high intensity 400 kW NuMI beam at Fermi lab. In this experimental set up a relatively smaller, 222 ton near detector and a bigger 15 kiloton far detector are placed at an off axis of 0.8° from the NuMI beam with peak energy at 2 GeV. In both near and far

positions liquid scintillator type detectors are used. NOνA is currently running at 700 kW beam power corresponding to 7.3×10^{20} POT yearly and has already collected 8.85×10^{20} POT. NOνA is planned to run in 3 years neutrino and 3 years of anti-neutrino mode. In our study we have used the re-optimized NOνA set up from [18, 19] and have used the full projected run time.

ESSνSB [14, 15] is a 540 km baseline experiment where high intensity neutrino beam will be produced at the European Spallation Source (ESS) in Lund, Sweden. ESSνSB [172] will focus its research on the second oscillation maximum and plans to use a megaton water Ĉherencov detector. To create a high intensity neutrino beam, they propose to use the linac facility of the European Spallation Source which will produce 2 GeV protons with an average beam power of 5 MW and 27×10^{23} POT. The ESSνSB collaboration advocates an optimized set up with 2 years of neutrino and 8 years of anti-neutrino runs [182].

India-based **N**eutrino **O**bservatory (INO) [125] is a proposal for observing atmospheric neutrinos in a magnetized **i**ron **cal**orimeter (ICAL) detector. This experiment will look for atmospheric ν_μ and $\bar{\nu}_\mu$ in the GeV energy range. It is proposed to be built in the southern part of India under a mountain with 1 km overall rock coverage. It will house a 50 kt ICAL detector with 1.5 Tesla magnetic field. Because of the magnetic properties of the detector, ICAL can identify the polarity of the charged particles produced by the **c**harge **c**urrent (CC) interaction of neutrinos with the detector. This gives it the ability to differentiate between neutrinos and anti-neutrinos by identifying the charge of the daughter particles using Resistive Plate Chambers (RPC) as an active detector component.

3.4 Simulation details

In this section we present the details of our simulation procedure for the LBL experiments T2K, NOνA and ESSνSB and the atmospheric neutrino experiment

ICAL@INO. We also discuss how the combined analysis of the various experiments are performed.

The simulation for the long-baseline accelerator experiments T2K , NOνA & ESSνSB are done using the General Long Baseline Experiment Simulator (GLoBES) package [20, 21]. In this, the capability of an experiment to determine an oscillation parameter is obtained by a χ^2-analysis using frequentist approach. The total $\chi^2_{\rm tot}$ is composed of $\chi^2_{\rm stat}$ and $\chi^2_{\rm pull}$ and is given by the following relation

$$\chi^2_{\rm tot} = \min_{\xi,\Omega} \left\{ \chi^2_{\rm stat}(\Omega, \xi) + \chi^2_{\rm pull}(\xi) \right\} \tag{3.12}$$

where $\Omega = \{\theta_{12}, \theta_{13}, \theta_{23}, \Delta m^2_{21}, \Delta m^2_{31}, \delta_{\rm CP}\}$ represents the oscillation parameters, $\chi^2_{\rm stat}$ denotes the Poissonian χ^2 function and $\chi^2_{\rm pull}$ consists of the systematic uncertainties incorporated in terms of pull variables (ξ). The "pull" variables considered in our analysis are signal normalization error, background normalization error, energy calibration error on signal & background (tilt). In the "pull" method a penalty term is added in terms of the "pull" variables which is given by $\chi^2_{\rm pulls} = \sum_{r=1}^{r=4} \xi_r^2$ in order to account for the systematics errors stated above. The Poissonian $\chi^2_{\rm stat}$ is given by

$$\chi^2_{\rm stat}(\Omega, \xi) = 2 \sum_i \left\{ \tilde{N_i}^{\rm test} - N_i^{\rm true} + N_i^{\rm true} \ln \frac{N_i^{\rm true}}{\tilde{N_i}^{\rm test}} \right\}. \tag{3.13}$$

The number of events predicted by the theoretical model over a range of oscillation parameters Ω in the i^{th} bin and is given by

$$\tilde{N_i}^{\rm test}(\Omega, \xi) = \sum_{k=s,b} {N_i}^k(\Omega) \left[1 + c_i^{(k)norm} \xi^{(k)norm} + c_i^{(k)tilt} \xi^{(k)tilt} \frac{E_i - \bar{E}}{E_{max} - E_{min}} \right] \tag{3.14}$$

where, $k = s(b)$ denotes signal(background) and $c_i^{norm}({c_i}^{tilt})$ represents alteration in the number of events by the modification of the "pull" variable $\xi^{norm}(\xi^{tilt})$. E_i is the mean reconstructed energy of the i^{th} bin, and $\bar{E} = (E_{max} + E_{min})/2$ is the

mean energy over this range with E_{min} and E_{max} denoting the maximum and minimum energy. The systematic errors on the signal and background normalizations are shown in Table 3.2 [2]. N_i^{true} in Equation 3.13 is given by the sum of simulated signal and background events $N_i^{\text{true}} = N_i^s + N_i^b$.

The background channels influencing detection of neutrinos is dependent on the type of detector used. The background channels which contribute for the water Ĉherenkov detectors for T2K and ESSνSB are the Charged Current(CC) non-Quasielastic(QE) background, intrinsic beam background, neutral current background and mis-identification error. While the main background channels affecting the scintillator detector in NOνA are CC non-QE, intrinsic beam background, neutral current background. The systematic uncertainties in signal and background normalizations in various channels are summarized in Table 3.2. Besides these, the energy calibration errors are also incorporated in the analysis in terms of "tilt" errors. The signal (background) "tilt" errors that have been included are 1%(5%) for T2K, 0.1%(0.1%) for NOνA and 0.1%(0.1%) for ESSνSB .

Channel	T2K	NOνA	ESSνSB
ν_e appearance	2% (5%)	5% (10%)	5% (10%)
$\bar{\nu}_e$ appearance	2% (5%)	5% (10%)	5% (10%)
ν_μ disappearance	0.1% (0.1%)	2.5% (10%)	5% (10%)
$\bar{\nu}_\mu$ disappearance	0.1% (0.1%)	2.5% (10%)	5% (10%)

Table 3.2: The signal (background) normalization errors for T2K , NOνA and ESSνSB .

ICAL is a 50 kt detector which aims to detect ν_μ and $\bar{\nu}_\mu$ along with hadron produced in the detector. Atmospheric flux consist of ν_μ ($\bar{\nu}_\mu$) and $\nu_e(\bar{\nu}_e)$ both of which will contribute to the number of events observed in the ICAL detector. The

[2]Note that, we have used statistical errors as dominant for ν_μ and $\bar{\nu_\mu}$ in case of T2K[183]. Therefore, the errors for the disappearance channels are kept small.

events observed in the detector can be expressed as:

$$\frac{d^2N}{d\Psi_\mu} = (t\ n_d) \times \int d\Psi_\nu\ d\Phi_\mu \left[P_{\mu\mu} \frac{d^3\Phi_\mu}{d\Psi_\nu\ d\Phi_\nu} + P_{e\mu} \frac{d^3\Phi_e}{d\Psi_\nu\ d\Phi_\nu} \right] \frac{d\sigma_\mu(E_\nu)}{d\Psi_\mu} \tag{3.15}$$

where, $d\Psi_\alpha = dE_\alpha\ d\cos\theta_\alpha$, n_d is the number of nucleon target in the detector, t is the experiment run time, Φ_μ and Φ_e are the initial flux of muon and electron respectively, σ_μ is the differential neutrino interaction cross section. $P_{\mu\mu}$ and $P_{e\mu}$ are the muon survival and appearance probabilities. To reduce the Monte Carlo fluctuations, firstly 1000 years of unoscillated data is generated with Nuance [184] neutrino generator using Honda neutrino flux and the interaction cross section and the ICAL detector geometry. Each event is then multiplied with the oscillation probability depending on the neutrino energy and path length. Oscillation probability in matter is calculated solving differential neutrino propagation equation in matter using the PREM model for the density profile of the Earth [185]. These events are smeared on a bin by bin basis using detector resolutions and efficiencies [10, 149] to get realistic simulation of the ICAL detector. Later in our analysis we have scaled down to 10 years of ICAL data. For ICAL@INO both "data" and theory events are simulated in the same way. In our analysis, we have used the resolution and the efficiency obtained for the central part of the ICAL detector [10] using GEANT4 [186–188] based simulation for the whole detector. The typical muon energy resolution in the GeV energy range is $\sim 10\%$ and angular resolution is $\sim 1^\circ$ and charge identification efficiency is greater than $\sim 95\%$ in the relevant energy range[189]. As ICAL has very good energy and angular resolution for the muons produced in the detector, so the events spectrum is categorized in terms of measured muon energy (E_μ) and reconstructed muon angle ($\cos\theta_\mu$). This binning scheme is referred to as **2D** binning scheme in our analysis. Hadrons are also produced along with muons in the CC interaction with the detector. The hadron resolution is $\sim 85\%$ at 1 GeV and $\sim 36\%$ at 15 GeV. It is also possible to extract

the hadron energy in event by event basis in CC interaction as $E'_h = E_\nu - E_\mu$. Now the inelasticity parameter $y = \frac{E'_h}{E_\nu}$ can be used as an independent parameter with every CC event in the previously mentioned 2D scheme. Analysis with these three independent parameters is referred to as the **3D** binning scheme. Improvement of the sensitivities while using the 3D binning scheme over the 2D scheme has been shown in [190]. The binning scheme is summarized in Table 3.3. While generating the data, oscillation parameters are used at their true values whereas the test events are generated using the 3σ range as mentioned in the Table 3.4.

Reconstructed variable	[Range] (bin width)	Total bins
E_μ^{obs} (GeV)	[1 : 4] (0.5)	6
	[4 : 7] (1)	3
	[7 : 11] (4)	1
$\cos\theta_\mu$	[-1.0 : -0.4] (0.05)	12
	[-0.4 : 0] (0.1)	4
	[0.0 : 1.0] (0.2)	5
$E'_{\rm had}$ (GeV)	[0.0 : 2.0] (1)	2
	[2.0 : 4.0] (2)	1
	[4.0 : 11.0] (7)	1

Table 3.3: The binning scheme used in 2D (E_μ, $\cos\theta_\mu$) and 3D (E_μ, $\cos\theta_\mu$, $E'_{\rm had}$) analysis.

As ICAL is not sensitive to $\delta_{\rm CP}$ [191], we have not marginalized over test $\delta_{\rm CP}$ and fixed the value at 0° while generating the test events. To get the ICAL@INO sensitivity we perform a χ^2 analysis where with χ^2 defined as:

$$\chi^2_{\rm INO} = \min_{\xi_l^{\pm}} \sum_{i=1}^{N_{E_\mu^{obs}}} \sum_{j=1}^{N_{\cos\theta_\mu^{obs}}} \sum_{k=1}^{N_{E'^{obs}_{had}}} 2\left[\left(T^+_{ijk} - D^+_{ijk}\right) - D^+_{ijk}\ln\left(\frac{T^+_{ijk}}{D^+_{ijk}}\right)\right] + 2\left[\left(T^-_{ijk} - D^-_{ijk}\right) - D^-_{ijk}\ln\left(\frac{T^-_{ijk}}{D^-_{ijk}}\right)\right] + \sum_{l^+=1}^{5}\xi^2_{l^+} + \sum_{l^-=1}^{5}\xi^2_{l^-} \ . \quad (3.16)$$

Where i, j, k sums over muon energy, muon angle and hadron energy bins respectively. T_{ijk}, $D_{i,j,k}$ refers the predicted (theory) and observed (data) events respectively in i, j, k bin. The $\pm$ sign in theory or observed events refer to the $\mu^{\pm}$ events coming from $\nu_\mu^{\pm}$ interactions in the detector. The number of expected events with systematic errors in each bin are given by:

$$T^+_{ijk} = T^{0+}_{ijk}\left(1 + \sum_{l^+=1}^{5}\pi^{l^+}_{ijk}\xi_{l^+}\right) \ ; \ T^-_{ijk} = T^{0-}_{ijk}\left(1 + \sum_{l^-=1}^{5}\pi^{l^-}_{ijk}\xi_{l^-}\right) \ . \quad (3.17)$$

where $T^{0\pm}_{ijk}$ refers to the number of theory events without systematic errors in a particular bin i, j, k. The systematic uncertainties considered in the analysis using pull method are [192]:

- $\pi_1 = 20\%$ flux normalization error
- $\pi_2 = 10\%$ cross section error
- $\pi_3 = 5\%$ tilt error
- $\pi_4 = 5\%$ zenith angle error
- $\pi_5 = 5\%$ overall systematics

To incorporate the "tilt" error, the predicted neutrino fluxes is modified using:

$$\Phi_\delta(E) = \Phi_0(E)\left(\frac{E}{E_0}\right)^{\delta} \simeq \Phi_0(E)\left(1 + \delta\ln\frac{E}{E_0}\right), \quad (3.18)$$

where, E_0 is 2 GeV, and δ is the 1σ systematic "tilt" error (5%). Flux uncertainty is included as $\Phi_\delta(E) - \Phi_0(E)$.

Oscillation parameters	True value	Test range
$\sin^2 2\theta_{13}$	0.085	fixed
$\sin^2 \theta_{12}$	0.304	fixed
θ_{23}	42° (LO), 48° (HO)	39° : 51°
Δm^2_{21} (eV^2)	7.4×10^{-5}	fixed
Δm^2_{31} (eV^2)	2.5×10^{-3}	$(2.35 : 2.65) \times 10^{-3}$
$\delta_{\rm CP}$ (LBL)	$-180° : 180°$	$-180° : 180°$
$\delta_{\rm CP}$ (INO)	$-180° : 180°$	0°(fixed)

Table 3.4: The true and test values of the oscillation parameters used in our analysis.

For performing the statistical analysis the observed events or data are generated using the true values listed in Table 3.4. The predicted or test events are simulated varying the parameters $|\Delta m^2_{31}|$, $\sin^2\theta_{23}$ in their 3σ ranges presented in Table 3.4. The values of θ_{12}, $\sin^2\theta_{13}$ and Δm^2_{21} are held fixed to their best-fit values while calculating the test events. For LBL experiments $\delta_{\rm CP}$ is varied over $0° - 360°$ while generating the test events. For calculating χ^2 corresponding to hierarchy or octant sensitivity for a particular experiment marginalization is done over the oscillation parameters which are varied. If two or more LBL experiments are combined then the χ^2 of each experiment are added in the test plane and then the combined χ^2 is marginalized over. Since ICAL@INO is insensitive to $\delta_{\rm CP}$, the $\delta_{\rm CP}$(test) is kept fixed for ICAL@INO analysis to save computation time. While calculating the combined χ^2 for LBL and ICAL@INO, the marginalization over test-$\delta_{\rm CP}$ is first performed for LBL experiments and then the marginalized χ^2 is added with the ICAL@INO χ^2. This χ^2 is further marginalized over the oscillation parameters

$|\Delta m^2_{31}|$, $\sin^2\theta_{23}$ as follows :

$$\chi^2_{tot} = \underset{\theta_{23},|\Delta m^2_{31}|}{\text{Min}} \left[\chi^2_{INO} + \underset{\delta_{\text{CP}}}{\text{Min}}\ \chi^2_{LBL}\right] \tag{3.19}$$

3.5 Results and Discussions

3.5.1 Mass hierarchy sensitivity

The mass hierarchy sensitivity is calculated by taking a true set of parameters assuming NH(IH) as true hierarchy and is compared against the test parameters assuming the opposite hierarchy IH(NH). While calculating the hierarchy sensitivity, marginalization is done over θ_{23}, $|\Delta m^2_{31}|$ and δ_{CP} in the range depicted in Table 3.4 in the test events (unless otherwise mentioned) while θ_{12}, θ_{13} and Δm^2_{21} are kept fixed at their best-fit values.

In Figure 3.3 we present the hierarchy sensitivities as a function of true δ_{CP} for the experiments ESSνSB (2 years neutrino + 8 years anti-neutrino), T2K + NOνA (3 years neutrino + 3 years anti-neutrino), INO-3D, individually and combined with each other for four hierarchy-octant combinations. These are NH-LO, NH-HO, IH-LO and IH-HO. The representative true values of θ_{23} for LO and HO are chosen as 42° and 48° respectively.

The blue dashed lines in the plots represent the hierarchy sensitivity of ESSνSB. It is seen that for all the four cases hierarchy sensitivity of ESSνSB is more for CP conserving values (0°, $\pm 180^\circ$) than for CP violating values ($+90^\circ/-90^\circ$). Overall, for NH and $\theta_{23} = 42^\circ$, ESSνSB can have close to 2σ hierarchy sensitivity for all values of δ_{CP} reaching up to 3σ for $\delta_{\text{CP}} = \pm 180^\circ$. The CP dependence of hierarchy sensitivity for NH-HO is similar to that of NH-LO as can be seen from the right panel of the top row. However, the sensitivity is slightly higher because of the

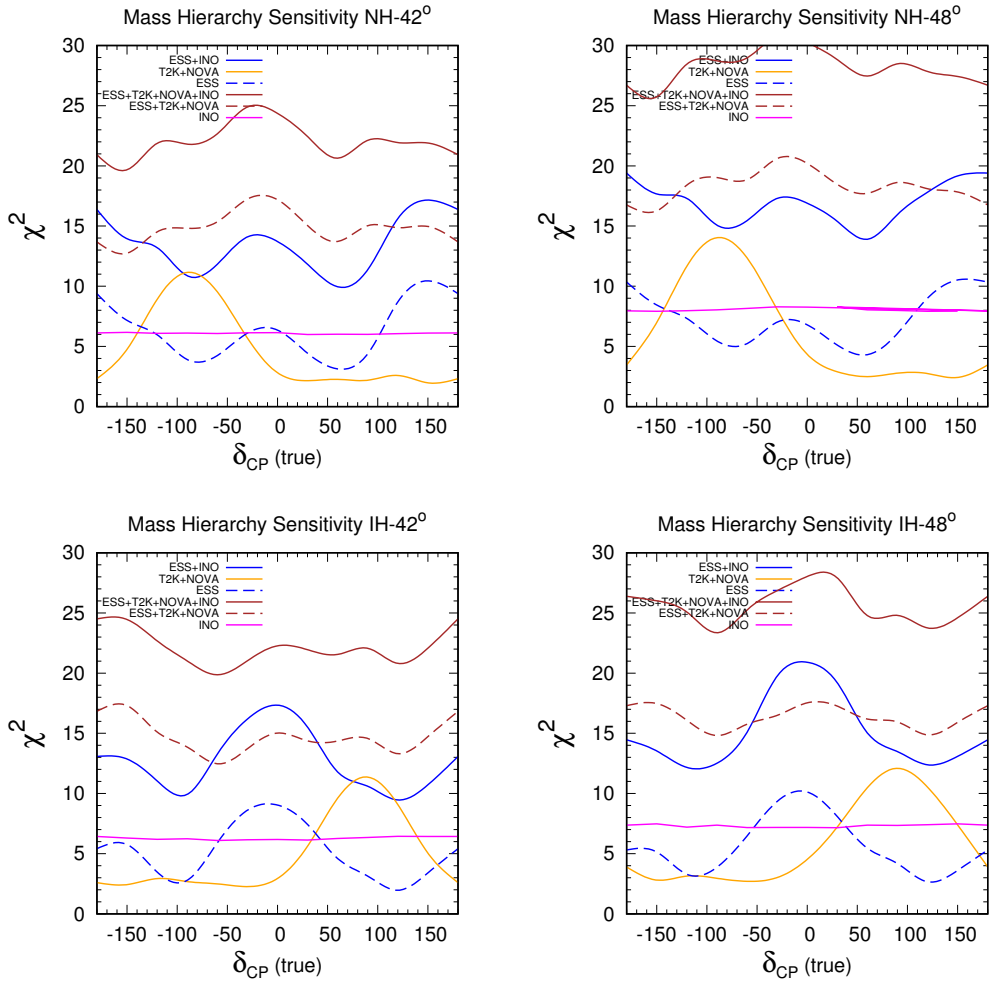

Figure 3.3: Mass hierarchy sensitivity vs. $\delta_{\rm CP}$ (true) for ICAL@INO-3D, ESSνSB , T2K, NOνA for four hierarchy-octant combinations starting from top right, clockwise in the order NH-LO, NH-HO, IH-HO and IH-LO. Each figure consists of six different experimental combinations which are represented as ICAL@INO (magenta solid curve), ESSνSB (blue dashed curve), T2K + NOνA (orange solid curve), ESSνSB + ICAL@INO (blue solid curve), ESSνSB + T2K + NOνA (brown dashed curve) and ESSνSB + T2K + NOνA + ICAL@INO (brown solid curve).

higher octant. The panels in the second row show the hierarchy sensitivity for IH-LO and IH-HO. In this case ESSνSB attains highest hierarchy sensitivity ($\sim 3\sigma$) for $\delta_{\rm CP} = 0^\circ$ but sensitivity is $< 2\sigma$ for $\delta_{\rm CP} = \pm 90^\circ$.

In order to understand the behavior of the hierarchy sensitivity χ^2 with $\delta_{\rm CP}$ in Figure 3.4 we plot the hierarchy χ^2 as a function of test-$\delta_{\rm CP}$ for only neutrino, only anti-neutrino and the mixed runs of 10ν+$0\bar{\nu}$ years, 0ν+$10\bar{\nu}$ years and 2ν+$8\bar{\nu}$

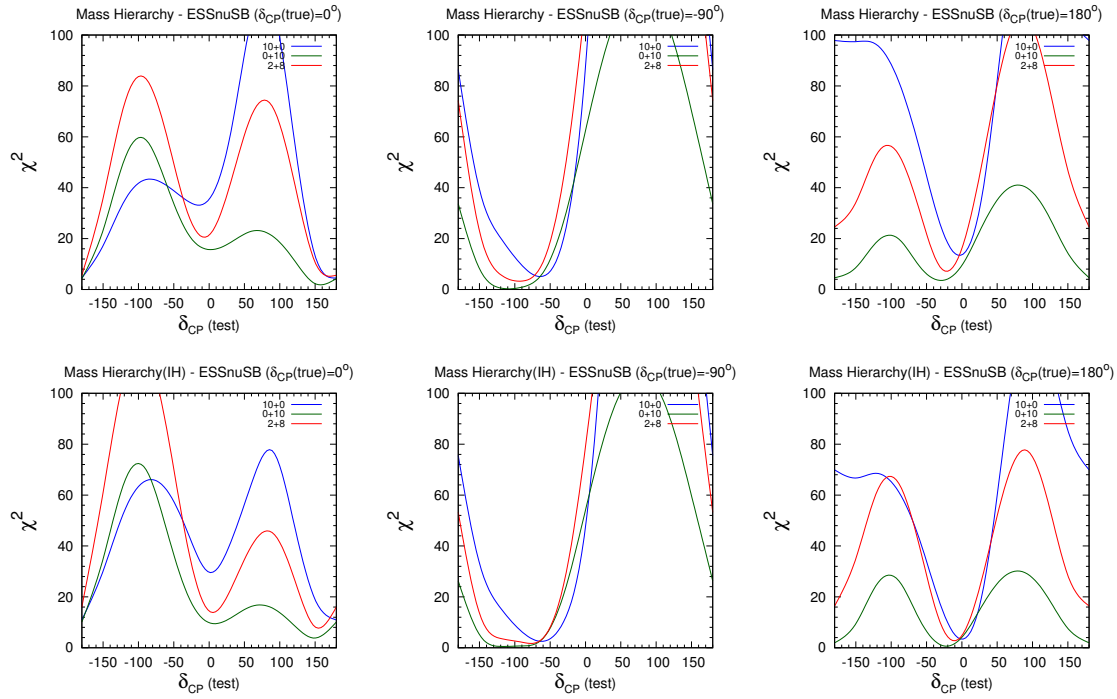

Figure 3.4: Mass hierarchy sensitivity vs $\delta_{\rm CP}$ (test) for ESSνSB with true $\delta_{\rm CP}$ fixed. The top row represents true NH while the bottom row represents true IH. The true octant is fixed as lower octant for all the plots. Each row has plots for three different $\delta_{\rm CP}$ (true), which are $0°$,$-90°$ and $180°$ from left to right in the given order. Each figure consists of three different runtime combinations of neutrino and anti-neutrino runs. The blue, green and red curves denote the runtime combinations (in years) of $10\nu + 0\bar{\nu}$, $0\nu + 10\bar{\nu}$ and $2\nu + 8\bar{\nu}$ respectively.

years respectively for the ESSνSB experiment. One can see that for $\delta_{\rm CP} = 0°$ the minimum for neutrinos come at $\pm 180°$ while that of anti-neutrinos occur at $150°$. Therefore, the position of the overall minimum combining neutrinos and anti-neutrinos is at $\delta_{\rm CP} = \pm 180°$. For $\delta_{\rm CP}$ (true) $= 180°$, the neutrino minimum is seen to be at $\delta_{\rm CP}$ (test) $= 0°$ whereas the anti-neutrino minimum at $\delta_{\rm CP}$ (test) $\approx -30°$ and $\pm 180°$. The overall minimum of 2ν+$8\bar{\nu}$ years runtime come at $\delta_{\rm CP} = -20°$. In comparison the figure drawn for true $\delta_{\rm CP} = -90°$ (the second panel in the first row) shows that the minimum for only neutrino run comes around $-60°$ whereas that for only anti-neutrino comes around $-110°$. Whereas the combined minimum occurs close to $-90°$. Thus for $\delta_{\rm CP} = -90°$ the wrong hierarchy minimum comes at the same CP value as compared to $\delta_{\rm CP}$ (true) $= 0°$, $\pm 180°$ where the wrong

hierarchy minima are farther from the true value and hence the tension is enhanced. Similar feature is observed in the IH-LO curves (in the lower panel) also. For $\delta_{\rm CP}$ (true) $= -90^\circ$ the minimum for only neutrino, only anti-neutrino and the combined runs occur in the same half plane as $\delta_{\rm CP} = -90^\circ$ whereas for true $\delta_{\rm CP} = 0^\circ$ the corresponding minimum occurs at $\pm 180^\circ$ and 150°. Similarly for $\delta_{\rm CP} = 180^\circ$, the minimum for only neutrino run is at 0°, for only anti-neutrino run is at -30° and the combined run is close to -10°. Thus for $\delta_{\rm CP} = -90^\circ$ the presence of WH-R$\delta_{\rm CP}$ degeneracy gives a lower sensitivity as compared to the CP conserving values, where the wrong hierarchy minimum comes at different wrong CP values for neutrino and anti-neutrino which enhances the tension and hence the χ^2. It is seen that the only neutrino run of ESSνSB can give a better hierarchy sensitivity because of statistics than the combined runs. However, the combined neutrino and anti-neutrino run is expected to give a higher CP sensitivity [182].

The magenta curves in Figure 3.3 represents the hierarchy sensitivity of ICAL@INO. Mass hierarchy sensitivity of ICAL@INO is independent of $\delta_{\rm CP}$ because of the sub-dominant effect of $\delta_{\rm CP}$ in survival probability and also due to smearing over directions [23, 24]. Hence, when ICAL@INO is added to other long-baseline accelerator experiments a constant increase in the sensitivity is observed. This helps to get reasonable sensitivity in the degenerate region. This is reflected by the blue solid curves which demonstrate the hierarchy sensitivity of ESSνSB + ICAL@INO. Since ICAL@INO has no dependence on $\delta_{\rm CP}$ the combined curve follows the ESSνSB curve. The combination of ESSνSB + ICAL@INO can give 3σ hierarchy sensitivity over the whole range of $\delta_{\rm CP}$ reaching 4σ for $\delta_{\rm CP} = \pm 180^\circ$ for NH-LO. For NH-HO, the combined sensitivity is more than 3.5σ for all values of $\delta_{\rm CP}$ crossing 4σ for $\pm 180^\circ$. For IH-LO, as can be seen from the second row first column of the Figure 3.3 the combined sensitivity of ESSνSB + ICAL@INO is more than $\sim 3\sigma$ for all values of $\delta_{\rm CP}$ and more than 4σ for $\delta_{\rm CP} = 0^\circ$. For IH-HO, the sensitivity at $\delta_{\rm CP} = 0^\circ$ can reach $\sim 4.5\sigma$.

The yellow curves in the different panels of Figure 3.3 represent the hierarchy sensitivity for T2K + NOνA. We see that for NH-LO/HO highest sensitivity occurs for $\delta_{\rm CP} \sim -90^\circ$ and the lower half plane (LHP, $-180^\circ < \delta_{\rm CP} < 0^\circ$) is seen to be favorable for hierarchy. This can be understood from the probability figures for T2K and NOνA in Figure 3.1. For instance NH-LO (the cyan band) and $\delta_{\rm CP} \sim -90^\circ$ does not show any degeneracy for anti-neutrinos. The degeneracy with IH-HO present for neutrinos can be resolved when neutrino and anti-neutrino are combined. Thus the LHP is conducive for hierarchy determination [193]. For true NH-HO, neutrino has no degeneracy for $\delta_{\rm CP} = -90^\circ$, whereas the WH-WO-R$\delta_{\rm CP}$ degeneracy observed in the anti-neutrino data (purple and green bands in the probability Figure 3.2) can be resolved when combined with neutrino data. Thus the LHP is favorable for hierarchy. For true IH-LO/HO the upper half plane(UHP, $0^\circ < \delta_{\rm CP} < 180^\circ$) is favorable for hierarchy, since there is no degeneracy for neutrinos (anti-neutrinos) for $\delta_{\rm CP}$ in the UHP.

When T2K + NOνA χ^2 is added to ESSνSB and marginalized, the CP dependence of the hierarchy sensitivity is governed by all the three experiments. The resultant curve shows highest sensitivity for $\delta_{\rm CP} = 0^\circ$ reaching 4σ level for both NH-LO and NH-HO. For IH, 4σ sensitivity is reached for HO for all values of $\delta_{\rm CP}$ and for $\delta_{\rm CP} = \pm 180^\circ$ for LO. Note that the hierarchy sensitivity for ESSνSB + ICAL@INO for certain values of $\delta_{\rm CP}$ could be higher than that of T2K + NOνA + ESSνSB.

The brown solid curve represents the combined hierarchy sensitivity of ESSνSB + T2K + NOνA + ICAL@INO and it shows sensitivity reach of $\chi^2 = 25$ for all values of $\delta_{\rm CP}$ NH-HO. For NH-LO 5σ sensitivity is reached for $\delta_{\rm CP} = 0^\circ$, while for IH-HO $\delta_{\rm CP} = 0^\circ, \pm 180^\circ$. For IH-LO, the sensitivity stays slightly higher than 4.4σ for all values of $\delta_{\rm CP}$. We have also observed a synergy between ICAL@INO and the accelerator based long-baseline experiments owing to $|\Delta m^2_{31}|$ tension. This tension happens because atmospheric data slightly prefers lower $|\Delta m^2_{31}|$ values while the

accelerator data supports the true value.

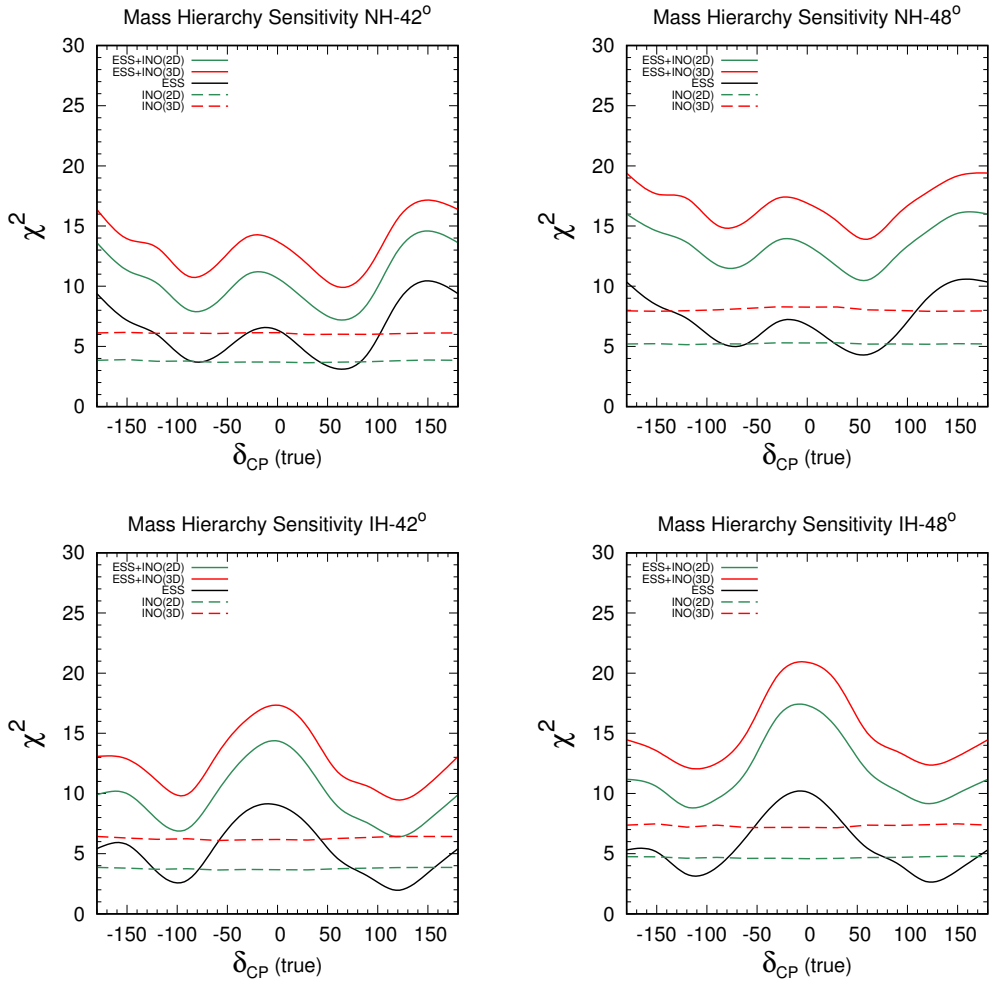

Figure 3.5: Mass hierarchy sensitivity vs $\delta_{\rm CP}$ (true) for ICAL@INO-3D, ICAL@INO-2D and ESSνSB for four hierarchy-octant combinations starting from top right, clockwise in the order NH-LO, NH-HO, IH-HO and IH-LO. Each figure consists of five different experimental combinations which are represented as ICAL@INO-2D (green dashed curve), ICAL@INO-3D (red dashed curve), ESSνSB (black solid curve), ESSνSB + ICAL@INO-2D (green solid curve) and ESSνSB + ICAL@INO-3D (red solid curve) .

In Figure 3.5 we compare and quantify the hierarchy sensitivity of ESSνSB + ICAL@INO for 2D and 3D analysis of the ICAL@INO experiment. The 3D analysis gives better hierarchy sensitivity over 2D because of the inclusion of hadron information in the analysis as described in Section 3.3.

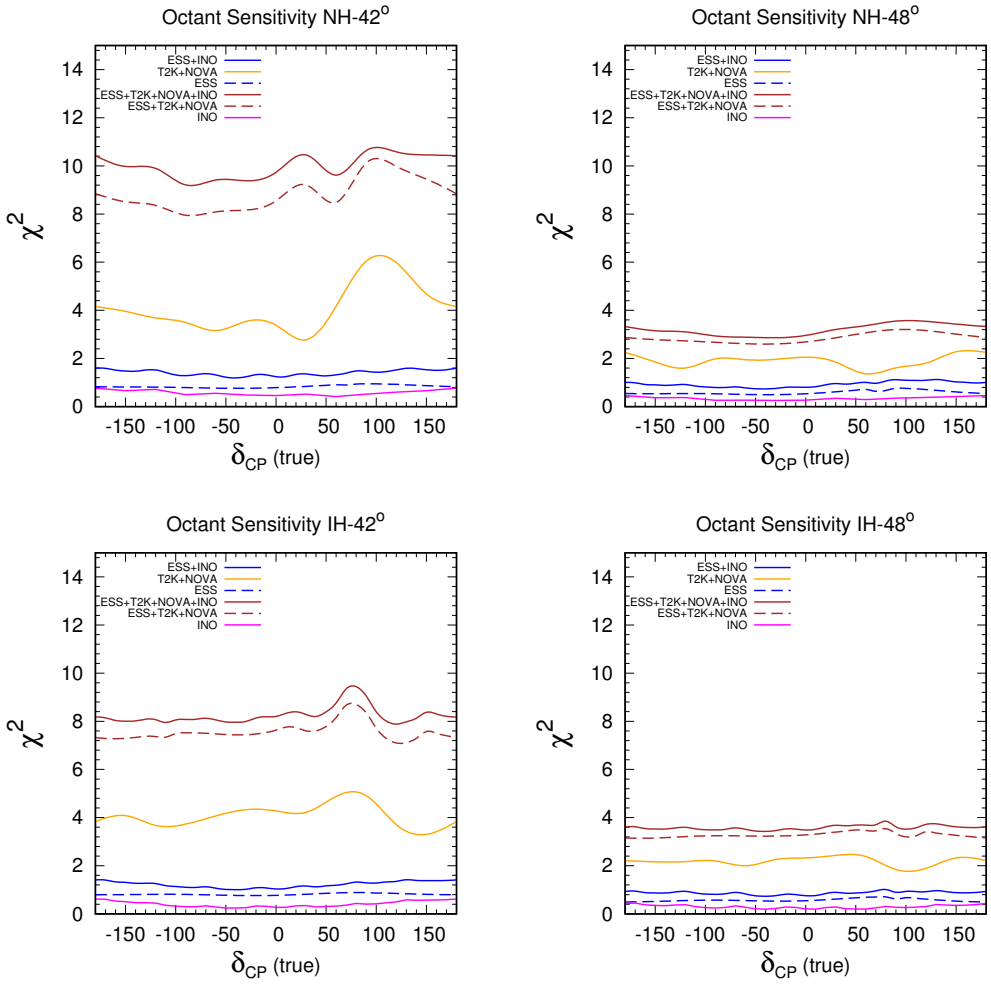

Figure 3.6: Octant sensitivity vs $\delta_{\rm CP}$ (true) for ICAL@INO-3D ESSνSB T2K NOνA for four hierarchy-octant combinations starting from top right, clockwise in the order NH-LO, NH-HO, IH-HO and IH-LO. Each figure consists of six different experimental combinations which are represented as ICAL@INO (magenta solid curve), ESSνSB (blue dashed curve), T2K + NOνA (orange solid curve), ESSνSB + ICAL@INO (blue solid curve), ESSνSB + T2K + NOνA (brown dashed curve) and ESSνSB + T2K + NOνA + ICAL@INO (brown solid curve).

3.5.2 Octant sensitivity

To calculate the octant sensitivity we simulate the data for a representative value of true θ_{23} belonging to LO (HO) and test it by varying θ_{23} in the opposite octant i.e. HO (LO) along with marginalization over $|\Delta m^2_{31}|$, hierarchy and $\delta_{\rm CP}$ (for LBL experiments). The plots in Figure 3.6 show the octant sensitivity for the various experiments. The magenta curves denote the octant sensitivity of ICAL@INO

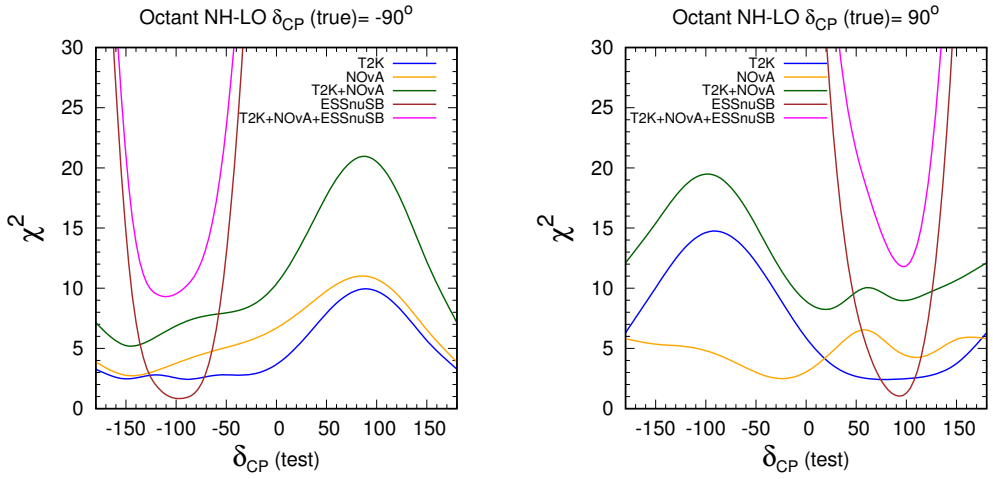

Figure 3.7: Octant sensitivity vs $\delta_{\rm CP}$ (test) for ESSνSB , T2K and NOνA with $\delta_{\rm CP}$ (true) = $\pm 90°$. The true hierarchy and true octant are taken as NH and LO respectively. Left panel represents the octant sensitivities for $\delta_{\rm CP}$ (true) = $-90°$ and the right panel $\delta_{\rm CP}$ (true) = $+90°$. Each figure consists of five different experimental combinations which are represented as T2K (blue solid curve), NOνA (orange solid curve), ESSνSB (brown solid curve), T2K + NOνA (green solid curve), ESSνSB + T2K + NOνA (magenta solid curve).

including the hadron information. It is seen that ICAL@INO has very poor octant sensitivity ($\sim< 1\sigma$). Although as discussed earlier, the matter effect can break octant degeneracy the sensitivity is low for ICAL@INO, since it can detect only the muon signal. This gets contribution from both $P_{\mu\mu}$ and $P_{e\mu}$ probabilities and the octant sensitivity are opposite which reduces the sensitivity.

T2K, NOνA and ESSνSB are accelerator experiments which can detect both the appearance and disappearance channels separately. The blue dashed line denotes the octant sensitivity of ESSνSB which is again $< 1\sigma$ for all the four hierarchy octant combinations. As we have seen from the discussion on probabilities, that ESSνSB suffers from octant degeneracy over the whole range of $\delta_{\rm CP}$ for the E1 and E3 bins. Thus, the octant χ^2 gets contribution mainly from the bin E2.

The solid yellow line in Figure 3.6 represents the combined octant sensitivity for T2K + NOνA. This combination has $\sim 2\sigma$ octant sensitivity for most of the $\delta_{\rm CP}$ range for true NH-LO and IH-LO with peak sensitivity reaching up to $\sim 2.4\sigma$ and $\sim 2.2\sigma$ at $\delta_{\rm CP} \sim 90°$ respectively. The combination of neutrino and anti-

neutrino run help in removing the degenerate wrong octant solutions [25–27, 155]. There can also be some synergy between T2K and NOνA which can enhance octant sensitivity. For instance for true NH-LO, we find a higher sensitivity in the upper half plane of $\delta_{\rm CP}$ near $\delta_{\rm CP} \sim 100°$. This happens because of synergy between T2K and NOνA. This can be understood from the Figure 3.7 where we plot the octant sensitivity χ^2 vs test-$\delta_{\rm CP}$ for T2K, NOνA and ESSνSB for NH-LO and two representative values of true $\delta_{\rm CP} = \pm 90°$. It is seen that for $\delta_{\rm CP} = -90°$ the minimum of NOνA, T2K and the combined χ^2 of NOνA and T2K, represented by the blue, yellow and the green lines come around $-150°$. But for $\delta_{\rm CP}$ =90° the minimum of T2K comes close to +90° but the minimum of NOνA comes close to $\delta_{\rm CP} \sim -20°$. The combined minimum comes at $\sim \delta_{\rm CP} = 20°$ where the T2K and NOνA contributions are higher than that at their individual minimum. This synergy gives a higher χ^2 in the UHP.

For IH-LO (green band in the probability Figure 3.1), the neutrino probability has no degeneracy for $\delta_{\rm CP}$ belonging to the upper half plane. The anti-neutrino probabilities for $\delta_{\rm CP}$ in upper half plane has degeneracy with NH-HO at same $\delta_{\rm CP}$ (purple band) and IH-HO with $\delta_{\rm CP}$ in the lower half plane. But since neutrino events have larger statistics, higher sensitivity is obtained for $\delta_{\rm CP}$ in the upper half plane.

For true NH-HO and IH-HO, the sensitivity is much lower with $\sigma \approx 1.4$ over the full range of $\delta_{\rm CP}$. The χ^2 is lower for HO in general. This is because the $\chi^2 \sim (N_{HO(LO)} - N_{LO(HO)})/N_{HO(LO)}$ for true HO(LO). We see that the numerator is same for both cases whereas the denominator is larger for a true higher octant resulting in a lower sensitivity.

When T2K + NOνA is combined with ESSνSB (shown by the dashed brown lines in the Figure 3.6) an enhancement is observed with the octant sensitivity reaching $\sim 3\sigma$ at $\delta_{\rm CP} \sim 90°$ for true NH-LO while the octant sensitivity reaches $\sim 2.9\sigma$ for true IH-LO at the same $\delta_{\rm CP}$. But the octant sensitivities are $\sim 1.7\sigma$ for

true NH-HO and IH-HO.

It is interesting to understand the enhancement of the octant sensitivity of T2K + NOνA when combined with ESSνSB . This synergy can be understood from Figure 3.7. The brown curve in this figure denotes the octant sensitivity of ESSνSB as a function of test $\delta_{\rm CP}$ while the magenta curve denotes the combined sensitivity of T2K + NOνA + ESSνSB . The left panel represents the plots with $\delta_{\rm CP}$ (true) $= -90^\circ$ while right panel represents $\delta_{\rm CP}$ (true) $= 90^\circ$. Analyzing the first panel i.e. NH-LO and $\delta_{\rm CP}$ (true) $= -90^\circ$ it is seen that the minimum for both T2K and NOνA come at $\delta_{\rm CP}$ (test) $= -150^\circ$ hence there is no synergy between T2K and NOνA as discussed earlier. But, the ESSνSB minimum is at $\delta_{\rm CP}$ (test) $= -100^\circ$ therefore the overall minimum is shifted towards $\delta_{\rm CP}$ (test) $= -120^\circ$, which gives rise to significant synergy between ESSνSB and T2K + NOνA which can be seen from the magenta curve in Figure 3.7.

The variation in the octant sensitivity χ^2 with $\delta_{\rm CP}$ (test) is seen to be very rapid for ESSνSB hence it controls the overall shape of the combined octant sensitivity curve and the position of the minimum. As we have discussed earlier, the octant sensitivity for ESSνSB is contributed by the bin with mean energy 0.35 GeV. As can be seen from Figure 3.2, the probability for this bin has a sharp variation with $\delta_{\rm CP}$. Thus a slight shift in the $\delta_{\rm CP}$ value can cause a large change in the probability and hence in the χ^2. Similar feature can also be observed in the second panel for NH-LO and true $\delta_{\rm CP} = 90^\circ$.

Addition of ICAL@INO with T2K + NOνA + ESSνSB represented by the solid brown curves, results in slightly higher sensitivity. In this case for true NH-LO 3σ octant sensitivity is obtained. For true IH-LO the octant sensitivity reaches close to $\sim 3\sigma$ at $\delta_{\rm CP} \sim 90^\circ$. While for true NH-HO and IH-HO the total sensitivity obtained is close to 2σ. Adding ICAL@INO, results in a constant increase in the χ^2, since the ICAL@INO χ^2 is almost independent of $\delta_{\rm CP}$.

3.6 Conclusions

The ESSνSB experiment is planned for discovery of $\delta_{\rm CP}$ with a high significance using the second oscillation maximum. In this work, we show how the hierarchy sensitivity of the ESSνSB experiment can be enhanced by combining with the atmospheric neutrino data at the proposed ICAL detector of the ICAL@INO collaboration as well as the data from the ongoing T2K and NOνA experiments assuming their full projected runs. We present our results for four true hierarchy - octant combination : NH-LO, NH-HO, IH-LO, IH-HO taking representative values of $\theta_{23} = 42^\circ$ for LO and 48° for HO. We find that ESSνSB has $\sim 2(3)\sigma$ hierarchy sensitivity over the majority of $\delta_{\rm CP}$ values for the above hierarchy octant combinations. The mass hierarchy sensitivity of ICAL@INO is independent of $\delta_{\rm CP}$ and adding ICAL data to ESSνSB helps to enhance this to $3(4)\sigma$ depending on hierarchy, octant and $\delta_{\rm CP}$ value. Addition of T2K + NOνA to this combination raises the hierarchy sensitivity farther and 5σ sensitivity to mass hierarchy can be reached. The overall conservative sensitivities (best sensitivities) for the various hierarchy octant combinations are as follows:

- NH-LO : $\sim 4.4(5)\sigma$
- NH-HO : $\sim 5(5.5)\sigma$
- IH-LO : $\sim 4.5(5)\sigma$
- IH-HO : $\sim 4.8(5.3)\sigma$

We have also explored to what extent the octant sensitivity of ESSνSB can be improved by combining with ICAL@INO and T2K and NOνA simulated data. We find that ICAL@INO itself has very low octant sensitivity due to opposite interplay of the survival and appearance channels nullifying the octant sensitivity. However when T2K + NOνA data is added $2(3)\sigma$ octant sensitivity can be achieved. Additionally, we have shown that despite of the poor octant sensitivity of ESSνSB,

it can have interesting synergy with T2K + NOνA owing to the rapid variation of $P_{\mu e}$ with respect to $\delta_{\rm CP}$ at the second oscillation maximum. Hence, combining ESSνSB with T2K + NOνA significantly increases the combined χ^2.

In conclusion, our analysis underscores the importance of exploring the synergies between the ongoing experiments T2K and NOνA and the ESSνSB experiment and atmospheric neutrino experiment ICAL@INO to give enhanced sensitivity.

Chapter 4

Study of neutrino decay with ICAL using atmospheric neutrinos

4.1 Introduction

Neutrino oscillation has been established as the dominant solution to the solar and atmospheric neutrino anomalies. These have been corroborated by reactor and accelerator based experiments. However, future/proposed high precision experiments can also probe new physics scenarios which can be subleading effects over the dominant oscillation solution. Several new physics scenarios have been considered in the literature. This includes non standard interactions (NSI), non unitarity, long range force etc. The neutrino oscillation probabilities would change in the presence of new physics. This could be used to constrain new physics scenarios at neutrino oscillation experiments. At the same time, a given new physics scenario could also interfere with the measurement of the standard neutrino oscillation parameters and hence pose a challenge to the proposed experiments, unless ways are found to cancel out their effects through synergistic measurements at multiple experiments. In this chapter (based on [194]) we consider the possibility of invisible neutrino decay and probing this scenario at INO.

While there is no observational evidence in support for unstable neutrinos, since they are massive, its not unlikely that they would decay. Radiative decays of neutrinos are severely constrained by cosmological data. Since the measured neutrino masses suggest that the neutrinos would radiatively decay in the microwave energy range, the most stringent bounds are provided by cosmic microwave background data [195], making radiative decay of neutrinos totally uninteresting for neutrino oscillation experiments. However, there still remains the possibility that neutrinos could decay into a lighter fermion state and a beyond standard model boson. The Majoron model [196–198] for instance allows the following decay modes for Majorana neutrinos: $\nu_i \to \nu_j + J$ or $\nu_i \to \bar{\nu}_j + J$, where ν_j and $\bar{\nu}_j$ are lighter neutrino and anti-neutrino states and J is a Majoron. The Majoron in principle could belong to either a singlet or a triplet representation of the standard model gauge group. But the triplet model is severely constrained [197, 198]and hence J must predominantly be an electroweak singlet. If the final state fermion is a lighter active neutrino, the decay is called *visible decay*. On the other hand, if the final state fermion is a sterile state with no standard model interaction, then the decay scenario is termed *invisible decay*. Even for Dirac neutrinos in extensions of the standard models one could write down terms in the Lagrangian coupling neutrinos with a light scalar boson and light right-handed neutrinos allowing the decay mode $\nu_i \to \bar{\nu}_{iR} + \chi$, where $\bar{\nu}_{iR}$ is a right-handed singlet neutrino and χ is an iso-singlet scalar carrying lepton number +2 [199, 200]. In this chapter, we will work in a scenario where the final state particles remain invisible to the detector.

The lifetime of ν_2 (and ν_1) is constrained by the solar neutrino experiments. Neutrino decay as a solution to the solar neutrino deficit problem was suggested in [201], however, now we know that neutrino decay alone cannot explain this deficit. Attempts to constrain the neutrino lifetime by considering neutrino decay as a sub-dominant effect along with the leading LMA-MSW solution was done in [28–31, 202–206]. Most of these studies considered the invisible decay scenario. Since

U_{e3} is small, the ν_e state mostly resides in the ν_2 and ν_1 states and hence all of these studies worked in the two-generation framework. Bounds on the lifetime of ν_2 was obtained from a global analysis of solar neutrino data in [29] where the impact of the Sudbury Neutrino Observatory neutral current data was highlighted. It was shown that the bound on ν_2 lifetime was $\tau_2/m_2 > 8.7 \times 10^{-5}$ s/eV at 99% C.L. for a 3 parameter fit. This bound was revisited in [30] (see also [31]) where the authors obtained the 95% C.L. limit $\tau_2/m_2 > 7 \times 10^{-4}$ s/eV for both normal and inverted mass hierarchy and $\tau_1/m_1 > 4 \times 10^{-3}$ s/eV for inverted mass hierarchy. These results are very consistent with the earlier analysis of [29] where the 95% C.L. limit for a one parameter fit is seen to be $\tau_2/m_2 > 4.4 \times 10^{-4}$ s/eV. The corresponding constraints from SN1987A are stronger [207].

Limits on the lifetime of ν_3 come from the atmospheric and long-baseline neutrino experiments. Like in the case of solar neutrinos, any fit with neutrino decay alone [208, 209] is unable to explain the atmospheric neutrino zenith angle data. A lot of work has gone into considering decay along with oscillations. The analyses can be broadly classified into two categories depending on the model used. If one considers decay of ν_3 to a state with which it oscillates, then the bounds coming from K-decays [210] restrict the corresponding mass squared difference between them to $\Delta m^2 > 0.1$ eV^2 [211]. However, if the state to which ν_3 decays is a sterile state then the Δm^2 driving the leading oscillations of ν_μ is unconstrained. The former case is that of decay to active neutrinos and was studied in the context of atmospheric neutrinos in [211, 212] and no good fit was found. The latter is the invisible decay scenario to sterile neutrinos and was analyzed against the atmospheric neutrino data in [32, 213–215]. The invisible decay case can be again classified into two. In one case we can make the assumption that $\Delta m^2 \ll 10^{-4}$ eV^2, causing it to drop out of the oscillation probability. The authors of [214] argued that this could explain the Super-Kamiokande atmospheric neutrino data, however, the Super-Kamiokande collaboration itself reported [215] that this scenario

was not supported by their data. The other case of invisible decay is when Δm^2 is left free in the fit to be determined by the data. This case was first mentioned in [213]. The results of [213] were updated in [32] where the authors obtained the limit $\tau_3/m_3 > 2.9 \times 10^{-10}$ s/eV for invisible decay at the 90% C.L. from a combined analysis of Super-Kamiokande atmospheric and MINOS data. More recently, the analysis of oscillation plus invisible decay scenario with unconstrained Δm^2 was performed in [33] in the context of MINOS and T2K data and gave a bound $\tau_3/m_3 > 2.8 \times 10^{-12}$ s/eV at 90% C.L. The constraint for the visible decay scenario using the MINOS and T2K charged as well as neutral current data was performed in [216]. The bounds on neutrino lifetime could be improved considerably by observations at IceCube using cosmological baselines [217–220].

All the above mentioned papers which considered neutrino decay alongside oscillations performed their analysis in the framework of two-generations and did not take Earth matter effects into account. Recently a three-generation analysis including Earth matter effect and decay in the context of the Deep Underground Neutrino Experiment (DUNE) was performed in [221] for visible decays and [222] for invisible decays. It was shown that DUNE could improve the bound on τ_3/m_3 for the invisible decay case by at least an order of magnitude compared to the current limits from MINOS and T2K. In this work, we consider invisible neutrino decay within a three-generation oscillation framework in the context of atmospheric neutrinos and include Earth matter effects. Atmospheric neutrinos span many orders of magnitude in energy and baseline. Since the effect of neutrino decay increases for lower energies and longer baselines, atmospheric neutrino experiments are expected to give a tighter bound on τ_3/m_3 than the proposed long-baseline experiments. We will study the sensitivity of the atmospheric neutrinos at INO to neutrino decay.

Some of the other new physics scenarios studied by the INO collaboration include, CPT violation [223], dark matter [224], non-standard neutrino interactions [225] and sterile neutrino oscillations [226]. In this work we will study in detail

the sensitivity of ICAL to invisible neutrino decay using the full physics analysis simulation framework of ICAL. We will also study the effect of invisible neutrino decay on the precision measurement of $|\Delta m^2_{32}|$ and the mixing angle θ_{23}.

This chapter is organized as follows. The scenario of invisible decay plus oscillations for three–generation mixing and oscillations in Earth matter are discussed in Section 4.2. The simulation of events and χ^2 analysis are explained in Section 4.3. In Section 4.4 we present our results for the sensitivity to the decay parameter τ_3/m_3. The effects of the presence of decay on the precision measurements of $\sin^2\theta_{23}$ and $|\Delta m^2_{32}|$ are discussed in Sections 4.5.1 and 4.5.2 respectively. The exclusion contours are presented in Section 4.5.3. Conclusions are presented in Section 4.7.

4.2 Invisible decay and oscillations in the presence of matter

In this section we consider the oscillations and decay of ν_3 in the presence of matter. Let the state ν_3 decay invisibly via $\nu_3 \rightarrow \nu_s + J$, where J is a pseudo-scalar and ν_s is a sterile neutrino. Since ν_s does not mix with the three active neutrinos, the mixing matrix U in vacuum [227–229] is given by :

$$U = \begin{pmatrix} c_{12}c_{13} & s_{12}c_{13} & s_{13}e^{-i\delta} \\ -c_{23}s_{12} - s_{23}s_{13}c_{12}e^{i\delta} & c_{23}c_{12} - s_{23}s_{13}s_{12}e^{i\delta} & s_{23}c_{13} \\ s_{23}s_{12} - c_{23}s_{13}c_{12}e^{i\delta} & -s_{23}c_{12} - c_{23}s_{13}s_{12}e^{i\delta} & c_{23}c_{13} \end{pmatrix}, \quad (4.1)$$

where $c_{ij} = \cos\theta_{ij}$, $s_{ij} = \sin\theta_{ij}$; θ_{ij} are the mixing angles and δ is the CP violating phase.

The mass of ν_s is such that when the hierarchy is normal, $m_s < m_1 < m_2 < m_3$. Since ν_s does not mix with the active neutrinos, the propagation equation is not affected by this. The effect of decay is included in the three-flavor evolution

equation in the presence of Earth matter as follows :

$$i\frac{d\tilde{\nu}}{dt} = \frac{1}{2E}\left[U\mathbb{M}^2U^\dagger + \mathbb{A}_{CC}\right]\tilde{\nu}, \tag{4.2}$$

$$\mathbb{M}^2 = \begin{pmatrix} 0 & 0 & 0 \\ 0 & \Delta m^2_{21} & 0 \\ 0 & 0 & \Delta m^2_{31} - i\alpha_3 \end{pmatrix}, \text{ and } \mathbb{A}_{CC} = \begin{pmatrix} A_{cc} & 0 & 0 \\ 0 & 0 & 0 \\ 0 & 0 & 0 \end{pmatrix}, \tag{4.3}$$

where E is the neutrino energy, $\alpha_3 = m_3/\tau_3$ is the decay constant in units of eV^2, m_3 is the mass of ν_3 and τ_3 its rest frame life time. Since the term α_3 appears in the propagation equation along with Δm^2_{31}, it has to be in units of eV^2. The conversion factor used here is $1\ \text{eV/s} = 6.58 \times 10^{-16}\ \text{eV}^2$. The matter potential is

$$A_{cc} = 2\sqrt{2}G_F n_e E = 7.63 \times 10^{-5}\text{eV}^2\ \rho(\text{gm/cc})\ E(\text{GeV}), \tag{4.4}$$

where, G_F is the Fermi constant and n_e is the electron number density in matter and ρ is the matter density. For anti-neutrinos, both the sign of A_{cc} and the phase δ in Equation 4.2 are reversed.

4.2.1 Effect of the decay term

The decay term is of the form of $\exp(-\alpha L/E)$. No decay corresponds to $\alpha = 0$ and the exponential term as 1 whereas complete decay will be when the exponential term tends to 0. The effect of the decay parameter α for various L/E values can be understood from Figure 4.1 in which $\exp(-\alpha L/E)$ vs L/E is plotted for the values $\alpha = 10^{-3}$, 10^{-4}, 10^{-5} and 10^{-6} eV^2. This figure gives an indication towards what are the values of α to which a given experiment spanning a specified L/E range can be sensitive to. For instance the red shaded region in Figure 4.1 indicates the L/E range covered by the narrow band NOνA neutrino beam (E = 1–3 GeV). It can be seen from the figure that NOνA's sensitivity is limited to larger values

of α; i.e. 10^{-3} and 10^{-4} eV^2 for which the exponential terms shows substantial departure from the no decay value of 1. The blue shaded region corresponds to the baseline $L = 9700$ km with $E = 0.5$–25 GeV, respectively. These are the typical values for an atmospheric neutrino experiment. This range of L/E is sensitive to a wider range of α from $\sim 10^{-6} - 10^{-3}$ eV^2 owing to the fact that it covers more L/E. The ranges of $\exp(-\alpha L/E)$ values for various values of α accessible for the specified range of L/E for a given baseline is shown in Table 4.1.

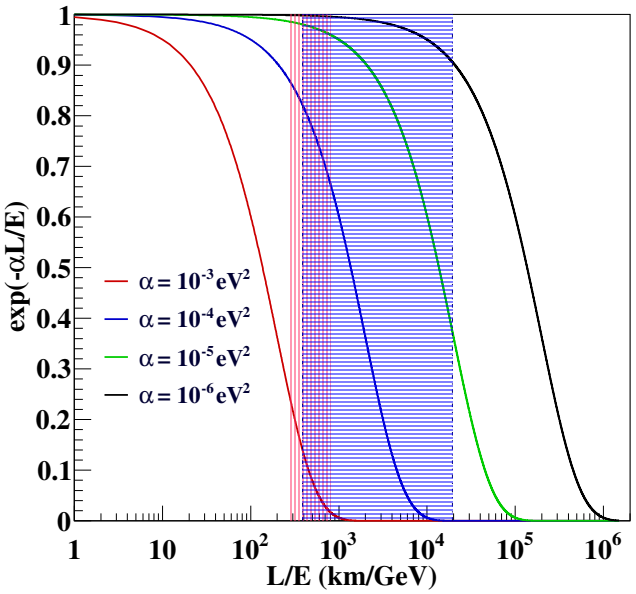

Figure 4.1: The value of $\exp(-\alpha L/E)$ as a function of L/E for different values of the decay parameter α. The red shaded region denotes the L/E range accessible with NOνA narrow band neutrino beam ($E = 1$–3 GeV) the dashed blue shaded region indicates the range for $L = 9700$ km, when E is in the range 0.5–25 GeV.

For a given L, a broader range of E will improve the sensitivity to α; on the other hand for a given E range the sensitivity to α will increase if longer baselines are available. In principle any experiment which spans over a wide range of L/E will have a better sensitivity to decay; with larger L/Es being sensitive to smaller values of α and vice versa. Atmospheric neutrino oscillation experiments fulfill this exact requirement. If we consider the neutrino energy range of 0.5–25 GeV, atmospheric neutrinos will span the L/E range of [0.6, 25484] (km/GeV) which includes all possible baselines from 15 km to the Earth's diameter. The INO ICAL

L (km)	L/E (min) (km/GeV)	L/E (max) (km/GeV)	α (eV^2)	$\exp(-\alpha L/E)$ (min)	$\exp(-\alpha L/E)$ (max)
810	270	810	10^{-3}	0.016	0.254
			10^{-4}	0.663	0.872
			10^{-5}	0.959	0.986
			10^{-6}	0.996	0.998
9700	388	19400	10^{-3}	0	0.14
			10^{-4}	0	0.82
			10^{-5}	0.37	0.98
			10^{-6}	0.91	1

Table 4.1: Allowed ranges of L/E in km/GeV for two fixed baselines 810 km and 9700 km with detectable neutrino energies as 1–3 GeV and 0.5–25 GeV respectively. The maximum and minimum values of $\exp(-\alpha L/E)$ for various α values for these L/Es are also shown.

detector becomes relevant in this context. ICAL can detect neutrinos in the range 0.5–25 GeV [230] and since it is an atmospheric neutrino experiment, it will be sensitive to a wide range of α values. As seen from Figure 4.1 ICAL should give a sensitivity to $\alpha = 10^{-6}$ eV^2 also. The sensitivity to low α values come from the low energy part of the spectrum, while the higher energy parts of the spectrum will help us rule out larger values of α.

4.2.2 Full three-flavor oscillations with decay in Earth matter

We perform an exact numerical calculation of the neutrino oscillation probabilities within the framework of three-generation mixing and invisible decay of ν_3. The oscillation probabilities are computed in the presence of Earth matter assuming the PREM density profile [231]. The oscillation probabilities $P_{\mu\mu}$, $P_{e\mu}$, $\bar{P}_{\mu\mu}$ and $\bar{P}_{e\mu}$ as a function of neutrino energy for the baseline $L = 9700$ km, for various values of the decay parameter α_3 and θ_{23} are shown in Figure 4.2. The following values have been used to generate these.

1. $\delta_{\rm CP} = 0^\circ$

2. $\theta_{12} = 34.08°$; $\theta_{23} = 39°,\ 45°,\ 51°$; $\theta_{13} = 8.5°$

3. $\Delta m^2_{21} = 7.6 \times 10^{-5}(\text{eV}^2)$; $|\Delta m^2_{32}| = 2.4 \times 10^{-3}(\text{eV}^2)$

4. $\alpha_3 = 0,\ 10^{-4},\ 10^{-3}\ (\text{eV}^2)$

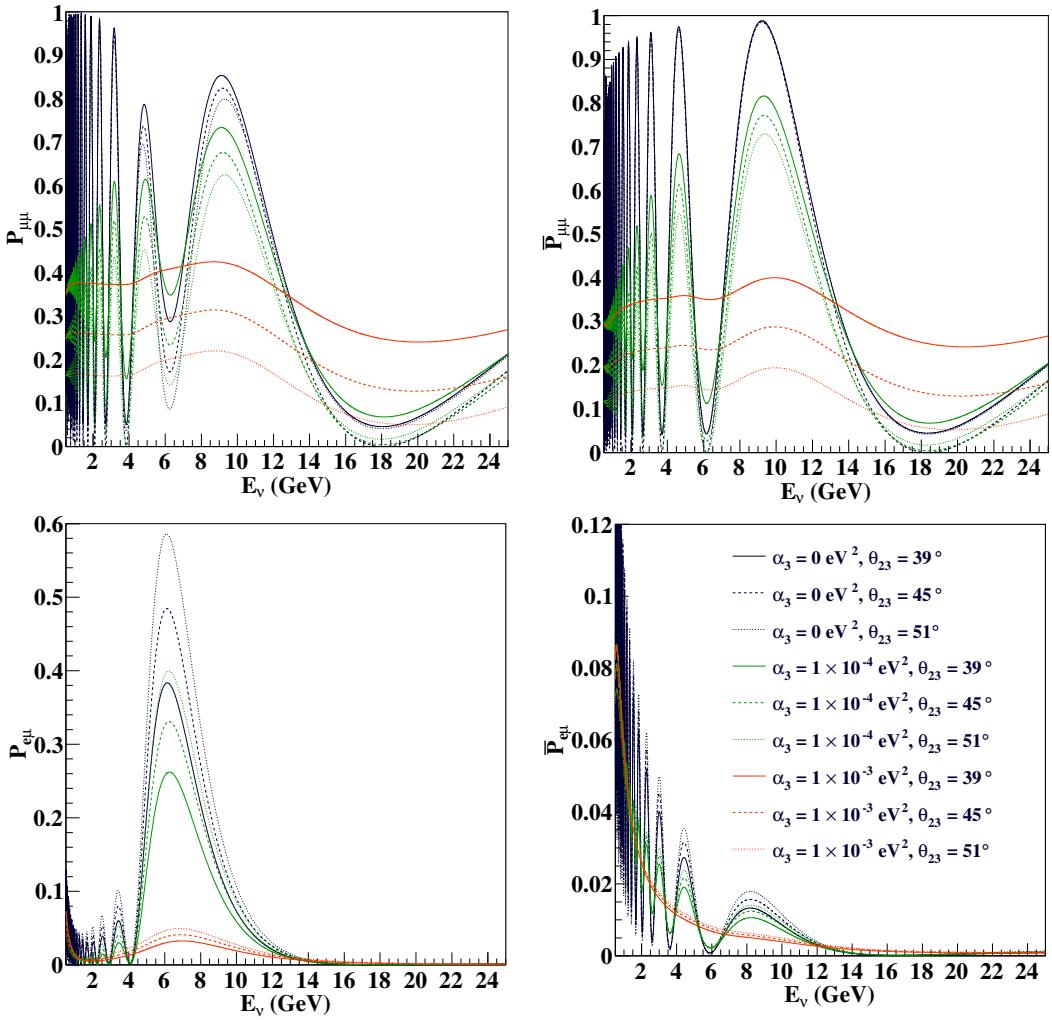

Figure 4.2: Oscillation probabilities in matter for $\alpha_3 = 0,\ 1 \times 10^{-4}$ and 1×10^{-3} eV^2 and $\theta_{23} = 39°, 45°$ and $51°$, for the baseline $L = 9700$ km in the energy range $E_\nu =$ 0.5–25 GeV. (Top-left) $P_{\mu\mu}$ and (top-right) $\bar{P}_{\mu\mu}$; (bottom-left) $P_{e\mu}$ and (bottom-right) $P_{\mu\mu}$. NH is taken as the true hierarchy. It should be noted that the ranges for the y-axes are not the same.

First let us consider the effect of α_3 alone for a given θ_{23}. The plots for $\alpha_3 = 0$ correspond to the oscillation only case and as the value of α_3 increases the effect of decay becomes prominent which can be seen from the Figure 4.2 . In general the effect of decay is seen to be more for the lower energy neutrinos. For the decay

constant $\alpha_3 = 10^{-4}$ eV^2, the effect of decay increases and the neutrino probabilities show significant depletion as compared to the no decay case for neutrino energies up to $\sim$ 15 GeV. The presence of decay reduces the oscillation amplitude near maxima and elevates it near minima. As α_3 increases to 10^{-3} eV^2, the survival probability of the neutrino and anti-neutrinos show a difference over the entire energy range considered. We also note that the effect of decay is mainly to damp out the oscillatory behavior in the probabilities. For the large decay case the oscillatory behavior is seen to be largely washed out. From Figure 4.2 it can be seen that, the relative change in the oscillation probability due to decay is more for $\bar{P}_{\mu\mu}$ than $P_{\mu\mu}$ whereas the relative change in $P_{e\mu}$ is more compared to that in $\bar{P}_{e\mu}$. Hence the contribution to the α_3 sensitivity χ^2 will be more from anti-neutrino events in the former case and neutrino events in the latter case. However since $P_{\mu\mu}$ and $\bar{P}_{\mu\mu}$ are the dominant channels at ICAL, the major contribution to α_3 sensitivity is expected to come from anti-neutrino events in the present study.

Now let us look at the effect of θ_{23} alone for a given α_3 value. The effect of θ_{23} is also to vary the oscillation amplitude. In general, $P_{\mu\mu}$ and $\bar{P}_{\mu\mu}$ decrease with increase in θ_{23}. However beyond 13 GeV, for $\alpha_3 = 0$ and 10^{-4} eV^2, $\theta_{23} = 45^\circ$ gives the lowest probability compared to those for 39° and 51°, though the relative variation is much less. From the plots in the lower panels of Figure 4.2 we see that $P_{e\mu}$ and $\bar{P}_{e\mu}$ increase with θ_{23}, the increase in $P_{e\mu}$ is larger than that in $\bar{P}_{e\mu}$. For all values of θ_{23}, $P_{e\mu}$ and $\bar{P}_{e\mu}$ decrease.

Since both α_3 and θ_{23} affect the oscillation amplitudes, when combined in the following way, similar probabilities can be obtained. The combination of θ_{23} in the first octant + a larger (smaller) value of α_3 will give a probability similar to that with θ_{23} in second octant + a smaller (larger) value of α_3 for $P_{\mu\mu}$ and $\bar{P}_{\mu\mu}$ ($P_{e\mu}$ and $\bar{P}_{e\mu}$). Since the event spectrum is dominated by $P_{\mu\mu}$ and $\bar{P}_{\mu\mu}$ events, this combined effect will affect the sensitivity/discovery potential to/of α_3 and the precision measurement on θ_{23} ,which is discussed in Section 4.5.

4.3 Details of numerical simulations

ICAL will be a 50 kt magnetized iron detector which is optimized for the detection of atmospheric ν_μ and $\bar{\nu}_\mu$. Both ν_μ ($\bar{\nu}_\mu$) and ν_e ($\bar{\nu}_e$) fluxes can contribute to the ν_μ ($\bar{\nu}_\mu$) events observed at ICAL. Hence the number of events detected by ICAL will be :

$$\frac{d^2N}{dE_\mu d\cos\theta_\mu} = t \times n_d \times \int dE_\nu d\cos\theta_\nu d\phi_\nu \times \left[P^m_{\mu\mu}\frac{d^3\Phi_\mu}{dE_\nu d\cos\theta_\nu d\phi_\nu} + P^m_{e\mu}\frac{d^3\Phi_e}{dE_\nu d\cos\theta_\nu d\phi_\nu}\right] \times \frac{d\sigma_\mu(E_\nu)}{dE_\mu d\cos\theta_\mu} \quad (4.5)$$

where n_d is the number of nucleon targets in the detector, σ_μ is the differential neutrino interaction cross section in terms of the energy and direction of the muon produced, Φ_μ and Φ_e are the ν_μ and ν_e fluxes and $P^m_{\alpha\beta}$ is the oscillation probability of $\nu_\alpha \to \nu_\beta$ in matter and in presence of decay. A sample of 1000 years of unoscillated neutrino events are generated using NUANCE-3.5 neutrino generator [232], in which the Honda 3D atmospheric neutrino fluxes [146] along with neutrino-nucleus cross-sections and a simplified ICAL detector geometry are incorporated. Each event is oscillated by multiplying with the relevant oscillation probability including decay and oscillations in Earth matter assuming PREM density profile [231]. The probabilities are obtained by solving the propagation equation in matter in presence of decay. The events are then smeared according to the resolutions and efficiencies obtained from [10]. These two steps are done on an event by event basis for the entire 1000 year sample. Both "data" and theory are generated via this method, "data" with the central values of the parameters as described in Table 4.2 and theory by varying them in their respective 3σ ranges. Afterwards the oscillated samples of 1000 years of events, both "data" and theory are scaled down to the required number of years, 10 for our current analysis. This is done to reduce the effect of Monte-Carlo fluctuations on sensitivity studies.

In the current analysis, the efficiencies and resolutions of muons in the central region of the detector [10] have been used over the entire detector. These resolutions and efficiencies have been obtained by the INO collaboration via detailed detector simulations using a GEANT4-based [186–188] simulation toolkit for ICAL. The central region of the ICAL detector [10] has the best efficiencies and resolutions for muons, the few-GeV muons in ICAL have a momentum resolution of $\sim 10\%$ and direction resolution of $\sim 1^\circ$ on the average. Their relative charge identification efficiencies is about $\sim 99\%$. However, ICAL has two more regions namely the peripheral [233] and side regions depending on the magnitude and strength of the magnetic field. The peripheral region which has lesser reconstruction efficiencies but only slightly worse resolutions compared to the central region, constitutes 50% of the detector. Hence, in a realistic scenario where the efficiencies and resolutions in different regions are taken appropriately, the results obtained with 10 years of running of 50 kt of ICAL will only be obtained by increasing the run time to 11.3 years, as mentioned in [10].

Since the charged current ν_μ ($\bar{\nu}_\mu$) interactions have μ^- (μ^+) in the final state along with the hadron shower, and since ICAL is capable of measuring the energy of the hadron shower, we include in our analysis the data on those as well. It was reported in [10] from ICAL simulations that hadrons in ICAL have energy resolutions of 85% at 1 GeV and 36% at 15 GeV and the events are smeared accordingly before including them in the final 3D-binned analysis which includes muons binned in observed energy and direction and hadrons binned in energy. There are 15 bins in E_μ^{obs} between $(0.5 - 25)$ GeV, 21 bins in $\cos\theta_\mu^{obs}$ between $(-1, +1)$and 4 bins in $E_{had}^{\prime obs}$ between $(0 - 15)$ GeV, thus giving 1260 bins. More details of the binning scheme and the numerical simulations can be found in Ref. [230].

The true values and the 3σ ranges of the oscillation parameters used to generate the probabilities are given in Table 4.2. Since ICAL is not directly sensitive to $\delta_{\rm CP}$, it is taken as 0° in this analysis and kept fixed. The 1-2 oscillation parameters

Δm^2_{21} and $\sin^2\theta_{12}$ are also kept fixed throughout our analysis. For the remaining parameters two types of analyses are performed, — one with fixed parameter and the other with marginalization. In the former all parameters are kept fixed while in the latter, the parameters other than the one for which the sensitivity study is done are marginalized in their respective 3σ ranges shown in Table 4.2.

Parameter	True value	Marginalization range
θ_{13}	8.5°	$[7.80^\circ, 9.11^\circ]$
$\sin^2\theta_{23}$	0.5	[0.39, 0.64]
Δm^2_{32}	2.366×10^{-3} eV^2	$[2.3, 2.6]\times 10^{-3}$ eV^2 (NH)
$\sin^2\theta_{12}$	0.304	Not marginalized
Δm^2_{21}	7.6×10^{-5} eV^2	Not marginalized
$\delta_{\rm CP}$	0°	Not marginalized

Table 4.2: Oscillation parameters used in this analysis. For fixed parameter studies all parameters are kept at their true values. While applying marginalization, only the parameter for which the sensitivity study is being performed is kept fixed and the others are varied in their respective 3σ ranges.

To statistically analyze the data, we define the following χ^2 function

$$\chi^2 = \min_{\xi_l^\pm, \xi_6} \sum_{i=1}^{N_{E_\mu^{obs}}} \sum_{j=1}^{N_{\cos\theta_\mu^{obs}}} \sum_{k=1}^{N_{E_{had}^{\prime obs}}} 2\left[\left(T^+_{ijk} - D^+_{ijk}\right) - D^+_{ijk}\ln\left(\frac{T^+_{ijk}}{D^+_{ijk}}\right)\right] + 2\left[\left(T^-_{ijk} - D^-_{ijk}\right) - D^-_{ijk}\ln\left(\frac{T^-_{ijk}}{D^-_{ijk}}\right)\right] + \sum_{l^+=1}^{5}\xi^2_{l^+} + \sum_{l^-=1}^{5}\xi^2_{l^-} + \xi^2_6 \ . \quad (4.6)$$

Here i, j, k sum over muon energy, muon angle and hadron energy bins respectively. The number of predicted (theory) events with systematic errors in each bin are given by

$$T^+_{ijk} = T^{0+}_{ijk}\left(1 + \sum_{l^+=1}^{5}\pi^{l^+}_{ijk}\xi_{l^+} + \pi_6\xi_6\right) \ ; T^-_{ijk} = T^{0-}_{ijk}\left(1 + \sum_{l^-=1}^{5}\pi^{l^-}_{ijk}\xi_{l^-} - \pi_6\xi_6\right) \ . \quad (4.7)$$

The number of theory events without systematic errors in a bin is given by $T^{0\pm}_{ijk}$ and the observed events ("data") per bin are given by $D^\pm_{ijk}$. It should be noted that both $D^\pm_{ijk}$ and $T^{0\pm}_{ijk}$ are obtained from the scaled NUANCE neutrino events as mentioned earlier. The following values are taken for the systematic uncertainties [192, 234]:

$\pi_1 = 20\%$ flux normalization error, $\pi_2 = 10\%$ cross section error, $\pi_3 = 5\%$ tilt error, $\pi_4 = 5\%$ zenith angle error, $\pi_5 = 5\%$ overall systematics and $\pi_6 = 2.5\%$ on $\Phi_{\nu_\mu}/\Phi_{\bar{\nu}_\mu}$ ratio. These are included in the analysis via pull method. The "tilt" error is incorporated as follows. The event spectrum with the predicted values of atmospheric neutrino fluxes is calculated and then shifted according to the relation:

$$\Phi_\delta(E) = \Phi_0(E)(\frac{E}{E_0})^\delta \simeq \Phi_0(E)(1 + \delta \ln \frac{E}{E_0}), \tag{4.8}$$

where E_0 is 2 GeV, and δ is the 1σ systematic tilt error (5%). Flux error is included as the difference $\Phi_\delta(E) - \Phi_0(E)$.

A prior of 8% at 1σ is added to $\sin^2 2\theta_{13}$. This is the only prior in this calculation. No prior is imposed at all on the quantities whose sensitivities are to be studied, i.e. on α_3, θ_{23} and $|\Delta m^2_{32}|$. The contribution from prior to the χ^2 is :

$$\chi^2_{\text{prior}} = \left(\frac{\sin^2 2\theta_{13} - \sin^2 2\theta_{13}^{\text{true}}}{\sigma(\sin^2 2\theta_{13})} \right)^2 , \tag{4.9}$$

where, $\sigma(\sin^2 2\theta_{13}) = 0.08 \times \sin^2 2\theta_{13}^{\text{true}}$. Hence, the final χ^2 for ICAL will be :

$$\chi^2_{\text{ICAL}} = \chi^2 + \chi^2_{\text{prior}} , \tag{4.10}$$

where χ^2 is given by Equation 4.6.

4.4 Sensitivity of ICAL to α_3

The results of the sensitivity studies of ICAL to α_3 are presented in this section. We first show how the number of oscillated events change with decay as a function of zenith angle and energy. Then we proceed further to discuss the sensitivity as well as the discovery potential of ICAL to neutrino decay and the bound on α_3 from our analysis.

Effect of decay on the number of oscillated events: In Figure 4.3, we show the zenith angle distribution of the ν_μ and $\bar{\nu}_\mu$ events for different values of the decay constant α_3. The four panels are for four different energy bins. The convention used in these plots is such that $\cos\theta_\mu^{obs} = [0, 1]$ indicates the up-coming neutrinos. It can be seen from the figure that both ν_μ and $\bar{\nu}_\mu$ events deplete with an increase in the value of α_3. We also note that the effect of decay is more prominent in the lower energy bins. With increase in energy, there is no significant effect of decay on the number of events if the decay parameter is less than 10^{-4} eV^2 as can be seen from the lower panels.

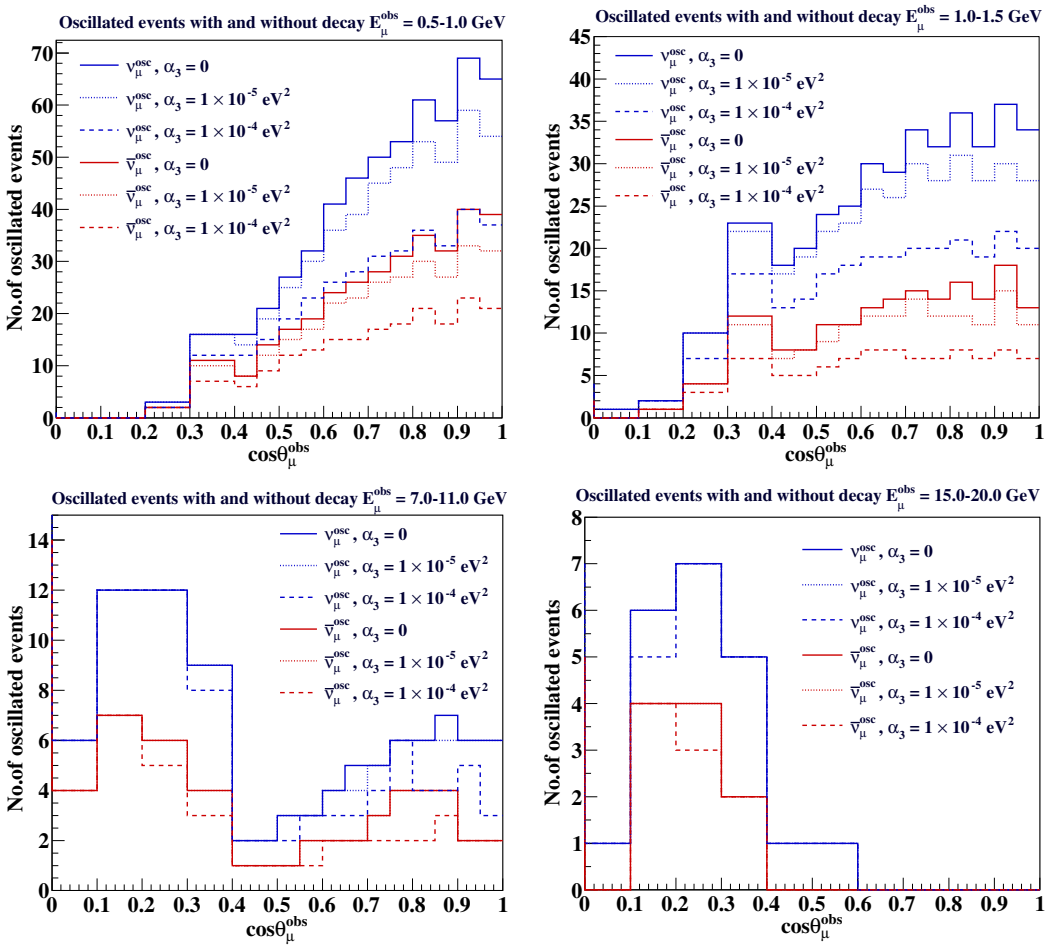

Figure 4.3: Oscillated ν_μ and $\bar{\nu}_\mu$ events for each E_μ^{obs} bin as a function of $\cos\theta_\mu^{obs}$ for $\alpha_3 = 0, 1\times10^{-5}$ and 1×10^{-4} eV^2 . The other parameters are set to their central values as in Table 4.2. It should be noted that the ranges for the y-axes are not the same. Only up-coming events (oscillated) are shown here.

Sensitivity to the decay parameter α_3: In this section, first the study of the sensitivity of ICAL to α_3 is presented with 500 kt-yr exposure of the detector taking normal hierarchy (NH) as the true hierarchy. To that end, we simulate the prospective "data" for no decay and fit it with a theory of oscillation plus decay. The corresponding χ^2 is shown as a function of α_3(test) in the left panel of Figure 4.4.

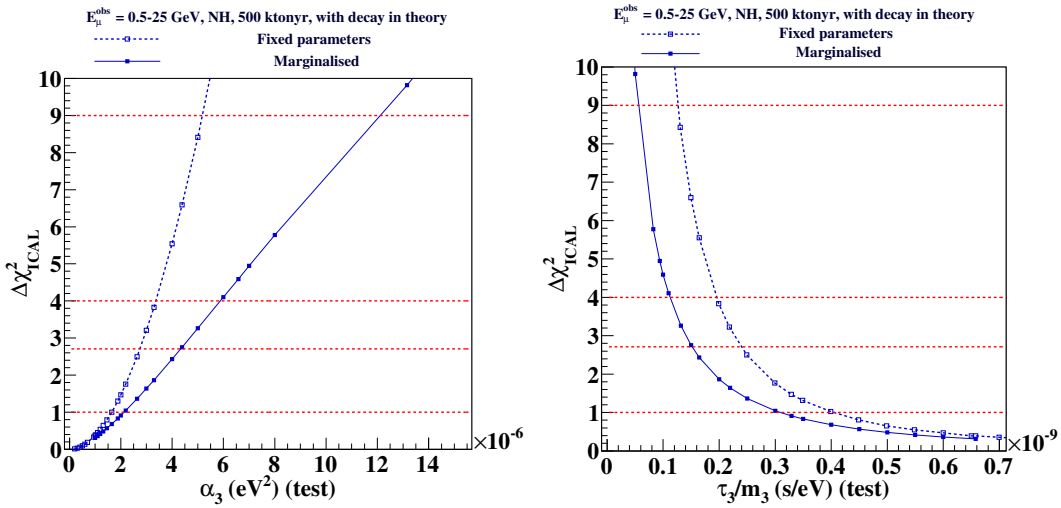

Figure 4.4: Expected sensitivity of ICAL to neutrino decay. The expected χ^2 is shown as a function of α_3 (test) eV^2 (left panel) and τ_3/m_3(test) (s/eV) (right panel) with 500 kt-yr exposure of ICAL.

The blue dashed curve is obtained for a fixed parameter fit while the blue solid one corresponds to the sensitivity when the χ^2 is marginalized over all oscillation parameters as described in Section 4.3. A comparison of the solid and dashed curves gives us an idea of the impact of marginalization over the oscillation parameters on the sensitivity of the experiment to decay. From Figure 4.4 it can be seen that with marginalization of the oscillation parameters, the sensitivity decreases as expected. The right panel shows the sensitivity to decay in terms of τ_3/m_3 in s/eV. The expected sensitivity of ICAL to α_3 are shown in Table 4.3. The corresponding values of τ_3/m_3 in units of s/eV are also given. Note that by sensitivity limit we mean the value of α_3 (τ_3/m_3) up to which ICAL can rule out neutrino decay.

The lower bound on τ_3/m_3 for the invisible decay scenario from MINOS data

Analysis type	$\Delta\chi^2$ (C.L.)	α_3 (eV^2)	τ_3/m_3 (s/eV)
Fixed parameters	1 (1σ)	1.65×10^{-6}	3.99×10^{-10}
	2.71 (90%)	2.73×10^{-6}	2.39×10^{-10}
	4 (2σ)	3.37×10^{-6}	1.96×10^{-10}
	9 (3σ)	5.19×10^{-6}	1.28×10^{-10}
Marginalized	1 (1σ)	2.13×10^{-6}	3.03×10^{-10}
	2.71 (90%)	4.36×10^{-6}	1.51×10^{-10}
	4 (2σ)	5.89×10^{-6}	1.12×10^{-10}
	9 (3σ)	1.21×10^{-5}	5.66×10^{-11}

Table 4.3: Sensitivity to α_3 (eV^2) and τ_3/m_3 (s/eV) with 500 kt-yr exposure of ICAL assuming NH as the true hierarchy.

was shown to be $\tau_3/m_3 > 2.8 \times 10^{-12}$ (s/eV) at 90% C.L. This corresponds to an upper limit $\alpha_3 < 2.35\times10^{-4}$ eV^2. Table 4.3 shows that ICAL is expected to tighten these bounds by two orders of magnitude with just charged current ν_μ and $\bar{\nu}_\mu$ events. At 90% C.L, ICAL with marginalization is expected to give a lower bound of $\tau_3/m_3 > 1.51 \times 10^{-10}$ (s/eV) which corresponds to $\alpha_3 < 4.36 \times 10^{-6}$ eV^2. The bound provided by ICAL is comparable to the limit provided by the global analysis of full atmospheric data from Super-Kamiokande with long baseline experiments K2K and MINOS [32].

The expected sensitivity with fixed parameters as well as marginalization for true IH are shown in Figure 4.5. At 90% C.L, the upper bound on α_3 are $\alpha_3 < 2.78 \times 10^{-6}$ eV^2 with fixed parameters and $\alpha_3 < 5.82 \times 10^{-6}$ eV^2 with marginalization. These are only slightly worse than the sensitivities obtained with true NH. In terms of τ_3/m_3, these limits translate as the lower limits $\tau_3/m_3 > 2.42\times10^{-10}$ s/eV and $\tau_3/m_3 > 1.14 \times 10^{-10}$ s/eV for the fixed parameter and marginalized cases, respectively. The expected sensitivity to α_3 at different C.L. with true IH is summarized in Table 4.4.

The analysis discussed above gives us the sensitivity to α_3 when we fit a "data" with no decay with a theory which has decay. On the other hand, if neutrinos indeed decay into sterile components, and if the decay rate is large enough to be observed in ICAL, we will be able to discover neutrino decay at this experiment.

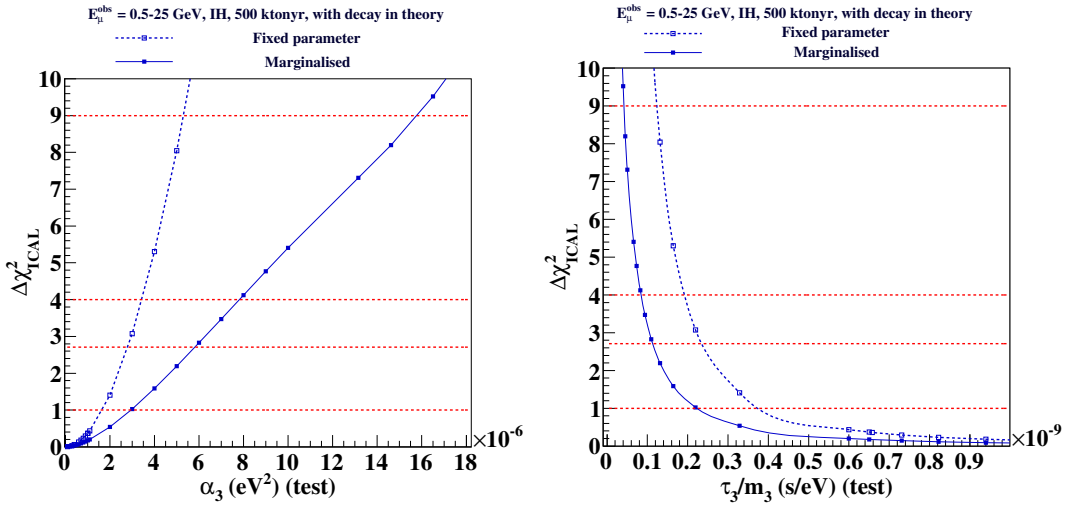

Figure 4.5: Bounds on the allowed values of (left) α_3 eV^2 (right) τ_3/m_3 (s/eV) with 500 kt-yr exposure of ICAL with IH as true hierarchy. The comparison of results for fixed parameter and marginalized cases is shown.

Analysis type	$\Delta\chi^2$ (C.L.)	α_3 (eV^2)	τ_3/m_3 (s/eV)
Fixed parameters	1 (1σ)	1.65×10^{-6}	4.35×10^{-10}
	2.71 (90%)	2.78×10^{-6}	2.42×10^{-10}
	4 (2σ)	3.43×10^{-6}	1.97×10^{-10}
	9 (3σ)	5.31×10^{-6}	1.25×10^{-10}
Marginalized	1 (1σ)	2.97×10^{-6}	2.21×10^{-10}
	2.71 (90%)	5.82×10^{-6}	1.14×10^{-10}
	4 (2σ)	7.82×10^{-6}	8.44×10^{-11}
	9 (3σ)	1.58×10^{-5}	4.21×10^{-11}

Table 4.4: Sensitivity to α_3 (eV^2) and τ_3/m_3 (s/eV) with 500 kt-yr exposure of ICAL assuming IH as the true hierarchy.

Therefore, we next estimate how much the decay rate needs to be in order for ICAL to make this discovery. For this analysis, we simulate the "data" with different values of α_3 and fit it with a theory with no decay. The analysis was done for 500 kt-yr exposure of ICAL for fixed parameters as well as with marginalization of the undisplayed parameters over their respective 3σ ranges. The results are shown in Figure 4.6 by the red-dashed curve for the fixed parameter case and the red-solid line for the marginalized case. However, we find that for the discovery potential, the marginalization has no effect and gives the same result as the fixed parameter case. We find that ICAL will be able to discover neutrino decay at the 90% C.L. if $\alpha_3 > 2.5\times10^{-6}$ eV^2. We also plot the sensitivity curves, blue dashed (solid) lines for

the fixed parameter (marginalized) case, in this figure for a comparison between the 'sensitivity" and "discovery" potential of α_3. We can see that the "sensitivity" and "discovery" limits of ICAL are very similar for fixed parameter analysis. However for the marginalized case the "discovery potential" is significantly higher than the "sensitivity" limit and is same as the fixed parameter case.

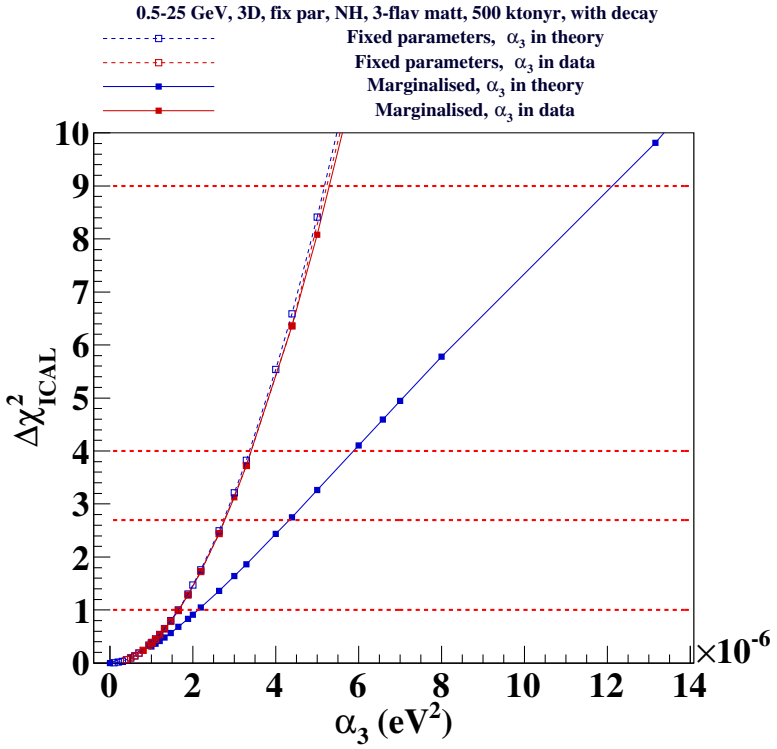

Figure 4.6: "Discovery potential" of α_3 by ICAL with 500 kt-yr exposure assuming NH as the true hierarchy, from fixed parameter and marginalized analyses.

The reason why the expected "sensitivity" limit worsens due to marginalization while the expected "discovery" limit does not can be understood as follows. For the "sensitivity" analysis we generate the data for no decay and θ_{23} maximal and fit it with a theory where $\alpha_3 \neq 0$. Since the effect of decay is to reduce the number of events and suppress the event spectrum for fixed parameter there will be a difference between the data and the theory giving a higher χ^2. For the marginalized case, this can be compensated to some extent by suitably changing the value of θ_{23} from maximal and thereby reducing $\sin^2 2\theta_{23}$, the leading term that controls the amplitude of oscillations in the case of muon neutrino survival probability. This

can be seen in Figure 4.7. In this figure the solid line denotes the "data" generated with $\alpha_3 = 0$ i.e. no decay and $\theta_{23} = 45°$ while the dashed (dotted) lines show the theory events for a non-zero α_3 and $\theta_{23} = 45°(38.65°)$. We can see that the lower value of θ_{23} compensates for the depletion due to decay and can give a lower χ^2. As a result the expected sensitivity drops when the sensitivity χ^2 is marginalized over θ_{23}.

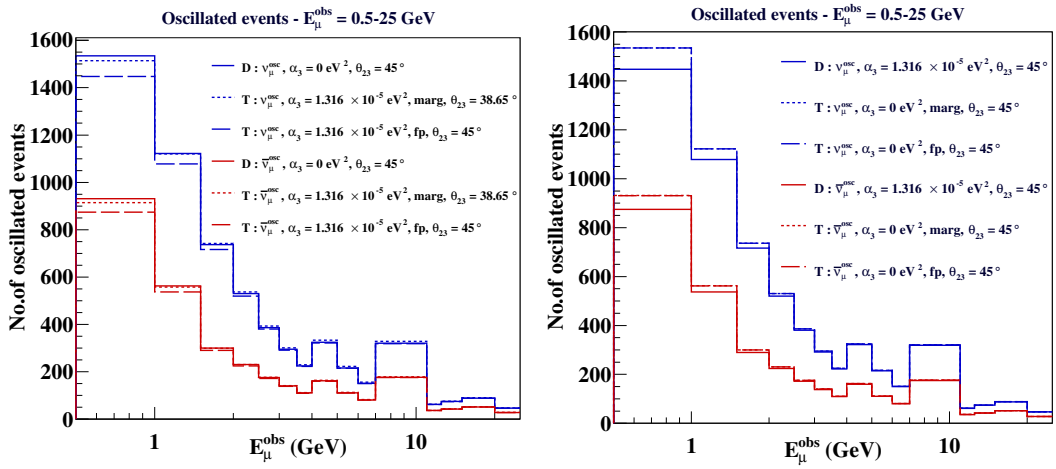

Figure 4.7: Number of oscillated events per E_μ^{obs} bin from 0.5–25 GeV (left) with $\alpha_3 = 0$ eV^2 in "data" and $\alpha_3 = 1.316 \times 10^{-5}$ eV^2 in theory; (right) with $\alpha_3 = 1.316 \times 10^{-5}$ eV^2 in "data" and $\alpha_3 = 0$ eV^2 in theory for the marginalized case. "D" represents data and "T" represents theory events. The blue histograms are for ν_μ and the red ones are for $\bar{\nu}_\mu$ events. The theory events are generated with marginalization of parameters except α_3 in their respective 3σ ranges.

On the other hand, for the expected "discovery" limit case we generate the data for non-zero α_3 and maximal mixing and fit it with a theory with no decay. In this case, the data has events lower than the theory due to decay. This can be seen from the second panel of Figure 4.7 where the blue (red) solid line denotes the data events for muon neutrinos (anti-neutrinos). However, unlike the "sensitivity" case, here one cannot change θ_{23} to reduce the event spectrum any further to compensate for the difference between data and theory since maximal mixing already corresponds to maximal suppression of the muon neutrino survival probability, the leading oscillation channel for atmospheric neutrinos. As a result, the fit continues to keep θ_{23} at its maximal value and marginalization fails to lower the χ^2 any further. This

can also be seen from Figure 4.7 where the dotted line shows the theory events obtained after marginalization and this is higher than the data events and same as the fixed parameter case.

4.5 Precision measurement of $\sin^2\theta_{23}$ and $|\Delta m^2_{32}|$

We next look at the impact of neutrino decay on the precision measurement of the mixing angle θ_{23} and the mass squared difference $|\Delta m^2_{32}|$ at ICAL. A comparison of the precision measurement in the presence and absence of decay is presented. In the no decay case both "data" and theory are generated without the decay parameter and in the case with decay both "data" and theory are generated with non-zero values of α_3. For all results presented in this section, the value $\alpha_3 = 1 \times 10^{-5}$ eV^2 is used to generate the "data". In the fixed parameter analysis this is kept fixed in theory and for the marginalized case, the range over which α_3 is marginalized is taken to be $\alpha_3 = [0, 2.35 \times 10^{-4}]$ eV^2 which corresponds to the 90% CL bound given by the MINOS analysis. The other parameters are kept fixed at their true values as shown in Table 4.2 for the fixed parameter analyses and varied in the 3σ ranges as shown in the same table for the marginalized case. The 1σ precision on a parameter λ is defined as :

$$p(\lambda) = \frac{\lambda_{\text{max-}2\sigma} - \lambda_{\text{min-}2\sigma}}{4\lambda_{true}} \ , \tag{4.11}$$

where $\lambda_{\text{max-}2\sigma}$ and $\lambda_{\text{min-}2\sigma}$ are the maximum and minimum allowed values of λ at 2σ and λ_{true} is the true choice.

4.5.1 Precision on $\sin^2\theta_{23}$ in the presence of decay

The sensitivity to $\sin^2\theta_{23}$ in the presence and absence of ν_3 decay is shown in Figure 4.8. The left panel shows the fixed parameter results whereas the right

panel shows the results for the marginalized case. For the fixed parameter case, in the absence of decay, the 1σ precision on $\sin^2\theta_{23}$ is $\sim$ 8.9%. In presence of decay the 1σ precision is $\sim$8.6% which is similar to the no decay case. However, it is important to note that even though the percentage precision is same, the allowed parameter space is shifted to the right when there is decay, as compared to the no decay case. The minimum and maximum values of $\sin^2\theta_{23}$ at 2σs in the presence and absence of decay are shown in Table 4.5.

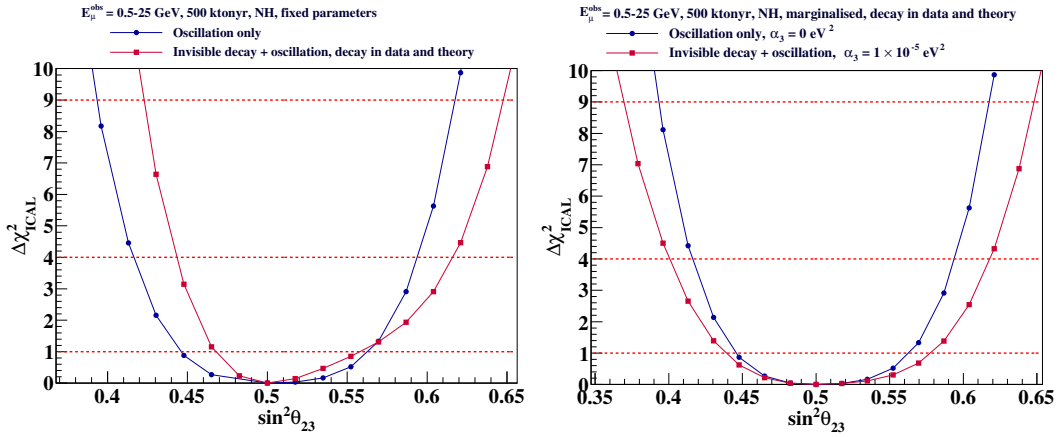

Figure 4.8: Precision on $\sin^2\theta_{23}$ in the presence and absence of invisible decay for (left) fixed parameter case (right) marginalized case. The value of decay parameter α_3 in "data" is taken to be 1×10^{-5} eV^2.

Analysis type	$\sin^2\theta_{23_{min}}(2\sigma)$	$\sin^2\theta_{23_{max}}(2\sigma)$	Precision at 1σ (%)
$\alpha_3 = 0$ eV^2 (fp)	0.416	0.594	8.9
$\alpha_3 = 1\times10^{-5}$ eV^2 (fp)	0.444	0.616	8.6
$\alpha_3 = 0$ eV^2 (marg)	0.416	0.594	8.9
$\alpha_3 = 1\times10^{-5}$ eV^2 (marg)	0.401	0.618	10.85

Table 4.5: Minimum and maximum values of $\sin^2\theta_{23}$ at 2σ, with and without decay for fixed parameter and marginalized cases. The relative 1σ precision obtained is also shown. NH is taken as the true hierarchy.

In order to understand the shift of parameter space, we show in Figure 4.9, the number of oscillated ν_μ and $\bar{\nu}_\mu$ events for three different values of θ_{23} - 39°, 45° and 52° and two different α_3 - 0 and 1×10^{-5} eV^2. Here 39° and 52° are representative values for lower octant and higher octant respectively. We plot the events as a function of energy integrating over the zenith-angle bins. From the figures it can

be seen that both in the absence and presence of decay there are differences between the number of events for various θ_{23} values. For the case of no decay this difference is less as compared to the case where decay is present. Comparing the figures on the left and right panels one also observes that, the difference between the number of events for $\theta_{23} = 39°$ and $45°$ is more in presence of decay and the curve for $\theta_{23} = 45°$ is closer to $52°$. Now, in obtaining the precision plot the data is generated with true $\theta_{23} = 45°$ and in theory the θ_{23} is kept fixed. For θ_{23} in the lower octant the difference of the number of events with that for $45°$ being more in presence of decay, the χ^2 for a θ_{23} in the lower octant will be higher as compared to the no decay case. On the other hand, for θ_{23} in the higher octant the difference in the number of events with $\theta_{23} = 45°$ being less in presence of decay, one gets a lower χ^2 as compared to the no decay case. This explains why the precision curve shifts towards higher θ_{23} values.

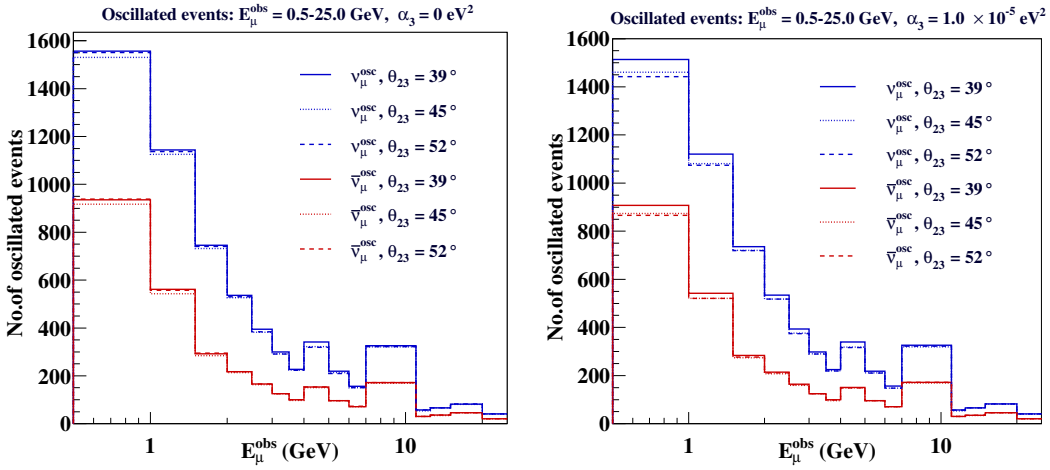

Figure 4.9: Oscillated ν_μ events as a function of E_μ for (left) $\alpha_3 = 0$ eV^2 and (right) $\alpha_3 = 1 \times 10^{-5}$ eV^2 for $\theta_{23} = 39$, 45 and $52°$.

For the marginalized case, in the presence of decay the overall precision becomes worse compared to the no decay case. The 1σ precision when decay is present is $\sim$10.85% whereas for no decay it is $\sim$8.9%. This can be explained as follows. In the marginalized case, for only oscillation we are trying to fit the "data" generated with $\theta_{23} = 45°$, varying the other parameters in theory. In this case the θ_{13} can be

adjusted to give a slightly lower χ^2. In presence of decay we generate the "data" for a particular non-zero α_3 and $\theta_{23} = 45°$. But now in theory we vary α_3 as well as the other parameters. For θ_{23} in the lower octant, the theory events will be higher than the "data" events as can be seen by comparing the events in the second panel of Figure 4.9. However, in this case the α_3 can be increased to give a better fit and a lower χ^2. On the other hand for θ_{23} in the higher octant, the data events are higher than the theory events and α_3 can be decreased in theory to match the data better and give a lower χ^2. This explains the widening of the χ^2 vs θ_{23} curve in presence of decay. Note that this is more for the higher octant because the difference of the events for $\theta_{23} = 45°$ and say $52°$ is less as compared to θ_{23} in the lower octant, say $39°$. This gives a lower χ^2 thus allowing more θ_{23} values in the higher octant.

4.5.2 Precision on $|\Delta m^2_{32}|$ in the presence of decay

The precision on the magnitude of the mass square difference $|\Delta m^2_{32}|$ in the presence and absence of invisible decay of ν_3 is presented in Figure 4.10. NH is taken as the true hierarchy. The relative 1σ precision on $|\Delta m^2_{32}|$ with oscillations only and with decay is $\sim$2.5% for the fixed parameter case. When marginalization is done this becomes $\sim$2.6% for both the cases. Thus it can be seen that the presence of decay does not affect the precision on $|\Delta m^2_{32}|$ much. This is because decay mainly affects the amplitude of the oscillations and not the phase which is determined by $|\Delta m^2_{32}|$. The minimum and maximum values of $\sin^2\theta_{23}$ at 2σs in the presence and absence of decay are shown in Table 4.6.

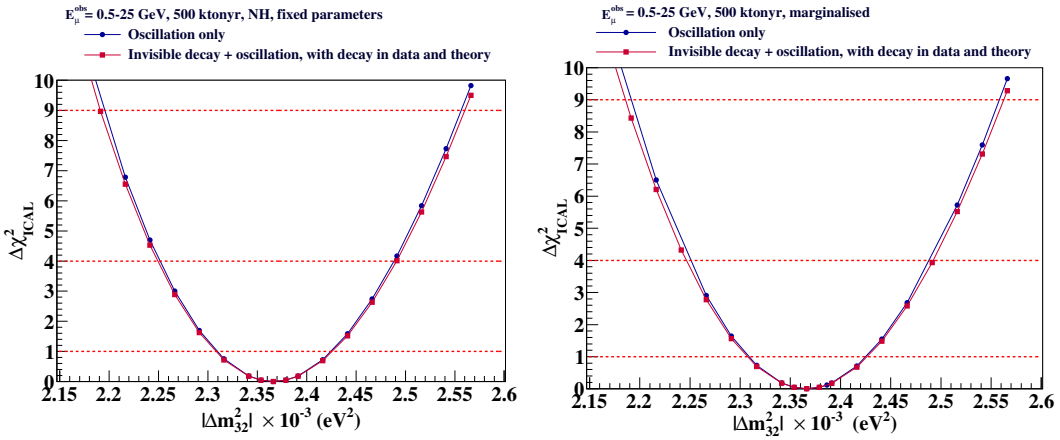

Figure 4.10: Precision on $|\Delta m^2_{32}|$ in the absence and presence of invisible decay (left) fixed parameters (right) with marginalization.

Analysis type	$\|\Delta m^2_{32}\|_{min}(2\sigma)$ $\times 10^{-3}$eV^2	$\|\Delta m^2_{32}\|_{max}(2\sigma)$ $\times 10^{-3}$eV^2	Precision at 1σ (%)
$\alpha_3 = 0$ eV^2 (fp)	2.252	2.489	2.5
$\alpha_3 = 1 \times 10^{-5}$ eV^2 (fp)	2.249	2.492	2.5
$\alpha_3 = 0$ eV^2 (marg)	2.252	2.489	2.6
$\alpha_3 = 1 \times 10^{-5}$ eV^2 (marg)	2.247	2.493	2.6

Table 4.6: Minimum and maximum values of $|\Delta m^2_{32}|$ at 2σ, with and without decay for fixed parameter and marginalized cases. The relative 1σ precision obtained is also shown. NH is taken as the true hierarchy.

4.5.3 Simultaneous precision on $\sin^2\theta_{23}$ and $|\Delta m^2_{32}|$ in the presence of α_3

In this section the expected C.L. contours in the $\sin^2\theta_{23} - |\Delta m^2_{32}|$ plane in the presence of decay are shown. The results are shown for true NH. A value of decay parameter $\alpha_3 = 1 \times 10^{-5}$ eV^2 is taken in "data" and is marginalized in the 3σ range $[0, 2.35 \times 10^{-4}]$ eV^2. The other parameters are also marginalized over their 3σ ranges as before. The expected 90% C.L. contour in the $\sin^2\theta_{23} - |\Delta m^2_{32}|$ plane in the presence and absence of decay is shown in Figure 4.11.

It can be seen that the precision worsens in the presence of decay. The contour widens significantly along the $\sin^2\theta_{23}$ axis, more so in the second octant for the same reason as explained in the context of marginalized case in Figure 4.8. In the absence of decay the precision on $\sin^2\theta_{23}$ at 90% CL is 18.5%. This worsens to

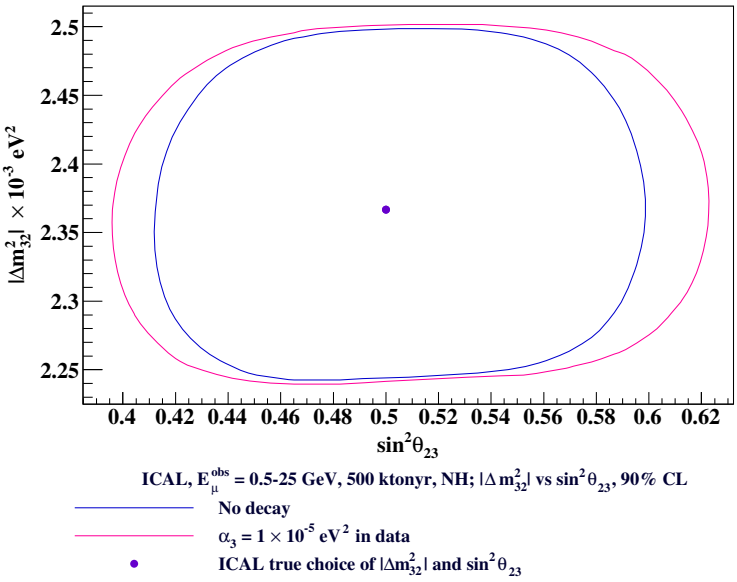

Figure 4.11: Expected 90% C.L. contour in the $\sin^2\theta_{23} - |\Delta m^2{}_{32}|$ plane, with and without decay, for NH. The value of α_3 in "data" is taken as 1×10^{-5} eV^2.

22.3% with a decay parameter $\alpha_3 = 1 \times 10^{-5}$ eV^2. The precision on $|\Delta m^2_{32}|$ worsens only marginally from the no decay value of 5.35% to 5.46% for the same central value of α_3. This is expected since the decay affects the oscillation amplitude which in turn affects the precision on $\sin^2\theta_{23}$.

4.6 Mass hierarchy sensitivity

We have also studied the effect of invisible decay on mass hierarchy determination as compared to the no decay [34]. Results are presented for both NH and IH assuming to be the true hierarchy with fixed and marginalized parameters. For fixed parameter analysis, both true and test parameters are fixed to their central values while for marginalized case, test parameters are varied in their 3σ ranges as given in Table 4.2. While performing the analysis, decay is assumed for both the hierarchies. The true hierarchy NH (IH) is compared with the opposite IH (NH) hierarchy to get the sensitivities in presence of decay. The reduction of the number of events when considering the invisible decay as compared to no decay events affect

the overall mass hierarchy sensitivity. The results are shown for $\alpha_3^{\text{true}} = 10^{-7}$, 6×10^{-6}, 10^{-5}, 2.35×10^{-4} eV^2 and are kept fixed for fixed parameter analysis but varied between $\alpha_3 = [0{:}5.84 \times 10^{-4}]$ eV^2 along with other oscillation parameters in their respective 3σ range as listed in Table 4.2. No decay results (assumes $\alpha_3 = 0$ eV^2 both in data and theory) are also shown for comparison. The variation of mass hierarchy sensitivity in presence of decay for different values of θ_{23} is shown in Figure 4.12 and 4.13 for true hierarchy NH and IH respectively by taking $\sin^2\theta_{23} = 0.41$, 0.5 and 0.63 as representative values.

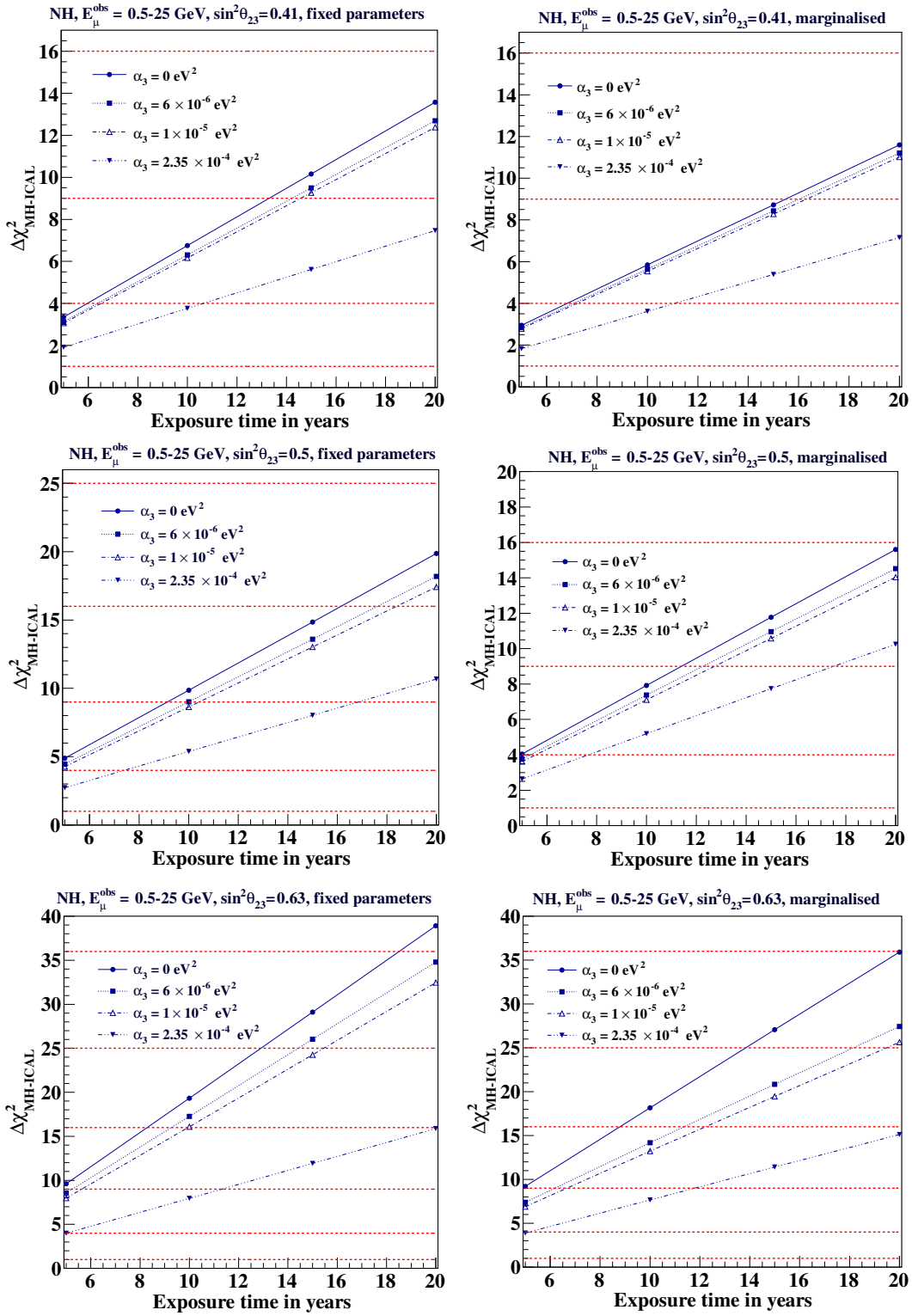

Figure 4.12: Neutrino mass hierarchy sensitivity as a function of exposure time of a 50 kt ICAL with true hierarchy NH for fixed parameters (left) and marginalized parameters (right). Different true values of α_3 used are $0, 6 \times 10^{-6}, 1 \times 10^{-5}$ and 2.35×10^{-4} eV^2. Rows from top to bottom are for true $\sin^2\theta_{23}^{true}$ values of 0.41, 0.5 and 0.63 respectively.

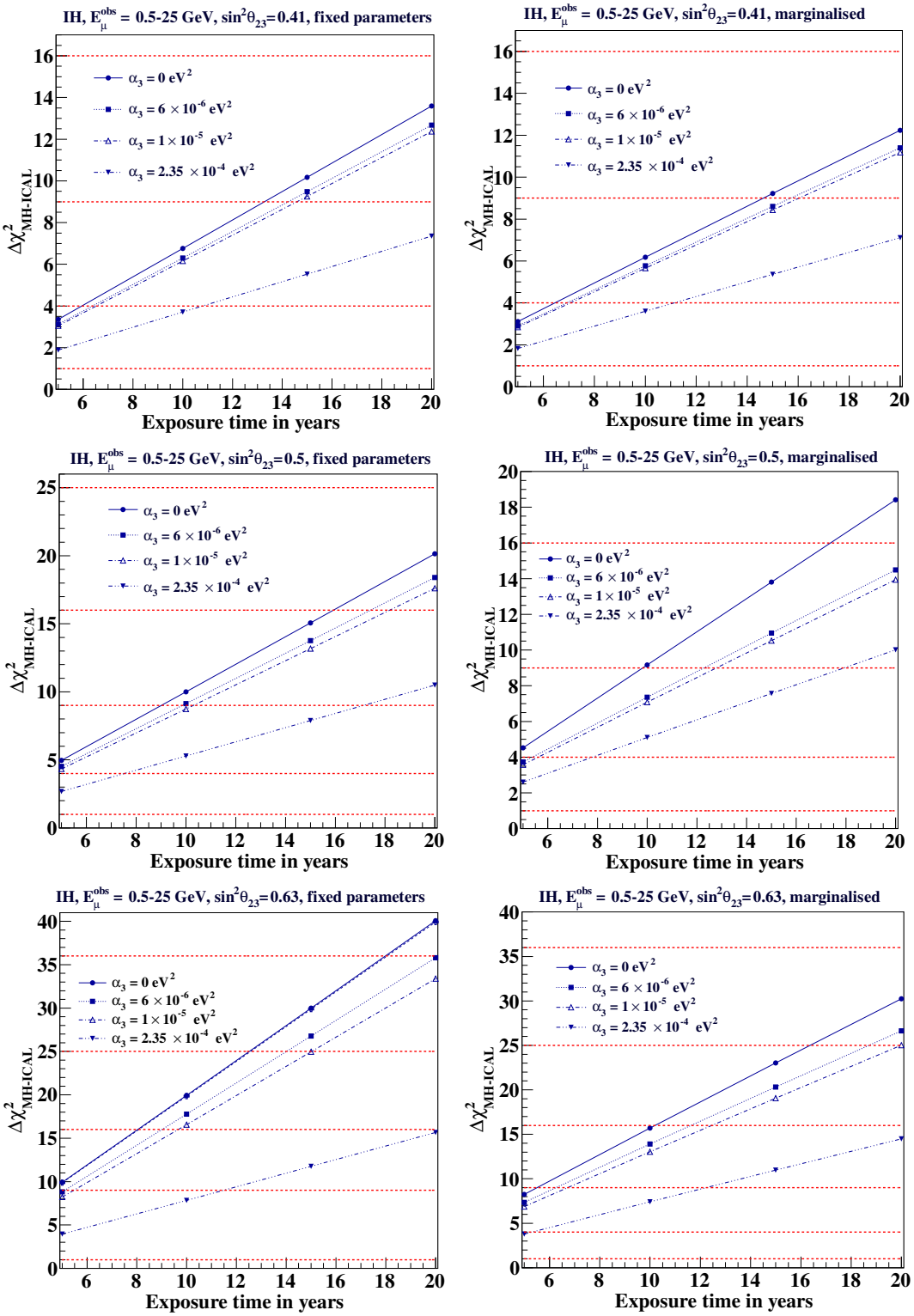

Figure 4.13: Neutrino mass hierarchy sensitivity as a function of exposure time of a 50 kt ICAL with true hierarchy IH for fixed parameters (left) and marginalized parameters (right). Different true values of α_3 used are $0, 6 \times 10^{-6}, 1 \times 10^{-5}$ and 2.35×10^{-4} eV^2. Rows from top to bottom are for true $\sin^2\theta_{23}^{true}$ values of 0.41, 0.5 and 0.63 respectively.

4.7 Summary and Discussions

The expected sensitivity of ICAL to the decay lifetime of the mass eigenstate ν_3, when it decays via the invisible decay mode was presented. The analysis was performed in the three-generation neutrino oscillation framework including decay as well as Earth matter effects. The decay was parameterized in terms of $\alpha_3 = m_3/\tau_3$, where, m_3 is the mass and τ_3 the lifetime at rest of the mass eigenstate ν_3. With 500 kt-yr of exposure, ICAL is expected to constrain the invisible decay rate to $\alpha_3 < 4.36 \times 10^{-6}$ eV^2 at 90% C.L., which is two orders of magnitude tighter than the bound obtained in [33] for MINOS. In [33] both charged current (CC) and neutral current (NC) events were considered where as in our study only atmospheric CC ν_μ and $\bar{\nu}_\mu$ events were used. For invisible neutrino decay, the NC background will be less. Hence the sensitivity to α_3 is expected to improve.

The effect of decay on the 2–3 oscillation parameters was also studied. Since the amplitude of oscillations is affected most by the presence of decay, it was found that decay affected the precision measurement of $\sin^2\theta_{23}$. For 500 kt-yrs of exposure assuming NH as the true hierarchy, the 1σ precision on $\sin^2\theta_{23}$ was found to worsen to 10.85% when $\alpha_3 = 10^{-5}$ eV^2 was assumed. This is worse as compared to the 8.87% obtained with oscillation only hypothesis. In the case of $|\Delta m^2_{32}|$ the 1σ precision without decay is 2.5% whereas the inclusion of invisible decay does not affect it at all.

It is also noteworthy that the sensitivity to smaller α_3 comes mainly from the lower energy bins below 2 GeV. Hence, if we can improve the efficiencies and resolutions of the detector, especially for muons in the lower energy region, we will be able to put a better limit on α_3. Reduction of the energy threshold for the detection of low energy neutrinos in future will also help probing phenomena like decay with increased precision. This is important since the atmospheric neutrino flux peaks at lower energies and by being able to detect and analyze more events

we will further improve our sensitivities to all parameters including α_3.

Chapter 5

Summary and Future Scope

In this thesis we have studied the possibility of determining the unknown neutrino oscillation parameters namely mass hierarchy, octant of θ_{23}, CP phase $\delta_{\rm CP}$ in atmospheric and accelerator based long baseline experiments. In particular, we have considered the synergy between accelerator experiments ESSνSB , T2K , NOνA and the atmospheric neutrino experiment INO. We have also studied the constraints on decaying neutrinos from the observations of atmospheric neutrinos at the ICAL detector of INO. Below we summarize the salient features of each chapter.

First chapter: Introduction In the first introductory chapter of this thesis, we have introduced the background of neutrino and discussed its properties, different sources and the world wide experiments that have been conducted including past, ongoing and future proposed experiments. We have also briefly touched upon the neutrino oscillation phenomenon in vacuum and matter. Values of the oscillation parameters from global oscillation analysis have also been summarized.

Second chapter: ICAL detector and neutrino interaction In second chapter of this thesis we have discussed about the massive 50 kt ICAL detector and its various detector parts and working principles. We have also discussed the components of atmospheric flux and their uncertainties. Interaction cross sections of

neutrinos at various energies with the detector medium has also been discussed in details.

Third chapter: Mass hierarchy and octant sensitivity of INO in conjunction with long baseline experiments ESSνSB is a future proposed long baseline experiment to study the CP violation by focusing on the second oscillation maximum but has poor hierarchy and octant sensitivity due to the parameter degeneracies which is an artifact of two different values of the unknown parameters giving similar number of events. T2K and NOνA are two currently running long baseline experiments to measure the neutrino oscillation parameters. They also suffer from parameter degeneracies. We have shown that the combination of neutrino and anti-neutrino runs and synergies between atmospheric and long baseline experiments help in alleviating some of the degeneracies. This helps to increase the overall sensitivity when neutrino data from INO is combined with the long baseline experiments ESSνSB , NOνA and T2K . We have presented our results for four different combinations NH-LO, NH-HO, IH-LO, IH-HO where true value of θ_{23} have been chosen as 42° and 48° as a representative value for LO and HO respectively. For all the true hierarchy-octant combination, mass hierarchy sensitivity of the combined atmospheric and long baseline experiments mentioned before can be reach $\sim 5\sigma$. Although, INO suffer from the poor octant sensitivity owing to the interplay of survival probability and appearance channel but when added to the other long baseline experiments the overall octant sensitivity can reach $\sim 3\sigma$ irrespective of true hierarchy and $\delta_{\rm CP}$ when considering lower octant and $\sim 2\sigma$ for higher octant.

Fourth chapter: Neutrino decay Other than probing standard neutrino oscillation parameters, INO ICAL detector is also well suited to explore other non standard physics. In Chapter 4 of this thesis, we have explored the capability of ICAL detector to constrain neutrino decay hypothesis along with 3 flavour neu-

trino oscillation. In this work, we have for the first time included 3 flavour matter effect while assuming the highest mass eigenstate to decay invisibly. The invisible decay modes of the neutrino does not produce any active neutrinos and therefore the oscillation amplitude get dampened with a factor $e^{-\frac{\alpha L}{E}}$ where $\alpha = \frac{m_3}{\tau_3}$ is the decay constant with rest frame lifetime τ_3 with mass m_3. This in turn reduces the observed neutrino events in the detector. Because of the wide ranges of $\frac{L}{E}$ in the atmospheric neutrinos and the capability of detecting muons with energy as low as 0.5 GeV, INO experiment is well suited to put stringent bounds on the lifetime of the decaying mass eigenstate. Considering only the charged current interactions with the detector, INO ICAL detector with 500 kt-yr exposure can put bounds $\alpha_3 < 4.36 \times 10^{-6}$ eV^2 with 90% CL which is two orders of improvement than the MINOS combined charge and neutral current analysis. We have also studied in details in Chapter 4 how the presence of decay can affect the precision measurements of the known oscillation parameters. As discussed in details earlier, oscillation amplitude gets modified in the presence of neutrino decay leaving the oscillation frequency intact. Thus the oscillation amplitude which is governed by the oscillation parameter θ_{23} gets correlated with the decay parameter α_3 reducing the 1σ precision of $\sin^2\theta_{23}$ to 10.85% as compared to no decay 8.87% for the assumed decay constant $\alpha_3 = 10^{-5}$ eV^2.

We have also shown that mass hierarchy sensitivity of INO get reduced when we consider neutrino decay as compared to no decay due to the reduction of number of events. For $\alpha = 2.35 \times 10^{-4}$ eV^2, hierarchy sensitivity get reduced by 34% for NH$^{\text{true}}$ and 44% for IH$^{\text{true}}$ from their no decay counterpart.

Future Directions Using synergies between atmospheric and long baseline experiment to put bounds and improving the previous limit on the non standard physics scenarios will be an interesting topic to work on. In our thesis work we have considered only the charged current interactions of neutrinos with the ICAL

detector. With the improvement of the detector resolution and reconstruction efficiencies, neutral current events can also be included to increase the event statistics which in turn will help to increase the sensitivity of the measured quantities related to neutrinos.

Neutral current events remain same with or without oscillation but the same is not true when considering invisible neutrino decay where the total probability of oscillation does not add up to 1. This opens up an interesting topic to carry out further research works. In out thesis work we have only considered the decay of the massive eigen state in active three flavour scenario. The decay of the sterile neutrinos and putting the bounds on the decay lifetime of the sterile neutrinos in (3+1) flavour will also be an interesting topic to work on in the future.

Bibliography

[1] W. pauli, Letter to the participants of workshop at T*ü*bingen, Germany (1930s).

[2] C. L. Cowan, Science 124 **103** (1956).

[3] P. F. de Salas, D. V. Forero, C. A. Ternes, M. Tortola, and J. W. F. Valle, Phys. Lett. **B782**, 633 (2018), arXiv:1708.01186 [hep-ph] .

[4] I. Esteban, M. C. Gonzalez-Garcia, A. Hernandez-Cabezudo, M. Maltoni, and T. Schwetz, JHEP **01**, 106 (2019), arXiv:1811.05487 [hep-ph] .

[5] F. P. An *et al.* (Daya Bay), Phys. Rev. Lett. **108**, 171803 (2012), arXiv:1203.1669 [hep-ex] .

[6] J. A. Formaggio and G. P. Zeller, Rev. Mod. Phys. **84**, 1307 (2012).

[7] D. Casper, Nuclear Physics B - Proceedings Supplements **112**, 161 (2002).

[8] T. K. Gaisser and M. Honda, Annual Review of Nuclear and Particle Science **52**, 153 (2002), https://doi.org/10.1146/annurev.nucl.52.050102.090645 .

[9] D. L. A. Adam M. Dziewonski, Physics of The Earth and Planetary Interiors **25**, 297 (1981).

[10] A. Chatterjee, K. K. Meghna, K. Rawat, T. Thakore, V. Bhatnagar, R. Gandhi, D. Indumathi, N. K. Mondal, and N. Sinha, JINST **9**, P07001 (2014), arXiv:1405.7243 [physics.ins-det] .

[11] K. Abe *et al.* (Hyper-Kamiokande Working Group), (2014), arXiv:1412.4673 [physics.ins-det] .

[12] K. Abe *et al.* (Hyper-Kamiokande proto-), (2016), arXiv:1611.06118 [hep-ex] .

[13] R. Acciarri *et al.* (DUNE), (2015), arXiv:1512.06148 [physics.ins-det] .

[14] E. Baussan, M. Dracos, T. Ekelof, E. F. Martinez, H. Ohman, and N. Vassilopoulos, (2012), arXiv:1212.5048 [hep-ex] .

[15] E. Baussan *et al.* (ESSnuSB), *Proceedings, 2013 Community Summer Study on the Future of U.S. Particle Physics: Snowmass on the Mississippi (CSS2013): Minneapolis, MN, USA, July 29-August 6, 2013*, Nucl. Phys. **B885**, 127 (2014), arXiv:1309.7022 [hep-ex] .

[16] K. Abe *et al.* (T2K), Phys. Rev. Lett. **118**, 151801 (2017), arXiv:1701.00432 [hep-ex] .

[17] P. Adamson *et al.* (NOvA), Phys. Rev. Lett. **118**, 231801 (2017), arXiv:1703.03328 [hep-ex] .

[18] S. K. Agarwalla, S. Prakash, S. K. Raut, and S. U. Sankar, JHEP **12**, 075 (2012), arXiv:1208.3644 [hep-ph] .

[19] R. Patterson (NOνA Collaboration), Neutrino 2012 Conference, Kyoto, Japan, 2012, http://nova-docdb.fnal.gov/cgi-bin/ShowDocument?docid=7546 .

[20] P. Huber, M. Lindner, and W. Winter, Comput. Phys. Commun. **167**, 195 (2005), arXiv:hep-ph/0407333 [hep-ph] .

[21] P. Huber, J. Kopp, M. Lindner, M. Rolinec, and W. Winter, Comput. Phys. Commun. **177**, 432 (2007), arXiv:hep-ph/0701187 [hep-ph] .

[22] K. Chakraborty, S. Goswami, C. Gupta, and T. Thakore, JHEP **05**, 137 (2019), arXiv:1902.02963 [hep-ph] .

[23] M. Ghosh, P. Ghoshal, S. Goswami, and S. K. Raut, Phys. Rev. **D89**, 011301 (2014), arXiv:1306.2500 [hep-ph] .

[24] M. Ghosh, P. Ghoshal, S. Goswami, and S. K. Raut, Nucl. Phys. **B884**, 274 (2014), arXiv:1401.7243 [hep-ph] .

[25] S. K. Agarwalla, S. Prakash, and S. U. Sankar, JHEP **07**, 131 (2013), arXiv:1301.2574 [hep-ph] .

[26] P. A. N. Machado, H. Minakata, H. Nunokawa, and R. Zukanovich Funchal, JHEP **05**, 109 (2014), arXiv:1307.3248 [hep-ph] .

[27] P. Coloma, H. Minakata, and S. J. Parke, Phys. Rev. **D90**, 093003 (2014), arXiv:1406.2551 [hep-ph] .

[28] A. Bandyopadhyay, S. Choubey, and S. Goswami, Phys. Rev. **D63**, 113019 (2001), arXiv:hep-ph/0101273 [hep-ph] .

[29] A. Bandyopadhyay, S. Choubey, and S. Goswami, Phys. Lett. **B555**, 33 (2003), arXiv:hep-ph/0204173 [hep-ph] .

[30] J. M. Berryman, A. de Gouvea, and D. Hernandez, Phys. Rev. **D92**, 073003 (2015), arXiv:1411.0308 [hep-ph] .

[31] R. Picoreti, M. M. Guzzo, P. C. de Holanda, and O. L. G. Peres, Phys. Lett. **B761**, 70 (2016), arXiv:1506.08158 [hep-ph] .

[32] M. C. Gonzalez-Garcia and M. Maltoni, Phys. Lett. **B663**, 405 (2008), arXiv:0802.3699 [hep-ph] .

[33] R. A. Gomes, A. L. G. Gomes, and O. L. G. Peres, Phys. Lett. **B740**, 345 (2015), arXiv:1407.5640 [hep-ph] .

[34] L. S. M. *et al.*, In preparations .

[35] F. Reines and C. L. Cowan, Nature **178**, 446 (1956).

[36] F. Reines and C. L. Cowan, Phys. Today **10N8**, 12 (1957).

[37] A. Gando *et al.* (KamLAND), Phys. Rev. **D88**, 033001 (2013), arXiv:1303.4667 [hep-ex] .

[38] M. Agostini *et al.* (Borexino), Phys. Rev. **D92**, 031101 (2015), arXiv:1506.04610 [hep-ex] .

[39] J. N. Bahcall, Phys. Rev. Lett. **12**, 300 (1964), [,9(1964)].

[40] J. N. Bahcall, A. M. Serenelli, and S. Basu, Astrophys. J. **621**, L85 (2005), arXiv:astro-ph/0412440 [astro-ph] .

[41] R. Davis, D. S. Harmer, and K. C. Hoffman, Phys. Rev. Lett. **20**, 1205 (1968).

[42] H. A. Bethe, Rev. Mod. Phys. **62**, 801 (1990).

[43] K. Hirata *et al.*, Phys. Rev. Lett. **58**, 1490 (1987).

[44] J. F. Beacom and P. Vogel, Phys. Rev. **D60**, 033007 (1999), arXiv:astro-ph/9811350 [astro-ph] .

[45] S. L. Glashow, Nuclear Physics **22**, 579 (1961).

[46] P. W. Higgs, Phys. Lett. **12**, 132 (1964).

[47] P. W. Higgs, Phys. Rev. Lett. **13**, 508 (1964).

[48] P. W. Higgs, Phys. Rev. **145**, 1156 (1966).

[49] F. Englert and R. Brout, Phys. Rev. Lett. **13**, 321 (1964).

[50] G. S. Guralnik, C. R. Hagen, and T. W. B. Kibble, Phys. Rev. Lett. **13**, 585 (1964).

[51] T. W. B. Kibble, Phys. Rev. **155**, 1554 (1967), [165(1967)].

[52] F. J. Hasert *et al.*, Phys. Lett. **B46**, 121 (1973), [5.11(1973)].

[53] F. J. Hasert *et al.* (Gargamelle Neutrino), *30 years of weak neutral currents*, Phys. Lett. **B46**, 138 (1973), [5.15(1973)].

[54] F. J. Hasert *et al.* (Gargamelle Neutrino), Nucl. Phys. **B73**, 1 (1974).

[55] A. Benvenuti, D. C. Cheng, D. Cline, W. T. Ford, R. Imlay, T. Y. Ling, A. K. Mann, F. Messing, R. L. Piccioni, J. Pilcher, D. D. Reeder, C. Rubbia, R. Stefanski, and L. Sulak, Phys. Rev. Lett. **32**, 800 (1974).

[56] S. Chatrchyan *et al.*, Physics Letters B **716**, 30 (2012).

[57] G. Aad *et al.*, Physics Letters B **716**, 1 (2012).

[58] B. Adeva *et al.*, Physics Letters B **231**, 509 (1989).

[59] D. DeCamp *et al.*, Physics Letters B **231**, 519 (1989).

[60] M. Akrawy *et al.*, Physics Letters B **231**, 530 (1989).

[61] P. Aarnio *et al.*, Physics Letters B **231**, 539 (1989).

[62] M. Goldhaber, L. Grodzins, and A. W. Sunyar, Phys. Rev. **109**, 1015 (1958).

[63] B. Pontecorvo, Journal of Experimental and Theoretical Physics **6**, 429 (1958).

[64] B. Pontecorvo, Journal of Experimental and Theoretical Physics **7**, 172 (1958).

[65] B. Pontecorvo, Journal of Experimental and Theoretical Physics **26**, 984 (1968).

[66] Z. Maki, M. Nakagawa, and S. Sakata, Progress of Theoretical Physics **28**, 870 (1962), http://oup.prod.sis.lan/ptp/article-pdf/28/5/870/5258750/28-5-870.pdf .

[67] M. Tanabashi *et al.* (Particle Data Group), Phys. Rev. D **98**, 030001 (2018).

[68] L. Wolfenstein, Phys. Rev. D **17**, 2369 (1978).

[69] S. P. Mikheyev and A. Yu. Smirnov, Sov. J. Nucl. Phys. **42**, 913 (1985), [,305(1986)].

[70] I. Esteban, M. C. Gonzalez-Garcia, M. Maltoni, I. Martinez-Soler, and T. Schwetz, Journal of High Energy Physics **2017**, 87 (2017).

[71] Http://www.nu-fit.org/.

[72] T. Araki *et al.* (KamLAND Collaboration), Phys. Rev. Lett. **94**, 081801 (2005).

[73] F. P. An *et al.* (Daya Bay), Phys. Rev. Lett. **108**, 171803 (2012), arXiv:1203.1669 [hep-ex] .

[74] M. C. Gonzalez-Garcia, M. Maltoni, and T. Schwetz, JHEP **11**, 052 (2014), arXiv:1409.5439 [hep-ph] .

[75] *Fundamental Physics at the Intensity Frontier* (2012) arXiv:1205.2671 [hep-ex] .

[76] F. Capozzi, E. Di Valentino, E. Lisi, A. Marrone, A. Melchiorri, and A. Palazzo, Phys. Rev. **D95**, 096014 (2017), arXiv:1703.04471 [hep-ph] .

[77] I. Esteban, M. C. Gonzalez-Garcia, M. Maltoni, I. Martinez-Soler, and T. Schwetz, JHEP **01**, 087 (2017), arXiv:1611.01514 [hep-ph] .

[78] A. de Gouvea *et al.* (Intensity Frontier Neutrino Working Group), in *Proceedings, 2013 Community Summer Study on the Future of U.S. Particle Physics: Snowmass on the Mississippi (CSS2013): Minneapolis, MN, USA, July 29-August 6, 2013* (2013) arXiv:1310.4340 [hep-ex] .

[79] B. T. Cleveland, T. Daily, R. Davis, Jr., J. R. Distel, K. Lande, C. K. Lee, P. S. Wildenhain, and J. Ullman, Astrophys. J. **496**, 505 (1998).

[80] R. Davis, Phys. Rev. Lett. **12**, 303 (1964).

[81] R. Davis, Progress in Particle and Nuclear Physics **32**, 13 (1994).

[82] J. N. Bahcall, Astrophysical Journal **137**, 344 (1963).

[83] J. N. Bahcall, Phys. Rev. **C56**, 3391 (1997), arXiv:hep-ph/9710491 [hep-ph] .

[84] V. N. Gavrin, Physics-Uspekhi **54**, 941 (2011).

[85] V. N. Gavrin, Physics of Atomic Nuclei **76**, 1238 (2013).

[86] M. Shiozawa *et al.* (Super-Kamiokande), Phys. Rev. Lett. **81**, 3319 (1998), arXiv:hep-ex/9806014 [hep-ex] .

[87] Y. Fukuda *et al.* (Super-Kamiokande), Phys. Lett. **B433**, 9 (1998), arXiv:hep-ex/9803006 [hep-ex] .

[88] T. Kajita, E. Kearns, and M. Shiozawa, Nuclear Physics B **908**, 14 (2016), neutrino Oscillations: Celebrating the Nobel Prize in Physics 2015.

[89] J. N. Bahcall, P. I. Krastev, and A. Yu. Smirnov, Phys. Rev. **D60**, 093001 (1999), arXiv:hep-ph/9905220 [hep-ph] .

[90] M. C. Gonzalez-Garcia, C. Pena-Garay, and A. Yu. Smirnov, Phys. Rev. **D63**, 113004 (2001), arXiv:hep-ph/0012313 [hep-ph] .

[91] Q. R. Ahmad *et al.* (SNO Collaboration), Phys. Rev. Lett. **89**, 011301 (2002).

[92] Q. R. Ahmad *et al.* (SNO Collaboration), Phys. Rev. Lett. **87**, 071301 (2001).

[93] S. N. Ahmed *et al.* (SNO Collaboration), Phys. Rev. Lett. **92**, 181301 (2004).

[94] M. Maris and S. Petcov, Physics Letters B **534**, 17 (2002).

[95] G. Alimonti *et al.* (Borexino), Nucl. Instrum. Meth. **A600**, 568 (2009), arXiv:0806.2400 [physics.ins-det] .

[96] M. Agostini *et al.* (Borexino), (2017), arXiv:1709.00756 [hep-ex] .

[97] P. Adamson *et al.* (MINOS), Phys. Rev. Lett. **106**, 181801 (2011), arXiv:1103.0340 [hep-ex] .

[98] K. Abe *et al.*, Nuclear Instruments and Methods in Physics Research Section A: Accelerators, Spectrometers, Detectors and Associated Equipment **659**, 106 (2011).

[99] T. Nakaya, *T2K presents hint of CP violation by neutrinos, http://t2k-experiment.org/2017/08/t2k-2017-cpv/*.

[100] M. Hartz (KEK seminar and press release Aug 2017), *T2K Neutrino Oscillation Results with Data up to 2017 Summer*.

[101] D. S. Ayres *et al.* (NOvA), (2004), arXiv:hep-ex/0503053 [hep-ex] .

[102] M. A. Acero *et al.* (NOvA), Phys. Rev. **D98**, 032012 (2018), arXiv:1806.00096 [hep-ex] .

[103] K. Eguchi *et al.* (KamLAND), Phys. Rev. Lett. **90**, 021802 (2003), arXiv:hep-ex/0212021 [hep-ex] .

[104] M. Decowski, Nuclear Physics B **908**, 52 (2016), neutrino Oscillations: Celebrating the Nobel Prize in Physics 2015.

[105] T. Araki *et al.* (KamLAND), Phys. Rev. Lett. **94**, 081801 (2005), arXiv:hep-ex/0406035 [hep-ex] .

[106] T. Araki *et al.*, Nature **436**, 499 (2005).

[107] Y. Abe *et al.* (Double Chooz), JHEP **10**, 086 (2014), [Erratum: JHEP02,074(2015)], arXiv:1406.7763 [hep-ex] .

[108] F. Suekane and T. Junqueira de Castro Bezerra (Double Chooz), Nucl. Phys. **B908**, 74 (2016), arXiv:1601.08041 [hep-ex] .

[109] J. K. Ahn *et al.* (RENO), Phys. Rev. Lett. **108**, 191802 (2012), arXiv:1204.0626 [hep-ex] .

[110] S.-H. Seo (RENO), *Proceedings of the 15th International Workshop on Neutrino Telescopes (Neutel 2013): Venice, March 11-15, 2013*, PoS **Neutel2013**, 018 (2014), arXiv:1312.4111 [physics.ins-det] .

[111] M. G. Aartsen *et al.* (IceCube), Astrophys. J. **857**, 117 (2018), arXiv:1712.06277 [astro-ph.HE] .

[112] B. P. Abbott *et al.*, Astrophys. J. **848**, L12 (2017), arXiv:1710.05833 [astro-ph.HE] .

[113] M. G. Aartsen *et al.*, Science **361**, eaat1378 (2018), arXiv:1807.08816 [astro-ph.HE] .

[114] M. G. Aartsen *et al.* (IceCube), Science **361**, 147 (2018), arXiv:1807.08794 [astro-ph.HE] .

[115] S. Adrian-Martinez *et al.* (KM3Net), J. Phys. **G43**, 084001 (2016), arXiv:1601.07459 [astro-ph.IM] .

[116] S. Adrian-Martinez *et al.* (Antares), Astrophys. J. **743**, L14 (2011), arXiv:1108.0292 [astro-ph.HE] .

[117] M. G. Aartsen *et al.* (IceCube), Phys. Rev. **D98**, 062003 (2018), arXiv:1807.01820 [astro-ph.HE] .

[118] M. G. Aartsen *et al.* (IceCube), Phys. Rev. **D91**, 072004 (2015), arXiv:1410.7227 [hep-ex] .

[119] R. Abbasi *et al.* (IceCube), Phys. Rev. **D81**, 057101 (2010), arXiv:0910.4480 [astro-ph.CO] .

[120] R. Abbasi *et al.* (IceCube), Phys. Rev. Lett. **102**, 201302 (2009), arXiv:0902.2460 [astro-ph.CO] .

[121] M. G. Aartsen *et al.* (IceCube Collaboration), Phys. Rev. Lett. **117**, 071801 (2016).

[122] N. Agafonova *et al.*, Physics Letters B **691**, 138 (2010).

[123] K. Abe *et al.* (Hyper-Kamiokande), (2018), arXiv:1805.04163 [physics.ins-det] .

[124] M. G. Aartsen *et al.* (IceCube), J. Phys. **G44**, 054006 (2017), arXiv:1607.02671 [hep-ex] .

[125] S. Ahmed *et al.* (ICAL), Pramana **88**, 79 (2017), arXiv:1505.07380 [physics.ins-det] .

[126] Y.-F. Li, J. Cao, Y. Wang, and L. Zhan, Phys. Rev. **D88**, 013008 (2013), arXiv:1303.6733 [hep-ex] .

[127] R. Acciarri *et al.* (DUNE), (2016), arXiv:1601.05471 [physics.ins-det] .

[128] S. Mertens, *Proceedings, Prospects in Neutrino Physics (NuPhys2015): London, UK, December 16-18, 2015*, J. Phys. Conf. Ser. **718**, 022013 (2016), arXiv:1605.01579 [nucl-ex] .

[129] M. Czakon, M. Zralek, and J. Gluza, *Recent developments in theory of fundamental interactions. Proceedings, 23rd School of Theoretical Physics, Ustron, Poland, September 15-22, 1999*, Acta Phys. Polon. **B30**, 3121 (1999), arXiv:hep-ph/9910357 [hep-ph] .

[130] R. Romero, Mod. Phys. Lett. **A31**, 1650113 (2016), [Erratum: Mod. Phys. Lett.A32,no.17,1792001(2017)], arXiv:1605.02975 [physics.gen-ph] .

[131] A. Roberts, Review of Scientific Instruments **32**, 482 (1961), https://doi.org/10.1063/1.1717420 .

[132] Yu. N. Pestov, Nucl. Instrum. Meth. **196**, 45 (1982).

[133] R. Santonico and R. Cardarelli, Nucl. Instrum. Meth. **187**, 377 (1981).

[134] R. Santonico, R. Cardarelli, A. Di Biagio, and A. Lucci, Nucl. Instrum. Meth. **A263**, 20 (1988).

[135] V. Datar *et al.*, *Resistive plate chambers and related detectors. Proceedings, 9th International Workshop, RPC2007, Mumbai, India, February 13-16, 2008*, Nucl. Instrum. Meth. **A602**, 744 (2009).

[136] V. Datar *et al.*, Nuclear Instruments and Methods in Physics Research Section A: Accelerators, Spectrometers, Detectors and Associated Equipment **602**, 744 (2009), proceedings of the 9th International Workshop on Resistive Plate Chambers and Related Detectors.

[137] *Electromagnetic field simulation software, Infolytica Corp.*, http://www.infolytica.com/en/products/magnet/.

[138] T. Kajita, Adv. High Energy Phys. **2012**, 504715 (2012).

[139] D. Casper *et al.*, Phys. Rev. Lett. **66**, 2561 (1991).

[140] W. Allison *et al.*, Physics Letters B **391**, 491 (1997).

[141] K. Hirata *et al.*, Physics Letters B **280**, 146 (1992).

[142] M. Honda, T. Kajita, K. Kasahara, and S. Midorikawa, Phys. Rev. **D83**, 123001 (2011), arXiv:1102.2688 [astro-ph.HE] .

[143] M. Honda, T. Kajita, K. Kasahara, S. Midorikawa, and T. Sanuki, Phys. Rev. **D75**, 043006 (2007), arXiv:astro-ph/0611418 [astro-ph] .

[144] G. D. Barr, T. K. Gaisser, P. Lipari, S. Robbins, and T. Stanev, Phys. Rev. **D70**, 023006 (2004), arXiv:astro-ph/0403630 [astro-ph] .

[145] G. Battistoni, A. Ferrari, T. Montaruli, and P. R. Sala, Astropart. Phys. **19**, 269 (2003), [Erratum: Astropart. Phys.19,291(2003)], arXiv:hep-ph/0207035 [hep-ph] .

[146] T. K. Gaisser and M. Honda, Ann. Rev. Nucl. Part. Sci. **52**, 153 (2002), arXiv:hep-ph/0203272 [hep-ph] .

[147] T. Kajita (Super-Kamiokande, Kamiokande), *Proceedings, International Conference on Neutrino physics and astrophysics (Neutrino'98): Takayama, Japan, June 4-9, 1998*, Nucl. Phys. Proc. Suppl. **77**, 123 (1999), [123(1998)], arXiv:hep-ex/9810001 [hep-ex] .

[148] J. A. Formaggio and G. P. Zeller, Rev. Mod. Phys. **84**, 1307 (2012), arXiv:1305.7513 [hep-ex] .

[149] M. M. Devi, A. Ghosh, D. Kaur, L. S. Mohan, S. Choubey, A. Dighe, D. Indumathi, S. Kumar, M. V. N. Murthy, and M. Naimuddin, JINST **8**, P11003 (2013), arXiv:1304.5115 [physics.ins-det] .

[150] L. S. Mohan, A. Ghosh, M. M. Devi, D. Kaur, S. Choubey, A. Dighe, D. Indumathi, M. V. N. Murthy, and M. Naimuddin, JINST **9**, T09003 (2014), arXiv:1401.2779 [physics.ins-det] .

[151] R. E. Kalman, Transactions of the ASME - Journal of Basic Engineering , 35 (1960).

[152] V. Barger, D. Marfatia, and K. Whisnant, Phys. Rev. **D65**, 073023 (2002), arXiv:hep-ph/0112119 [hep-ph] .

[153] J. Burguet-Castell, M. B. Gavela, J. J. Gomez-Cadenas, P. Hernandez, and O. Mena, Nucl. Phys. **B646**, 301 (2002), arXiv:hep-ph/0207080 [hep-ph] .

[154] H. Minakata and H. Nunokawa, JHEP **10**, 001 (2001), arXiv:hep-ph/0108085 [hep-ph] .

[155] M. Ghosh, P. Ghoshal, S. Goswami, N. Nath, and S. K. Raut, Phys. Rev. **D93**, 013013 (2016), arXiv:1504.06283 [hep-ph] .

[156] N. Nath, S. Goswami, and K. N. Deepthi, *Proceedings, XXII DAE High Energy Physics Symposium: Delhi, India, December 12 -16, 2016*, Springer Proc. Phys. **203**, 611 (2018), arXiv:1703.00245 [hep-ph] .

[157] S. K. Agarwalla, S. Prakash, and S. Uma Sankar, JHEP **03**, 087 (2014), arXiv:1304.3251 [hep-ph] .

[158] M. Ghosh, S. Goswami, and S. K. Raut, Eur. Phys. J. **C76**, 114 (2016), arXiv:1412.1744 [hep-ph] .

[159] K. Bora, D. Dutta, and P. Ghoshal, Mod. Phys. Lett. **A30**, 1550066 (2015), arXiv:1405.7482 [hep-ph] .

[160] V. Barger, A. Bhattacharya, A. Chatterjee, R. Gandhi, D. Marfatia, and M. Masud, Phys. Rev. **D89**, 011302 (2014), arXiv:1307.2519 [hep-ph] .

[161] K. N. Deepthi, C. Soumya, and R. Mohanta, New J. Phys. **17**, 023035 (2015), arXiv:1409.2343 [hep-ph] .

[162] N. Nath, M. Ghosh, and S. Goswami, Nucl. Phys. **B913**, 381 (2016), arXiv:1511.07496 [hep-ph] .

[163] C. Soumya, K. N. Deepthi, and R. Mohanta, Adv. High Energy Phys. **2016**, 9139402 (2016), arXiv:1408.6071 [hep-ph] .

[164] P. Coloma, P. Huber, J. Kopp, and W. Winter, Phys. Rev. **D87**, 033004 (2013), arXiv:1209.5973 [hep-ph] .

[165] P. Ballett, S. F. King, S. Pascoli, N. W. Prouse, and T. Wang, Phys. Rev. **D96**, 033003 (2017), arXiv:1612.07275 [hep-ph] .

[166] S. K. Agarwalla, M. Ghosh, and S. K. Raut, JHEP **05**, 115 (2017), arXiv:1704.06116 [hep-ph] .

[167] M. Ghosh, Phys. Rev. **D93**, 073003 (2016), arXiv:1512.02226 [hep-ph] .

[168] M. Ghosh and O. Yasuda, Phys. Rev. **D96**, 013001 (2017), arXiv:1702.06482 [hep-ph] .

[169] S. K. Raut, Phys. Rev. **D96**, 075029 (2017), arXiv:1703.07136 [hep-ph] .

[170] C. R. Das, J. Pulido, J. Maalampi, and S. Vihonen, Phys. Rev. **D97**, 035023 (2018), arXiv:1708.05182 [hep-ph] .

[171] K. Chakraborty, K. N. Deepthi, and S. Goswami, Nucl. Phys. **B937**, 303 (2018), arXiv:1711.11107 [hep-ph] .

[172] E. Wildner *et al.*, Adv. High Energy Phys. **2016**, 8640493 (2016), arXiv:1510.00493 [physics.ins-det] .

[173] S. K. Agarwalla, S. Choubey, and S. Prakash, JHEP **12**, 020 (2014), arXiv:1406.2219 [hep-ph] .

[174] A. Chatterjee, P. Ghoshal, S. Goswami, and S. K. Raut, JHEP **06**, 010 (2013), arXiv:1302.1370 [hep-ph] .

[175] E. K. Akhmedov, R. Johansson, M. Lindner, T. Ohlsson, and T. Schwetz, JHEP **04**, 078 (2004), arXiv:hep-ph/0402175 [hep-ph] .

[176] S. Prakash, U. Rahaman, and S. U. Sankar, JHEP **07**, 070 (2014), arXiv:1306.4125 [hep-ph] .

[177] L. Wolfenstein, Phys. Rev. **D17**, 2369 (1978), [,294(1977)].

[178] S. P. Mikheyev and A. Yu. Smirnov, Sov. J. Nucl. Phys. **42**, 913 (1985), [,305(1986)].

[179] S. P. Mikheev and A. Yu. Smirnov, Nuovo Cim. **C9**, 17 (1986).

[180] B. Brahmachari, S. Choubey, and P. Roy, Nucl. Phys. **B671**, 483 (2003), arXiv:hep-ph/0303078 [hep-ph] .

[181] A. Chatterjee, P. Ghoshal, S. Goswami, and S. K. Raut, JHEP **1306**, 010 (2013), arXiv:1302.1370 [hep-ph] .

[182] E. Baussan *et al.* (ESSnuSB Collaboration), Nucl.Phys. **B885**, 127 (2014), arXiv:1309.7022 [hep-ex] .

[183] I. K. and, Journal of Physics: Conference Series **136**, 022018 (2008).

[184] D. Casper, *Proceedings, 1st International Workshop on Neutrino-nucleus interactions in the few GeV region (NuInt 01): Tsukuba, Japan, December 13-16, 2001*, Nucl. Phys. Proc. Suppl. **112**, 161 (2002), [,161(2002)], arXiv:hep-ph/0208030 [hep-ph] .

[185] A. M. Dziewonski and D. L. Anderson, Phys. Earth Planet. Interiors **25**, 297 (1981).

[186] S. Agostinelli *et al.*, Nuclear Instruments and Methods in Physics Research Section A: Accelerators, Spectrometers, Detectors and Associated Equipment **506**, 250 (2003).

[187] J. Allison *et al.*, Nuclear Instruments and Methods in Physics Research Section A: Accelerators, Spectrometers, Detectors and Associated Equipment **835**, 186 (2016).

[188] J. Allison *et al.*, IEEE Transactions on Nuclear Science **53**, 270 (2006).

[189] T. Thakore, A. Ghosh, S. Choubey, and A. Dighe, JHEP **05**, 058 (2013), arXiv:1303.2534 [hep-ph] .

[190] M. M. Devi, T. Thakore, S. K. Agarwalla, and A. Dighe, JHEP **10**, 189 (2014), arXiv:1406.3689 [hep-ph] .

[191] R. Gandhi, P. Ghoshal, S. Goswami, P. Mehta, S. U. Sankar, and S. Shalgar, Phys. Rev. **D76**, 073012 (2007), arXiv:0707.1723 [hep-ph] .

[192] M. C. Gonzalez-Garcia and M. Maltoni, Phys. Rev. **D70**, 033010 (2004), arXiv:hep-ph/0404085 [hep-ph] .

[193] S. Prakash, S. K. Raut, and S. U. Sankar, Phys. Rev. **D86**, 033012 (2012), arXiv:1201.6485 [hep-ph] .

[194] S. Choubey, S. Goswami, C. Gupta, S. M. Lakshmi, and T. Thakore, Phys. Rev. **D97**, 033005 (2018), arXiv:1709.10376 [hep-ph] .

[195] A. Mirizzi, D. Montanino, and P. D. Serpico, Phys. Rev. **D76**, 053007 (2007), arXiv:0705.4667 [hep-ph] .

[196] Y. Chikashige, R. N. Mohapatra, and R. D. Peccei, Phys. Lett. **98B**, 265 (1981).

[197] G. B. Gelmini and M. Roncadelli, Phys. Lett. **99B**, 411 (1981).

[198] G. Gelmini and J. Valle, Physics Letters B **142**, 181 (1984).

[199] A. Acker, S. Pakvasa, and J. T. Pantaleone, Phys. Rev. **D45**, 1 (1992).

[200] A. Acker, A. Joshipura, and S. Pakvasa, Physics Letters B **285**, 371 (1992).

[201] J. N. Bahcall, N. Cabibbo, and A. Yahil, Phys. Rev. Lett. **28**, 316 (1972), [,285(1972)].

[202] A. Acker and S. Pakvasa, Phys. Lett. **B320**, 320 (1994), arXiv:hep-ph/9310207 [hep-ph] .

[203] Z. G. Berezhiani, G. Fiorentini, M. Moretti, and A. Rossi, Z. Phys. **C54**, 581 (1992).

[204] Z. G. Berezhiani, M. Moretti, and A. Rossi, Z. Phys. **C58**, 423 (1993).

[205] S. Choubey, S. Goswami, and D. Majumdar, Phys. Lett. **B484**, 73 (2000), arXiv:hep-ph/0004193 [hep-ph] .

[206] A. S. Joshipura, E. Masso, and S. Mohanty, Phys. Rev. **D66**, 113008 (2002), arXiv:hep-ph/0203181 [hep-ph] .

[207] J. A. Frieman, H. E. Haber, and K. Freese, Phys. Lett. **B200**, 115 (1988).

[208] J. M. LoSecco, (1998), arXiv:hep-ph/9809499 [hep-ph] .

[209] P. Lipari and M. Lusignoli, Phys. Rev. **D60**, 013003 (1999), arXiv:hep-ph/9901350 [hep-ph] .

[210] V. D. Barger, W.-Y. Keung, and S. Pakvasa, Phys. Rev. **D25**, 907 (1982).

[211] V. D. Barger, J. G. Learned, S. Pakvasa, and T. J. Weiler, Phys. Rev. Lett. **82**, 2640 (1999), arXiv:astro-ph/9810121 [astro-ph] .

[212] G. L. Fogli, E. Lisi, A. Marrone, and G. Scioscia, Phys. Rev. **D59**, 117303 (1999), arXiv:hep-ph/9902267 [hep-ph] .

[213] S. Choubey and S. Goswami, Astropart. Phys. **14**, 67 (2000), arXiv:hep-ph/9904257 [hep-ph] .

[214] V. D. Barger, J. G. Learned, P. Lipari, M. Lusignoli, S. Pakvasa, and T. J. Weiler, Phys. Lett. **B462**, 109 (1999), arXiv:hep-ph/9907421 [hep-ph] .

[215] Y. Ashie *et al.* (Super-Kamiokande), Phys. Rev. Lett. **93**, 101801 (2004), arXiv:hep-ex/0404034 [hep-ex] .

[216] A. M. Gago, R. A. Gomes, A. L. G. Gomes, J. Jones-Perez, and O. L. G. Peres, JHEP **11**, 022 (2017), arXiv:1705.03074 [hep-ph] .

[217] J. F. Beacom, N. F. Bell, D. Hooper, S. Pakvasa, and T. J. Weiler, Phys. Rev. Lett. **90**, 181301 (2003), arXiv:hep-ph/0211305 [hep-ph] .

[218] M. Maltoni and W. Winter, JHEP **07**, 064 (2008), arXiv:0803.2050 [hep-ph] .

[219] G. Pagliaroli, A. Palladino, F. L. Villante, and F. Vissani, Phys. Rev. **D92**, 113008 (2015), arXiv:1506.02624 [hep-ph] .

[220] M. Bustamante, J. F. Beacom, and K. Murase, Phys. Rev. **D95**, 063013 (2017), arXiv:1610.02096 [astro-ph.HE] .

[221] P. Coloma and O. L. G. Peres, (2017), arXiv:1705.03599 [hep-ph] .

[222] S. Choubey, S. Goswami, and D. Pramanik, JHEP **02**, 055 (2018), arXiv:1705.05820 [hep-ph] .

[223] A. Chatterjee, R. Gandhi, and J. Singh, JHEP **06**, 045 (2014), arXiv:1402.6265 [hep-ph] .

[224] N. Dash, V. M. Datar, and G. Majumder, Pramana **86**, 927 (2016), arXiv:1410.5182 [hep-ex] .

[225] S. Choubey, A. Ghosh, T. Ohlsson, and D. Tiwari, JHEP **12**, 126 (2015), arXiv:1507.02211 [hep-ph] .

[226] S. P. Behera, A. Ghosh, S. Choubey, V. M. Datar, D. K. Mishra, and A. K. Mohanty, Eur. Phys. J. **C77**, 307 (2017), arXiv:1605.08607 [hep-ph] .

[227] B. Pontecorvo, Sov. Phys. JETP **26**, 984 (1968), [Zh. Eksp. Teor. Fiz.53,1717(1967)].

[228] B. Pontecorvo, Sov. Phys. JETP **6**, 429 (1957), [Zh. Eksp. Teor. Fiz.33,549(1957)].

[229] Z. Maki, M. Nakagawa, and S. Sakata, Prog. Theor. Phys. **28**, 870 (1962), [,34(1962)].

[230] L. S. Mohan and D. Indumathi, Eur. Phys. J. **C77**, 54 (2017), arXiv:1605.04185 [hep-ph] .

[231] A. M. Dziewonski and D. L. Anderson, Physics of the Earth and Planetary Interiors **25**, 297 (1981).

[232] D. Casper, Nuclear Physics B - Proceedings Supplements **112**, 161 (2002).

[233] R. Kanishka, K. K. Meghna, V. Bhatnagar, D. Indumathi, and N. Sinha, JINST **10**, P03011 (2015), arXiv:1503.03369 [physics.ins-det] .

[234] J. Kameda, *Detailed studies of neutrino oscillations with atmospheric neutrinos of wide energy range from 100 MeV to 1000 GeV in Super-Kamiokande*, Ph.D. thesis, Tokyo U. (2002).